A MULTIWAVELENGTH OBSERVATIONAL INVESTIGATION OF HERBIG-HARO OBJECTS AND THEIR EXCITING STARS

Thesis by

Karl Roald Stapelfeldt

In Partial Fullfillment of the Requirements
for the Degree of
Doctor of Philosophy

California Institute of Technology
Pasadena, California
1991
Submitted May 28, 1991

Acknowledgements

A Ph.D. thesis would be an impossible task without the help and support of many individuals. I had the good fortune to work with three research groups during the course of this thesis, truly spreading my indebtedness around. At Caltech I thank Nick Scoville for his patience and willingness to take on a student with his own crazy thesis idea. Nick steered me toward the OVRO millimeter interferometer, which although not in my original thesis plan ended up producing some of the most interesting results.

I am very grateful to John Trauger, who accepted the idea of pointing a Fabry-Perot at an HH object and gave his time and effort to make the observing runs possible. I can't soon forget the time when John traveled with me to Palomar, led a long instrument set-up, and stayed up through a night of observations – all while knowing he had to return to JPL for a meeting the next morning. I thank him for his financial support, which I enjoyed earning through work on his Io plasma torus project.

I also express my appreciation to Chas Beichman, who gave me the opportunity to use a state of the art infrared camera and trusted me to spend 14 K buying filters for it. My research benefited directly from all the time that Chas, Jeff Hester, and Nick Gautier spent coaxing down the noise in the Prime Focus camera electronics.

I was very fortunate to be awarded a NASA Graduate Fellowship for the 1988-1990 academic years. This financial support helped make my independent research possible. I thank the JPL educational affairs office for giving me the opportunity, and hope that over my career I can pay back NASA's investment in me.

Working on space astronomy projects has been a real highlight of my graduate school years. Charles Elachi, in addition to teaching the most interesting courses I

took at Caltech, arranged my first summer job at JPL. I didn't find any features in Rich Terrile's groundbased images of Uranus (which was fortunate, since neither did Voyager 2 a few months later), but the introduction to CCD image processing was very valuable. I thank Jim Westphal for giving me the task of building a WF/PC diffraction testbed, and Paul Swanson for involving me in the LDR design team.

In addition to John I have many other people to thank at JPL. The WFPC II project staff accepted me as one of their own and gave me full access to their resources. Dwight Moody is an ideal of what a computer system manager should be, always willing to help, sometimes even letting me get away with occupying 1.2 gigabytes of disk space. Dwight and Brian Gordon gave invaluable assistance to my Fabry-Perot data reduction task, and were cheerful lunchtime companions. Dave Crisp was always up to something interesting and willing to tell me about it, and generously included me in his Venus near-infrared imaging project.

Most of this thesis was written while I worked at IPAC, and everyone there has been very supportive. I am indebted to Jeff Hester, who wrote the software that I used to reduce my IR camera data, straightened out my understanding of interstellar shocks several times, made fundamental scientific contributions to the discussion of my infrared imaging results, and virtually shared his office with me for a whole year. It is hard to thank him enough. Sue Tereby, Dave Van Buren, and Debbie Levine provided valuable help and discussion, and Mary Ellen Barba made everything that I needed happen.

Many people on the Caltech campus improved my graduate student years. I thank Gerry Neugebauer for the job working the 200″ pointing corrections, Lilo Hauck and Sandy Lester for getting my paychecks out of limbo, and Ernie Lorenz for his friendly and capable instruction in the S. Mudd machine shop. Fellow graduate students, Alain Porter, Kent Budge, and Chris Wilson were friendly officemates. My Robinson inmate experience was also enhanced by the likes of Blaise Canzian, Steve Myers, Chuck Steidel, Alain Picard, Rich Rand, Josh Roth, and Irwin Horowitz. During my first years at Caltech I spent much time over in the

Planetary Science department, where Bill Anderson, Walter Kiefer, Mark Hofstadter and others welcomed me as an "honorary" Planetary Science student. I was fortunate to import friends from my Princeton undergraduate years to Caltech: Dave Goldstein, Mark Looper, Frank Mills, and Deborah Padgett. Debbie has been and always will be my most important friend, colleague, and companion. I would be lost without her support and encouragement.

To the memory of my parents

A Multiwavelength Observational Investigation of Herbig-Haro Objects and Their Exciting Stars

Ph.D. Thesis of

Karl Roald Stapelfeldt

Abstract:

Herbig-Haro objects are small optical emission line nebulae, shock-heated by collimated winds from young stars. In this thesis, near-infrared imaging and high resolution optical imaging spectroscopy have been used to investigate Herbig-Haro object shock structure. Four objects have been studied: HH 7-11, HH 12, HH 34, and HH 1. By a detailed comparison of emission line images and spatially complete kinematic maps, we find that although no single flow model can be applied to all regions, some regions do fit the existing models quite well. HH 7 is well-described as the working surface of a stellar jet, with both a bowshock and a jet terminus shock identified within it. The density of this jet is shown to be comparable to the density of the medium it is impacting. Based on the absence of 2 μm H_2 line emission in the shocked wind material, H_2 does not appear to be a major constituent of the outflowing winds. Where H_2 emission is found, the associated [S II] emission tends to have lower radial velocities. The 1.64 μm [Fe II] emission line has been imaged for the first time in HH objects. The [Fe II] images indicate extinction is not significant in determining the optical appearance of the HH objects studied, and thus the HH 34 bipolar outflow is indeed a one-sided jet system. The kinematics and H_2 morphology of HH 12 argue for SVS 12 as this object's exciting star, a

conclusion which strongly suggests that the observed proper motions in this object represent pattern motion rather than a material velocity.

The second part of this work is a study of the circumstellar material of two HH object exciting stars using millimeter-wave interferometry. High resolution ^{13}CO images suggest that the HH 34 and HH 111 exciting stars both possess circumstellar disks elongated perpendicular to the highly collimated optical jets emerging from these two sources. The masses of these disks are two to four times greater than the disk masses found for T Tauri stars, although the sizes are comparable. The stellar source masses are most likely less than 2 $M_{\odot}$. The total weight of evidence argues that HH exciting stars represent an earlier stage of stellar evolution than T Tauri stars, and that large disk masses are being accreted onto the central star, dispersed by the outflow winds, and/or formed into planets during the earliest phases of the life of a star.

Table of Contents

Chapter I.

Thesis Introduction

The formation of stars is a central question of modern astronomy, not just for its astrophysical import but also because it is a key to understanding the origins of planets and life. In addressing this question an astronomer faces much the same challenge as a geologist who wishes to understand how a mountain range is formed. The astronomer and the geologist both have some ideas about how their favorite features came to be, but precious little firsthand observation of the process in action. The difficulty is that both the mountains and the stars form over millions of years, too long a time for a single scientist (or all of human civilization, for that matter) to follow the process. By studying only an ordinary mountain a geologist might never fathom how it came to be; but by studying an extraordinary mountain called a volcano, he discovers that its features and behavior are a rosetta stone to the answers he seeks. As the geologist must study the right mountains, so must the astronomer study the right stars to address their origins. Of the countless observable stars, which ones reveal the most about the star formation process?

Out of all the classes of stars that astronomers have catalogued, there is now general agreement that T Tauri stars represent the youngest optically visible stars. These late-type irregular variable stars were first recognized by Joy (1945) from their strong Hα emission. Their proximity to dark galactic clouds and OB associations was the first indication of their youth. In the HR diagram T Tauri stars are found above the main sequence, in the region of fully convective Hayashi tracks which are predicted for stars evolving toward the main sequence. These theoretical

evolutionary tracks imply stellar ages of just a few million years.

A key to undertanding even earlier stages of star formation was found in the 1970's, when the large molecular mass fraction of the interstellar medium was first recognized. This discovery led to the realization that galactic molecular clouds provide the source material for star formation. Gravitational collapse of a clump of molecular gas leads to a dense gaseous core; eventually core temperatures become high enough to fuse deuterium and then hydrogen, stabilizing the core against further collapse and yielding a star. During these early phases of accretion, models predict that the protostar will be optically invisible, hidden by the absorbing dust in the surrounding cloud material. The very young predecessors to T Tauri stars are therefore expected to be visible only at infrared wavelengths.

As millimeter-wave observational astronomy matured, it was discovered that there were regions in molecular clouds where carbon monoxide (CO) emission line wings were extended to radial velocities tens of kilometers per second from the cloud's central velocity. Such velocities imply highly supersonic motions in the cold molecular cloud material. Often the blue and red-shifted CO line wings are spatially offset from each other on the sky; it is believed that these "bipolar" outflows arise when two oppositely directed, outflowing stellar wind streams sweep up nearby molecular cloud gas. In a few instances, a visible T Tauri star may be found between the outflow lobes, identifying it as the outflow source. In other cases without an associated visible star, an infrared source is found near the outflow center. The clear implication is that very young stars undergo a stage of energetic mass loss during their pre-main sequence evolution. The outflows thus may be responsible for sweeping away the nascent cloud material, leading to the emergence of an optical T Tauri star.

The discovery of bipolar molecular outflows helped to clarify the nature of a class of small, faint emission nebulae — the so-called Herbig-Haro objects. Named after their joint discoverers, HH objects are found in association with dark clouds. For many years the HH objects themselves were thought to be the sites of forming stars. However, when it was discovered that many bipolar outflows were accompanied by HH objects along the flow axis, it was soon realized that the HH objects are optical manifestations of the same outflows. In 1981, Herbig and Jones discovered large, oppositely directed proper motions for HH 1 and 2, implying space motions of 300 km s^{-1} in a bipolar optical outflow. The optical spectra of HH objects suggest shock excitation (Schwartz 1981). From these discoveries, a new understanding of HH objects emerged: they are shock-heated regions where a supersonic wind from a young stellar object (YSO) impacts the nearby interstellar gas.

A remarkable aspect of HH objects is the evidence they give of outflow collimation. In 1983, Mundt and Fried discovered highly collimated optical emission line jets extending between outflow source stars and several Herbig-Haro objects. The observed optical jet opening angles are much smaller than those implied by the CO observations. Subsequent work using narrowband imaging has documented many additional examples of these jets and their association with HH objects and CO outflows (Mundt *et al.* 1984; Reipurth *et al.* 1986; Hartigan *et al.* 1986; Strom *et al.* 1986; Solf 1987; Raga and Mateo 1987; Mundt, Brugel and Buhrke 1987). Spectroscopically these jets resemble Herbig-Haro objects of a unique low excitation character, indicating that the jet emission is excited by low velocity or oblique shocks. Figure 1 shows the HH 34 system, described by Mundt as "the finest example of a jet/ HH object complex."

Figure 1 suggests that the HH objects represent a stellar analog to the much

larger jets responsible for the double-lobed radio emission associated with entire galaxies. HH objects are therefore of very general astrophysical interest, as they are a laboratory to test our understanding of the formation and propagation of gaseous jets. Aside from their physical scale, the stellar outflows differ from their extragalactic counterparts in two important respects: (1) They are non-relativistic, although they are highly supersonic; and (2) the shocked regions exhibit an emission line spectrum, not a synchrotron continuum. As a result, the hydrodynamics of the YSO outflow can be studied in detail from measurements of emission line ratios and radial velocities. Such information cannot be directly obtained for the galactic scale outflows.

The outflow sources which produce HH objects are known as "HH object exciting stars." These stars are usually optically obscured and must be found by infrared observations (Cohen and Schwartz 1983). In actuality HH exciting stars are just a subclass of the bipolar outflow sources. The bolometric luminosities of these stars (as measured by IRAS) are consistent with models of protostars of mass $< 2\ M_{\odot}$ (Cohen & Schwartz 1987). It has been suggested for some time that bipolar outflows may be collimated and/or energized by circumstellar disks at the outflow sources (Pudritz 1986). Accretion of disk material is suggested as the energy source for the outflow process and the outflow provides a convenient means for transporting angular momentum away from the accreting protostar. From this theoretical perspective it follows that stars with energetic, collimated HH object flows are likely to also have massive circumstellar disks.

The formation of our planetary system took place 4.6 billion years ago in the gas and dust surrounding the early sun. The coplanar orbits of our planetary system indicate that this protoplanetary matter was distributed in a circumstellar disk.

The study of disks around very young stars is therefore one of the most important contributions observational astronomy can make to the study of the origin of the solar system. It is of great interest to compare the masses and sizes of observed circumstellar disks to those inferred for our own solar nebula; to determine the frequency of disk formation around solar-type stars; and to determine the timescales for disk evolution. Recent millimeter observations (Sargent 1989; Beckwith *et al.* 1990) have addressed the first two issues very successfully, finding that disks appear to be commonly associated with T Tauri stars. To address the question of disk evolution, stars of different ages must be studied. HH object exciting stars, as likely T Tauri predecessors, may offer an opportunity to study circumstellar disks in their earliest evolutionary phases.

Despite the substantial observational and theoretical progress which has occurred over the past decade there remain many outstanding questions as to how these star-jet-shock systems operate. Does a circumstellar disk energize and collimate the jets? Can we understand in detail the hydrodynamics of the HH object outflows? A host of mechanisms have been proposed to account for the shocks seen in HH objects, including: the termination of a jet in the ambient medium; the interaction of the flow with small dense obstacles; "interstellar bullets" ejected by the star; boundary layer effects at the walls of an outflow cavity; and internal oblique shocks within a jet. How do these outflows affect the evolution of the protostar and the dynamics of the surrounding molecular clouds? What are the implications of this phase of energetic outflow for the early solar nebula and the formation of planetary systems?

Herbig-Haro objects and their exciting stars are currently the subjects of active worldwide astronomical research; most of what is currently known about these ob-

jects has been learned in the last ten years. This thesis represents a multiwavelength observational effort to gather detailed information about 5 different HH object systems, in the expectation that many of the issues discussed above can be directly addressed.

Three new instruments have been employed in this research, making possible observations that would have been difficult or impractical just eight years ago. A near-infrared array camera has been used to study the morphology and distribution of 2.12 μm H_2 emission; by comparing optical and H_2 images, inferences can be made about shock type and geometry. A Fabry-Perot CCD imaging spectrometer has been used to map the full HH object velocity fields at seeing-limited resolution, allowing tests of shock models and the identification of outflow sources. Last but not least, the Owens Valley Millimeter Interferometer has been used to resolve the circumstellar molecular gas associated with two HH object exciting stars.

A brief shock primer

To orient the reader for the discussion of HH object shocks in the first two chapters it is worth reviewing the terminology and complexity involved in the study of interstellar shocks. A formal review can be found in McKee and Hollenbach (1980). When two gases collide supersonically, each is shocked near the material interface (the "contact discontinuity"). Each shock will heat and compress the medium passing through it at the expense of the flow kinetic energy. The strength of an astrophysical shock is characterized by the *shock velocity*, which is the component of the flow velocity perpendicular to the shock surface. Normal shocks have a shock velocity equal to the full speed of the flowing gas, whereas oblique shocks have much smaller shock velocities.

The shock velocity is the single most important parameter in determining the emission spectrum of shock-heated gas. To understand this emitted spectrum, one first must realize that little or no emission arises from the shock front itself. Instead, most of the observable emission is produced by the shock-heated gas as it cools. Very large shock velocities ($\geq$ 300 km s^{-1}, with the exact value density-dependent) are strong enough to completely ionize the shocked gas, so much so that its cooling time becomes very large. This is the case of a non-radiative (or "adiabatic") shock. A radiative (or "isothermal") shock occurs at lower shock velocities; rapid cooling occurs in the post-shock recombination zone. A whole range of temperatures is found in this zone, from a peak temperature determined by the shock velocity down to ambient values. Accordingly, the emission spectrum from this cooling zone is a composite of many different temperature regions. Large shock velocities will produce emission in high temperature (or 'high excitation') species such as [O III]; lower-velocity shocks (20 - 100 km s^{-1}) lack this high-excitation emission and will radiate primarily in lines such as Hα and [S II]. Shock models have been created that allow the shock velocity to be related to the observed emission line ratios in a quantitative way.

The physical characteristics of the pre-shock medium have an important effect on the spectrum of a radiative shock, and must be taken into account in shock modelling. A very important variable is the physical state of the gas. For a given shock velocity, a high excitation spectrum will be emitted if the pre-shock medium is fully ionized; a lower excitation spectrum will be emitted if the pre-shock medium is atomic, and lower still if it is molecular. This behavior occurs because shock energy is expended in ionization and/or dissociation of the gas, leading to lower peak postshock temperatures. Another variable is the magnetic field in the preshock medium. In a magnetohydrodynamic (MHD) shock, work must be done to compress

the field as well as the gas. A medium with a significant magnetic field will therefore produce a lower excitation shock emission spectrum than a medium with no field, for a given shock velocity. Still another complication is the presence of shock precursors. Although no pressure disturbances can propagate ahead of the advancing shock front, radiative and magnetic precursors can affect the pre-shock ambient medium. Strong shocks will produce Lyman α emission in their postshock cooling zones, which can then propagate ahead of the shock to pre-ionize the ambient medium. This pre-ionization provides free electrons which can then propagate ahead of the hydrodyanamic shock at the local Alfven speed. By collisions with neutrals, ions, and/or molecules, these electrons can accelerate the pre-shock medium before the direct hydrodynamic effects of the shock are felt. If a magnetic precursor is strong enough to accelerate the medium to equivalent postshock flow velocities without any discontinuous jumps in the flow properties, the shock is termed a "C-shock" (or continuous shock). It is clear that the variable properties of the pre-shock medium prevent a simple one-to-one correspondence between the shock velocity and the emitted spectrum.

References

Beckwith, S., Sargent, A. I., Chini, R. S., and Gusten, R. 1990 A.J. 99 924

Cohen, M. C. and Schwartz, R. D. 1987 Ap.J. 316 311

Cohen, M. C. and Schwartz, R. D. 1983 Ap.J. 265 877

Hartigan, P., Lada, C. J., Stocke, J., and Tapia, S. 1986 A.J. 92 1155

Herbig, G. H., and Jones, B. F. 1981 A.J. 86 1232

Joy, A. H. 1945 Ap.J. 102 168

McKee, C. F. and Hollenbach, D. J. 1980 Ann.Rev.Astron.Astrophys. 18 219

Mundt, R., Brugel, E. W., and Buhrke, T. 1987 Ap.J. 319 275

Mundt, R., Buhrke, T., Fried, J. W., Neckel, T., Sarcander, M., and Stocke, J. 1984 Astr.Astrophys. 140 17

Pudritz, R. E. 1988 in *Galactic and Extragalactic Star Formation*, R.E. Pudritz and M. Fich eds. Kluwer Academic Publishers pp. 135-158

Reipurth, B., Bally, J., Graham, J. A., Lane, A. P., and Zealey, W. J. 1986 Astron.Astrophys. 164 51

Sargent, A. I. in *The Formation and Evolution of Planetary Systems*, STSci Symposium Series 3 (1989), H. A. Weaver and L. Danly eds., Cambridge University Press, pp. 111-129.

Schwartz, R. D. 1981 Ap.J. 243 197

Solf, J. 1987 Ast.Astro. 184 322

Strom, K. M., Strom, S. E., Wolff, S. C., Morgan, J., and Wenz, M. 1986 Ap.J.Suppl. 62 39

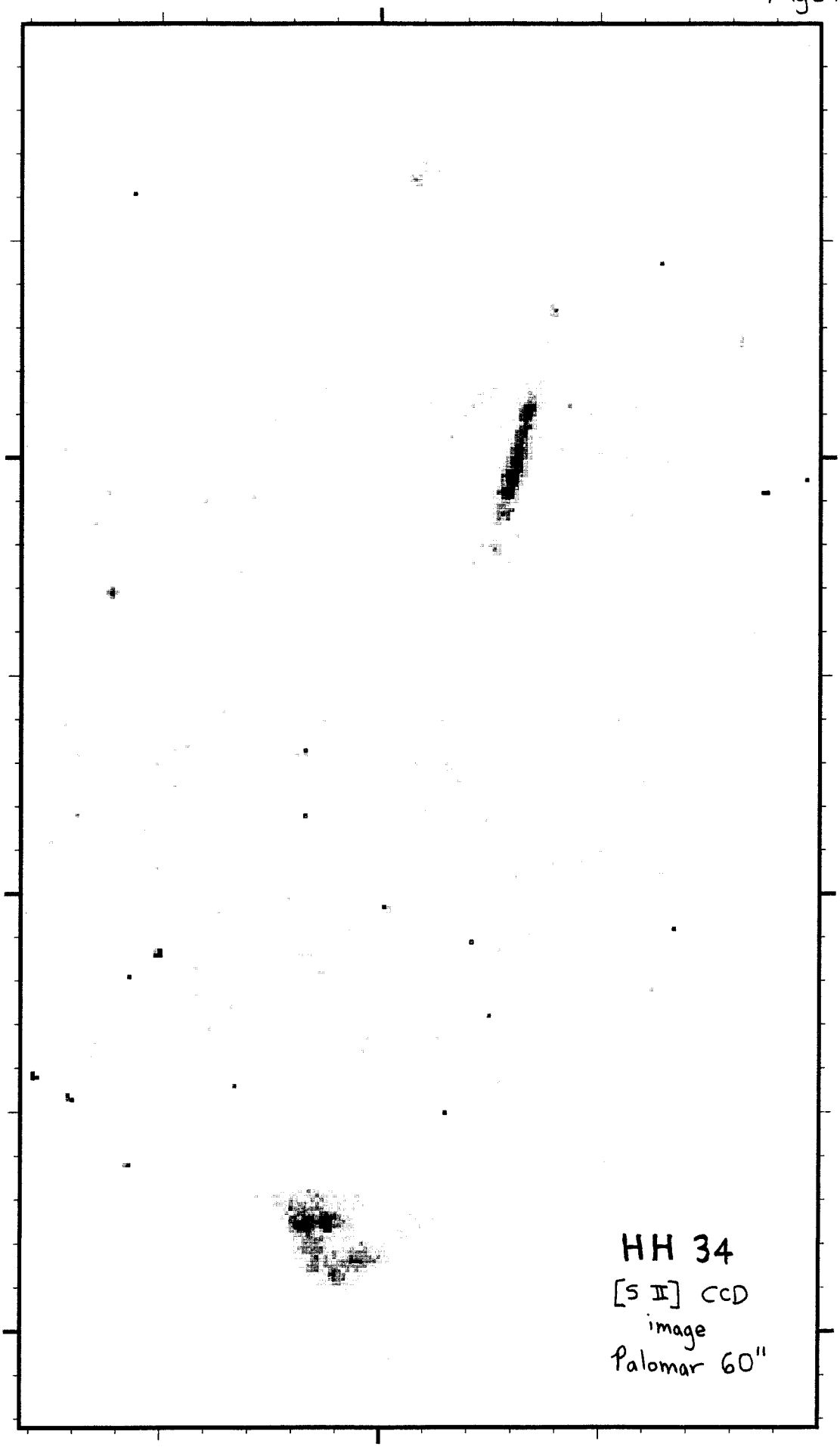

HH 34
[S II] CCD
image
Palomar 60"

CHAPTER II.

Near Infrared Emission Line Images of Three Herbig-Haro Objects

Abstract

HH 7-11, HH 12, and HH 34 have been observed with an infrared array camera using 9 narrowband filters. We report the first detection of the 1.64 μm line of [Fe II] in all three Herbig-Haro objects, including the HH 34 jet. Vibrational lines of H_2 were imaged in HH 7-11 and HH 12, but were not detected in HH 34. Brackett γ emission was not detected in any of the HH objects. The infrared results are compared with optical [S II] images. No new emission line regions are revealed in the infrared data, suggesting that extinction plays little role in determining the optical appearance of these HH objects. No infrared continuum emission was detected from any of the HH objects, indicating that none contain embedded stars. An infrared reflection nebula has been detected to the north of the HH 34 exciting star.

The spatial distribution of [Fe II] emission is generally similar to the distribution of 6717 Å [S II] emission. The [Fe II]/[S II] ratio is very different in HH 12E, where the value is down by a factor of 7 relative to the rest of HH 12. At this location we suggest that the cooling and recombining flow behind the shock is disrupted before the [Fe II] emission zone can form. In HH 7-11 and HH 12, H_2 emission peaks are nearly always accompanied by [Fe II] and [S II] emission. In three locations (western HH 7; eastern HH 12C and HH 12D) ionized gas peaks occur without H_2 counterparts; these locations all occur 2″-5″ upstream of H_2 emission. We identify these peaks without H_2 as shocked jet/wind material, displaced upstream from the

H_2 emission at the flow terminus. We suggest that the geometry of a flow obstacle controls whether or not the standoff distance between the molecular and ionized gas shocks is large enough to be observable.

I. Introduction

Herbig-Haro objects mark the locations where energetic winds from young stellar objects confront the dense quiescent gas of surrounding molecular clouds. The shock wave nature of HH objects, their association with bipolar molecular outflows, their often large proper motion, and their proximity to highly reddened young stars has been clear for several years (see Schwartz 1983 for a review). HH objects exhibit a wide variation in morphology (see Strom *et al.* 1986); for this reason, their specific shock geometries have been a matter of some debate. Discrete stellar mass ejections ("bullets"; Norman and Silk 1979) and ambient cloudlets in a supersonic stellar wind (Schwartz 1978) are models that have been proposed. Recently, many HH objects have been interpreted as collimated optical jets and jet working surfaces (Mundt, Brugel, and Buhrke 1987).

It is clear that there is much to be gained by studying HH objects at near-infrared wavelengths. The exciting stars of HH objects can usually be located only by infrared mapping since they are highly obscured at optical wavelengths. Extinction may also bias our view of the HH objects themselves; there are fewer known redshifted objects, *i.e.* those moving deeper into the host clouds. In addition, the near-infrared includes a unique spectroscopic tracer: the H_2 vibrational emission produced by shock-heated molecular gas. Using new infrared array detectors, it is now possible to obtain high-resolution images comparable to those at optical wavelengths. This new capability offers the opportunity for a detailed comparison of the molecular, atomic, and ionized gas tracers of the Herbig-Haro object shock fronts. The spatial relationship between the molecular and atomic emission should be indicative of the shock type and geometry within an individual HH object.

In this paper, we present flux-calibrated imagery in 5 emission line and 4 narrowband continuum filters for three classical HH objects. The emission lines studied ([Fe II], Brγ, and H_2 v=1-0S(1), 1-0Q(3), and 2-1S(1)) were chosen for imaging in order to selectively probe low-excitation ionized gas ([Fe II]), high-excitation ionized gas (Brγ), and the hot molecular gas shock fronts (H_2). Graham *et al.* (1987) have detected the 1.64 μm [Fe II] line in the spectrum of the supernova remnant IC 443 and suggested that it could be a useful tracer of ionized gas in low-velocity shocks. Futhermore, Hollenbach and McKee (1989) have carried out detailed modeling of the near-infrared emission line spectra of J shocks in molecular clouds and suggest that [Fe II] emission should be present in HH objects. Vibrational H_2 emission has been detected in many HH objects (ex. Schwartz *et al.* 1987). Near infrared imaging of H_2 emission has been carried out by several workers: Schwartz *et al.* 1988 (HH 43); Hartigan, Curiel, and Raymond 1989 (HH 7-11); Lane 1989 (Cepheus A, HH 24, HH 33-40, RNO 43N); and Garden *et al.* 1990 (HH 7-11, HH 12). The current contribution improves on the previous H_2 imaging in several respects. Narrowband continuum images were obtained to discriminate between line and continuum sources. Imaging was carried out in three H_2 lines, constraining the extinction and excitation conditions. All of the data has been flux calibrated; and lastly, careful registration of the infrared images with optical images has been done.

II. Observations and Reduction

The observations were carried out with the new Prime Focus infrared camera (Beichman *et al.* 1990) on the 5 meter Hale telescope during four observing runs from 1988 September to 1989 March. The detector was a Rockwell 128 x 128 HgCdTe array with reticon readout, 40% quantum efficiency from 1.6 μm - 2.45

μm, read noise of 1200 electrons, and a linear well depth of 6×10^5 electrons. The camera optics provide the detector with a 98″ field of view and 0.765″ pixels. The emission line images were made with 1% wide filters at 1.64 μm ([Fe II]), 2.12 μm ($H_2$1-0S(1)), 2.16 μm (Brγ), 2.24 μm ($H_2$2-1S(1)), and 2.42 μm ($H_2$1-0Q(3)). Narrowband filters that avoid strong emission lines were used to measure the continuum at 1.57, 2.08, 2.19 and 2.38 μm. Broadband J,H,K filter images were also obtained for reference.

The observing sequence consisted of taking object, bias, sky, and dark frames, and observations of standard stars. Exposure times in the narrowband filters were typically 500 seconds; Q(3) exposures were limited to 150 seconds by sky emission. All images were bias subtracted, dark subtracted, and flattened. Flat field frames were generated by taking the median of a number of normalized sky frames. The data were processed to remove low-level low spatial frequency noise present in the serial data stream from the camera. In each frame, "hot pixel" data values were replaced by a local median calculated over a 3 x 3 pixel box. Final images were constructed by co-adding several individual frames. The 98″ field of view was large enough to include the full areas of HH 7-11 and HH 12; however, three fields were required to cover HH 34. The narrowband images were flux calibrated using tracings of the cold filter transmission functions and observations of standard A-stars from the list of Elias *et al.* (1982). Our 3σ limiting surface brightness corresponds to about 4×10^{-5} erg s^{-1} cm^{-2} ster^{-1} in the emission line filters, and 0.04 Jansky/pixel in the continuum.

Calibration of the Q(3) line is more complex than for the other lines due to emission in the bandpass from the Q(1) and Q(2) lines as well as atmospheric extinction due to water vapor. The contribution of Q(1) and Q(2) can be estimated

in LTE using H_2 A-values from Turner, Kirby-Docken, and Dalgarno (1977). The ratios are: Q(1)/Q(3)=1, and Q(2)/Q(3)=1/3 with only 10% variation from $1500 < T < 2600$ K. After adjustment for filter transmission differences, we find that Q(3) makes up 49% of the line flux observed in the 2.42 μm filter. The atmospheric absorption correction is more difficult: narrow H_2O lines are located 25 km s^{-1} to the red of both the Q(3) and Q(1) rest wavelengths (Delbouille *et al.* 1981). The atmospheric extinction in the lines was estimated from Q(3) observations of HH 2 (V_{rad}= 25 km s^{-1} (Zinnecker *et al.* 1989)) at different airmasses. We found a Q(3) extinction of 0.2 magnitudes per airmass. We estimate the two corrections discussed above may introduce a 30 % systematic uncertainty in the derived Q(3) fluxes. The usefulness of Q(3) for revealing reddening variations within a field is unaffected by this uncertainty.

The optical [S II] frames were obtained during 1988 November using a TI 800 x 800 CCD at the Cassegrain focus of the Palomar 60 inch telescope. In the direct imaging mode with 2 x 2 on-chip binning the image scale was 0.49″ per pixel. The [S II] filter was centered on the 6717Å line and had a FWHM of 10Å. Hα frames (not presented here) were also obtained for reference. The CCD images were bias subtracted using the overscan of the serial registers and flattened against dome flats. Subimages were extracted to correspond to the infrared camera field size and aligned with the infrared images by applying a scale change and a small rotation. The optical and infrared images were then registered to a common origin using a reference star in the field.

The scale and rotation parameters were determined using a two step procedure. First, scale and rotation were determined astrometrically: for the infrared camera we used 19 Trapezium stars and positions from Herbig and Terndrup (1986); for the

CCD images we used 5 HH 34 field stars and positions from Strom *et al.* (1986). The astrometric method yielded a scale ratio of 1.556 ± 0.009 and a rotation angle of 0.5° ± 0.4° . These results were then checked against K band and Hα images of HH 12; a pair of stars separated by 67″ is visible in both frames. The vector between these two stars was measured in both the IR and CCD images, yielding an improved rotation angle of 0.2° ± 0.2° .

III. Results and Discussion

Images in [Fe II], H_2, narrowband infrared continuum, and optical [S II] were assembled together in Figure 1 for HH 7-11 and in Figure 5 for HH 12. For HH 34, broadband J, H, K, [Fe II], and [S II] images were assembled into Figure 7. Continuum emission from the HH objects was found to be negligible; we therefore chose not to subtract the continuum from the line images because of the added noise which would result. Individual objects in the fields are identified in the lower right panel of Figures 1, 5, and 7. The area of each object used for flux measurements in Table 1 was defined as the contiguous region of pixels where individual pixel values exceeded three times the single pixel noise σ measured in an empty area of each image. This aperture size determination was performed using both the [Fe II] and H_2 images; for each object, the largest aperture of the two was then chosen for all the line photometry. Intensity upper limits are calculated as 3σ, while flux upper limits are calculated as $3\sigma N^{1/2}$ (N is the number of pixels in the aperture). The derived peak intensity of an object was found by a weighted average of the brightest pixel with its four nearest neighbors.

A detailed justification for the identification of 1.64 μm emission as [Fe II] emission is given at the end of section III.

A. HH 7-11

HH 7-11 is a nearly colinear system of optical emission knots in the L1450 molecular cloud near NGC 1333 (see Strom *et al.* 1986). The estimated distance in 350 parsecs. The complex lies in the blue lobe of an outflow observed in 2.6 mm CO emission (Snell and Edwards 1981). A massive neutral atomic wind apparently drives this CO outflow (Lizano *et al.* 1988). The optical ionized gas emission lines are centered at LSR radial velocities of -200 to -40 km s^{-1} (Stapelfeldt *et al.* 1991; Solf and Bohm 1987). The H_2 1-0S(1) emission line is centered at much lower radial velocities of -60 to 0 km/sec (Carr 1990; Zinnecker *et al.* 1989), a fact important to shock models of the region. Rudolph and Welch (1989) have found zero velocity HCO^+ emission regions offset downstream of HH 8, 9, 10, and 11; they interpret this as evidence of shocked ambient cloudlets. The source of the outflow and exciting star of the HH emission is presumed to be the obscured star SVS 13.

None of the HH objects are evident in the 2.19 μm continuum image (Figure 1*b*). Continuum contamination is therefore insignificant in the line images of HH 7-11. SVS 13, the exciting star of the outflow, is the bright point source toward the upper right of Figure 1*b*.

i) [Fe II]

All of the optical HH objects are visible in the 1.64 μm [Fe II] line (Figure 1*d*). No optically invisible emission line regions are revealed in [Fe II]; from this we conclude that extinction has not strongly affected the optical appearance of the HH objects. The [Fe II] emission is spatially coincident with the optical [S II] emission except in HH 9, which appears extended 2″ further upstream (closer to SVS 13) in

[Fe II]. A knot of [Fe II] emission is seen adjacent to SVS 13, extending 4″ to the ENE. Faint [S II] emission (Figure 1e) is also seen in this knot, suggesting that the obscuring dust near the star does not extend over this knot of gas. HH 11 shows the highest [Fe II] surface brightness in this system.

ii) H_2

The Q(3) image (Figure 1*a*) shows the most intense H_2 emission in HH 7; HH 8 and 10 are moderately bright; HH 9 is faintly visible; and no H_2 emission is associated with the optical peak of HH 11. Two knots of Q(3) emission are present 3″ west and 7″ north of HH 11's optical position; these have no counterparts in the ionized gas. The H_2 peak to the north of HH 11, which we refer to as HH 11b, actually shows a better positional correspondence to Rudolph & Welch's HH 11 HCO^+ peak than HH 11 itself. There is also low-intensity H_2 emission coincident with the western edges of HH 11. Lastly, note the diffuse H_2 emission apparently filling the outflow cavity between SVS 13 and the flow terminus at HH 7.

The 1-0S(1) line image (not shown here) is virtually identical to the Q(3) image. Since these lines originate from the same upper state, their similar distributions imply that the foreground extinction is relatively uniform. The 1-0S(1) flux we derive for HH 7 agrees very well with the value found by Hartigan *et al.* (1989) in a 12″ aperture. The fluxes we obtained for HH 8 and HH 10 are smaller by 25% and 10% respectively, probably because of our smaller apertures. The diffuse emission west of HH 8 has a typical intensity of 0.3 erg s^{-1} cm^{-2} $ster^{-1}$ in the 1-0S(1) line.

A contour map overlaying the H_2 and [S II] emission morphology is shown in Figure 2. In HH 7, the H_2 morphology is significantly different from the [S II] morphology. The brightest [S II] emission originates in two peaks separated by 4″

along the flow direction; only one peak is present in H_2. The eastern [S II] peak coincides (to the limits of our resolution and image registration) with the H_2 peak. However, there is a significant difference between the shape of the [S II] peak and the shape of H_2 peak at this location: the H_2 emission is more extended perpendicular to the flow axis. This is shown quantitatively in Figure 3. A plot of intensity versus position along a line passing through the eastern peak at PA 200° reveals that the [S II] peak FWHM= 4.4″, [Fe II] peak FWHM= 4.7″, but the the H_2 FWHM= 6.2″ (see Figures 3*a*, 3*b*, 3*c*). These results are derived using a swath 4″ wide and are therefore insensitive to infrared-optical image registration uncertainties. The western [S II] peak has no H_2 counterpart; it does, however, correspond to the position of brightest [Fe II] emission in HH 7.

Our results for HH 8 and HH 10 differ from those of Hartigan, Curiel, and Raymond (1989). HCR's Figure 2 depicts significant ($\approx$ 3″-5″) spatial offsets between the H_2 and [S II] peaks in these objects. Our data do not confirm this: we find no offset at the southern peak of HH 8, and at most a 1″ offset at northern HH 8 and at HH 10. There is reason to believe our image registration is more reliable: the large field of view of our array covered all of HH 7-11 and a reference star, whereas HCR used a smaller array that demanded mosaicing without available reference stars. Furthermore, we find the infrared [Fe II] peaks are coincident with the [S II] peaks to within 1″ in HH 8 and HH 10. This result, which is physically reasonable given the similar low excitation characteristics of the two emission lines, confirms that we have good optical-infrared image registration and thus that there are no H_2 - [S II] offsets as large as 3″ in HH 8 and HH 10.

The 2-1S(1) emission (see Figure 1*c*) is clearly detected in two locations: at the brightest source of v=1-0 emission (HH 7) and in an extension to the NE of

SVS 13. The aperture photometry also shows 2-1S(1) emission in HH 8 and HH 10. Using the *integrated* flux values for HH 7 given in Table 1, we obtain a v=1-0/2-1 ratio of 11. This is consistent with the results of Burton *et al.* (1988). The ratio at the emission *peak* is only 5, however, implying that the H_2 excitation conditions vary with position within HH 7. Models predict this line ratio to be dependent on the H_2 vibrational temperature, the ultraviolet radiation field, and the degree of molecule re-formation taking place (Hollenbach & McKee 1989). The knot of 2.24 μm emission 7″ NE of SVS 13 is enigmatic: it is displaced 2″ north of an [S II]-[Fe II] peak; it is present in all of the 2 μm images, including the continuum; and it is most prominent at the 2-1S(1) wavelength. If interpreted as H_2 line emission, the knot's v=2-1/1-0 ratio is 2. This value is much higher than predicted by either the shock-excitation or ultraviolet fluorescence excitation mechanisms for H_2.

iii) Interpretation

In a two-dimensional axisymmetric flow, a collimated stellar wind can produce two different shock geometries where the wind encounters an obstacle. Sketches of these two situations are shown in Figure 4. Figure 4*a* shows the shock structure associated with the termination of a jet; and Figure 3*b* shows the shock structure around a small clump of material being acted on by a jet. The most essential difference between these two situations is the relative sizes of the jet and the obstacle. In Figure 4*a*, depicting the flow terminus, the jet width is much less than the obstacle size; the ambient medium is very large. In Figure 4*b*, the jet width is much greater than the obstacle size. In both of these scenarios, two separate shock emission regions are expected: one from within shocked wind material, and a second from within shocked ambient material. A bow shock is present in both the jet terminus

and shocked cloudlet scenarios, but with different characteristics in each. At the jet terminus (4*a*), a moving bow shock occurs in the ambient medium and is concave open toward the flow source. In the case of a cloudlet (3*b*), a stationary bow shock occurs in the wind material and is concave open away from the flow source. These Figures are similar to the Figures of Schwartz (1978), Hartigan (1989), and Zinnecker *et al.* (1989).

In the case of a neutral atomic wind flowing into a molecular medium (as Lizano *et al.* 1988 report is the case for HH 7-11), shocked wind material should not produce H_2 emission. Any H_2 emission detected in such a flow must originate in regions of shocked ambient material. Therefore, for those HH objects where near-infrared H_2 emission is detected, it should be possible to infer whether a given HH emission knot is shocked ambient material or shocked wind material on the basis of the presence or absence of H_2 emission. This discriminant will prove useful in our discussion of the shock structure within HH objects.

A key difference between these two types of HH objects shown in Figure 4 should be the magnitude of the distance between the emission due to the shock in the wind material and the emission due to shock in the obstacle material. The displacement between these shocks reflects the amount of material which is present between them, which in turn is a function of the geometry of the obstacle. In the case of a small clump of material immersed in the flow (4*b*), there is little geometrical containment of the postshock gas. Shocked wind material is free to flow around the obstacle and continue downstream. Shocked ambient material at the surface of the clump may become entrained in the flow and carried away as well. Both of these mechanisms suggest that it is unlikely that a great deal of material will accumulate between the shock emission regions. The displacement bewteen the

two shocks in this case will be determined by the standoff distance of the bow shock from the front side of the obstacle. For high Mach number flows, this standoff distance will be significantly smaller than the cloud (see Figure 1 of Raga and Bohm 1985). Therefore, the displacement between the shocked wind material and shocked obstacle material can be significantly smaller than the size of the obstacle itself. Thus, even for a cloudlet which is itself resolved, the displacement between the bow shock emission and cloud shock emission could still be unresolved. It is therefore plausible that a shocked cloudlet may exhibit little or no observable offset between the position of its peak Hα , [S II] emission and the position of its peak H_2 emission.

In the cloudlet case just discussed, the dynamic pressure of the flow acts to move the postshock material away downstream. This does not occur in the case of a flow terminus geometry, where shocked jet material and shocked wind material accumulate in a geometrically closed region. The terminal jet shock will occur where the jet strikes this accumulated material — a location distinctly separate from the bow shock in the ambient medium. The visibility of this terminal jet shock has been discussed by Hartigan (1989). The separation of the two shocks in this scenario should be significantly larger the shock separation in the cloudlet scenario — probably comparable in size to the width of the jet.

The two separate [S II] peaks in HH 7, one of which does not have an H_2 counterpart, suggest that two distinct shocks are indeed present in HH 7. The absence of HH objects to the east of HH 7, coupled with the object's bow shape (concave open to SVS 13), makes it clear that HH 7 is the eastern terminus of the outflow from SVS 13. Using the flow terminus model, we identify the western [S II] peak in HH 7 as the location of the terminal jet shock. The eastern [S II]

peak (and the peak H_2 emission) then correspond to the bow shock in the ambient molecular medium. Hartigan, Curiel, and Raymond (1989) have also discussed this interpretation. This model naturally accounts for the lack of a western H_2 peak: the terminal jet shock is occurring entirely within wind material where very little H_2 is present. The model is also supported by new imaging spectroscopy of HH 7-11 (Stapelfeldt *et al.* 1991) which shows that much of the intensity of HH 7's western [S II] peak originates from a -100 km s^{-1} high velocity component not present in eastern HH 7.

There is both kinematic and spatial evidence for separate H_2 and [S II] formation regions in the bow shock on the eastern edges of HH 7. First is the radial velocity data: Carr (1990) and Zinnecker *et al.* (1989) find much lower H_2 velocities than Stapelfeldt *et al.* (1991) and Solf & Bohm (1987) find for [S II] and Hα in HH 7. Secondly, as we reported above, the H_2 peak is more broadly extended perpendicular to the flow direction than the [S II] peak that it spatially coincides with. Greater extinction at the periphery of HH 7 does not account for this, as the infrared [Fe II] distribution essentially matches the optical [S II] distribution. Excitation gradients caused by the variation in effective shock velocity over the bow shock surface are probably not large enough to account for the observed peak shape variations. A very plausible explanation for the observations is that the region of bright H_2 emission is located *exterior* to the more axially concentrated [S II] emission.

Separate H_2 and [S II] emission regions are expected if the HH 7 bow shock takes the form of a J shock with a magnetic precursor, as proposed by Hartigan, Curiel, and Raymond (1989). This model predicts that the H_2 emission forms where the shock precursor heats and accelerates the preshock molecular cloud material;

with a flow terminus bow shock geometry, the precursor H_2 emission will form in a shell *exterior* to the region of [S II] emission from the J shock itself. An alternate molecular emission scenario predicts that the H_2 emission will form in the cooling zone behind a shock, perhaps with a significant contribution from molecule reformation processes (Hollenbach and McKee 1989). In a flow terminus bow shock geometry, this scenario would have the H_2 emission forming in a shell *interior* to the [S II] emission in the post-shock cooling zone. We see no obvious way for such interior post-shock H_2 emission to be more broadly extended from the bow shock axis than [S II] emission, as our observations show is the case in eastern HH 7. It seems straightforward, however, for an exterior shell of H_2 emission to appear more broadly extended from the bow shock axis than an interior shell of [S II] emission. On these geometrical grounds it therefore appears likely that the brightest H_2 emission in HH 7 is excited by a magnetic precursor.

In the case shown in Figure 4*a*, which we apply to HH 7, the jet is in rough pressure equilibrium with the surrounding material (region 1). Region 1, in turn, is probably close to pressure equilibrium with the ambient material (region 0). The region between the jet shock and the shock driven into the ambient material (region 2) must satisfy $p_2 \approx \rho_s v_s^2$, so $p_2 >> p_1$ and $p_2 >> p_0$. Region 2 is filled with shocked jet and ambient material at high pressure, which then flows out into region 1. It is possible (but not necessarily the case) that there is a shock transition between region 2 and region 1 arising from the effective venturi formed by the jet and the opening walls of the cavity.

It does not have to be the case that $p_1 = p_0$. If the cavity around the jet is mostly enclosed, then the energy input from the jet will pressurize the cavity. If $p_1 > p_0$, then weak shocks will be driven into the cavity walls. Such shocks could be

the source of the diffuse ubiquitous H_2 emission in HH 7-11. It should also be noted that there will be a velocity shear across the contact discontinuity between shocked jet and ambient material. The shocked jet material will be primarily flowing along the discontinuity on its way out of region 2; at the same time, ambient material is shocked and enters region 2. The contact discontinuity will be Kelvin-Helmholtz unstable and mixing will occur. Thus, distinctions between emission from regions of shocked jet material and regions of shocked ambient material may be largely artificial in some cases. In particular, mixing of molecular material not dissociated by the bow shock with the warm atomic gas in region 2 could be a significant additional source of molecular emission. This mixing could also significantly complicate interpretation of high resolution spectroscopy of HH objects.

Some of the atomic emission extended perpendicular to the flow in HH 7 could also be due to shocked jet material. If material remains in region 2 for a time which is less than or comparable to the time scale for radiative cooling and recombination of the emitting species, then the emissivity will be high throughout this region of high pressure. In this case, the spatial extent of the emission from region 2 would be similar to the spatial extent of bow shock emission because the pressure in region 2 drives the bow shock.

The nature of HH 8, HH 9, and HH 10 is not as easy to discern as that of HH 7. Rudolph and Welch (1988) interpreted the zero-velocity HCO^+ peaks just to the east of these objects as shocked cloudlet emission. For the purpose of discussion, let us assume that HH 8, HH 9, and HH 10 are shocked molecular cloudlets in a neutral wind. If so, we would expect the cloudlet shock to produce both bright H_2 emission and the HCO^+. Our observations show that the peak H_2 emission in HH 8, HH 9, and HH 10 is nearly coincident with the optical [S II] peaks. This means that the

H_2 peaks are *also* located upstream (by 3″-8″) of the HCO^+ peaks. A naive cloudlet model might not have expected the H_2 and HCO^+ peaks to be spatially separated. In the context of the cloudlet model, this observation can be best understood if the H_2 emission forms in warm post-shock gas and the HCO^+ emission arises in the cold pre-shock medium. The HCO^+ emission is then most likely excited by a radiative or magnetic precursor of the cloudlet shock, by weak shocks acting on the rear of the cloudlet, or by the simple high density of the undisturbed cloudlet material.

We do not feel that Rudolph and Welch's (1988) original suggestion, that the HCO^+ emission arises in dense gas compressed by the cloudlet shock, can be easily reconciled to the observed spatial relationship between the HCO^+ and H_2 peaks. If a single cloudlet shock was responsible for both the HCO^+ emission (by compressing the gas above the HCO^+ J= 1-0 critical density) and the H_2 emission (by heating the H_2 to near 2000 K), then the shock must be located just to the east of the HCO^+ peaks. This implies that the HCO^+ emission region must lie closer to the shock than the H_2 formation region. For radiative shocks, this assumption further implies that the HCO^+ emission should form in a region of higher temperature than the region of H_2 emission. However, this cannot be the case: because the observed HCO^+ emission originates in a level only 4 K above the molecular ground state, we expect essentially no J=1-0 HCO^+ emission to form in regions as warm (2000 K) as those where 2 μm H_2 emission originates. We therefore conclude that the HCO^+ and H_2 emission in HH 8, HH 9, and HH 10 cannot *both* be excited in the material that has completely passed through a single cloudlet shock.

An alternative explanation that would still allow HCO^+ formation in the shocked gas is the following: if the cloudlet shock was of very low velocity (a few km s^{-1}), it could potentially produce the HCO^+ peaks via compression without

producing detectable H_2 emission. In this case, the weak cloudlet shock would be located just to the east of the HCO^+ peaks. However, another mechanism is needed in this case to explain how the emission from warm H_2 is formed several arcseconds to the west. It may be that the entrainment of cloudlet material by the neutral wind can produce the H_2 emission on the cloudlet's upstream surface.

The lack of a significant H_2 - [S II] offset in HH 8, HH 9, and HH 10 is not a problem for a cloudlet model of these objects. As discussed earlier in this section, the spatial separation between wind and cloudlet shocks can be unresolved even for a resolved cloudlet. Morphology is another issue. In H_2 and [S II], neither HH 8 or HH 10 has the appearance of an idealized cloudlet (Figure 4*b*): there is no identifiable bow shock structure, and axial symmetry is lacking. However, we believe that a non-ideal cloudlet is still a viable model for HH 8 and HH 10. A flow obstacle that has an irregular non-spherical shape, or one which is partially embedded in the outflow cavity wall can break the symmetry in Figure 4*b*. Regardless of the shape of the obstacle, we expect that both the wind and obstacle material will be shocked and produce emission. If the wind is neutral, the shocked wind material may be evident as a bright [S II], Hα emission knot that has no H_2 counterpart. Such peaks are present in both HH 8 and HH 10: in HH 8, at the northwestern tip; and in HH 10, near the geometric center of the object. In both cases, an Hα - H_2 comparison reveals these peaks most clearly (see Hartigan, Curiel and Raymond 1989). The presence of these shocked wind peaks adjacent to the H_2 peaks in HH 8 and HH 10 suggests that a flow obstacle model is a viable explanation for these objects.

HH 11 does not seem to fit either of the two pictures depicted in Figure 4. A nearby HCO^+ cloudlet appears to be associated with HH 11b, not HH 11 itself; the line profiles do not include zero velocity (chapter III; Solf & Bohm 1987); and

there is no H_2 emission. The lack of molecular emission from HH 11 suggests one of two situations: either the material being shocked is not molecular gas, or the shock itself is strong enough to dissociate molecules before any emission is excited.

The absence of molecular emission also indicates that no molecule formation is occuring in a post-shock cooling zone at this location. This may not be a strong test of model predictions of molecule formation in shocks, however, since the object may be too young for molecular formation to be important yet. From the models by Hollenbach and McKee (1989), the column depth required for significant H_2 emission from the zone of molecule formation is $\sim 3 \times 10^{20}$ cm^{-2}. For $v_s = 50$ km s^{-1} and $n_0 = 10^3$ cm^{-3}, it takes about 2000 years to accumulate this column depth. This is long compared to the dynamic time scale of 300 years inferred from the proper motion of the object and the distance to the source (Herbig & Jones 1983).

The essential features of 4*b* are similar to 4*a*, with shocked jet material confined for a time in the high pressure region 2 between the jet and cloud shocks. As with 3*a*, $p_2 >> p_0$ and $p_2 >> p_1$, and the possibility exists for a shock transition between region 2 and region 1. The time scale for confinement of shocked jet material in region 2 will be shorter for Figure 4*b*. As shocked material escapes from region 2, its emissivity will drop abruptly and dramatically. This is due to the combined effects of lower density and mechanical cooling that occur as a result of the expansion. For example, the Boltzmann factor for the ^2D level of S II changes from .13 to .02 between 10000° K and 5000° K. This phenomenon of incomplete cooling and recombination is discussed below in the case of HH 12E.

B. HH 12

HH 12 is one of the more extended complexes of Herbig-Haro objects, measuring 30″ x 50″ in size. It is located in L1450 approximately 5′ NW of HH 7-11. The optical emission knots of HH 12 are blueshifted with respect to the ambient cloud and are coincident with the blue lobe of a CO outflow (Edwards and Snell, 1983). Unlike HH 7-11, the outflow source has not been postitively identified. The infrared source SVS 12, located 20″ to the east of HH 12, has been suggested as the exciting star (Strom, Vrba, and Strom 1976; Edwards and Snell 1983; Cohen and Schwartz 1983). However, the proper motions of HH 12B and HH 12F are directed toward the north (Herbig and Jones 1983), roughly perpendicular to the direction of SVS 12. It is difficult to reconcile this result with an outflow from SVS 12. K. Strom *et al.* (1983) suggested that a star 2′ to the south is the outflow source, but additional observations failed to confirm this (K. Strom *et al.* 1986). New arguments supporting a case for SVS 12 as the HH 12 exciting star are presented by Stapelfeldt (1991) and Stapelfeldt *et al.* (1991) on the basis of the local molecular gas distribution and [S II] radial velocities. On the basis of these we adopt SVS 12 as the exciting star in the discussion below.

The near-infrared luminosity of HH 12 is predominantly line emission; continuum images (such as 2.19 μm, Figure 5*b*) show no significant emission. The brightest source in this field is SVS 12 and its reflection nebula, which are discussed below.

i) [Fe II]

As was the case for HH 7-11, all of the HH 12 optical emission knots are also present in [Fe II] (see Figure 5*d*). There are no additional emission features seen [Fe II] 1.64 μm which were not already apparent in the optical emission line morphology. To the limits of our resolution and image registration, the [Fe II] and

[S II] emission peaks are spatially coincident. HH 12B shows the highest [Fe II] surface brightness within HH 12.

HH 12E is an exception to the generally good agreement we see between [S II] and [Fe II]. At this location, [S II]/[Fe II] is a factor of 7 higher than typical in other nearby knots. This is difficult to interpret using steady flow shock models, which indicate that [S II]/[Fe II] should be fairly constant for shock velocities in the relevant range (Hollenbach and McKee 1989). A deficit of [Fe II] emission from the shocked wind material can be explained by incomplete cooling of the postshock gas. This idea has been used to explain similar discrepancies between observations and shock models in supernova remnants (see Raymond *et al.* 1988 and references therein). The second ionization potentials for S and Fe are quite different (23.3 eV versus 16.2 eV). Assuming a shock velocity adequate to ionize S, there should be a significant region in the cooling and recombining flow behind the shock where Fe is predominately Fe^{+2} while S is predominately S^{+}. If too little material has passed through the shock for the Fe^{+} zone to form, or if the geometry of the flow is such that material behind the shock never cools enough to produce much [Fe II] emission, then the the [S II]/[Fe II] ratio can become larger. The geometry of HH 12E appears consistent with a small cloudlet (Figure 4*b*) or a protrusion into the flow, and it is likely that shocked wind material is confined to the zone between the bow shock and cloudlet shock for a short time only. In this interpretation, the region of molecular formation would also be absent behind the bowshock, so the H_2 emission from HH 12E must originate from a separate shock in the cloudlet material. This scenario admittedly requires that the shocked flow in HH 12E somehow be "disrupted" at a fairly special place; however, we point out that of the objects observed, HH 12E is the only one with a significantly anomalous [S II]/[Fe II] ratio. Model calculations showing the [S II] and [Fe II] emission as a function of column depth would enable

a more quantitative analysis of HH 12E.

ii) H_2

Figure 6 shows the spatial relationship between the [S II] and H_2 emission in HH 12. The morphology of the H_2 emission is remarkably different from the optical emission lines. The Q(3) emission (Figure 5a) in knots B, C*w*, E and G is coincident with the [S II] and [Fe II] emission (Figure 5e). Significant offsets are evident, however, the cases of knots C, D, and F. Peak H_2 Q(3) emission occurs 2″ west of the [S II] peak in knot C. The H_2 counterpart of knot D (referred to here as knot D*m*) appears 8″ west of its optical counterpart (D*i*). Faint Q(3) emission associated with knot F lies 8″ SW of the corresponding optical emission.

All three of these H_2 - [S II] offset vectors point back towards SVS 12. In addition, Q(3) knots we call C*n* and C*w* appear north and west of optical knot C. Small [S II] knots coincide with C*n* and C*w*. Finally, there is a knot of Q(3) emission, colinear with SVS 12 and optical knot G. This H_2 feature has no optical counterpart; we designate it HH 12H. The morphology of the S(1) emission image (not shown here) is very similar to the Q(3) emission in Figure 3a. The 2-1S(1) emission was detected only in knot E and the peak v=1-0/2-1 ratio is 16.

In HH 12, the molecular hydrogen emission tends to be distributed in discrete clumps; the optical emission includes and extends between these clumps. This is a real effect and is not due to infrared sensitivity limitations: the [S II] intensity between knots D and E is about a factor of 3 reduced from the value on the peaks. Limits for the H_2 emission between these knots show that the knot/interknot intensity ratio here is greater than 10. This result suggests that HH 12's H_2 emission is predominantly formed in clumps of ambient medium shocked by the pressure of

the stellar wind.

HH 12 has the appearance of the termination of a wide opening angle conical flow from the east against the approximately N-S boundary of a molecular cloud. The morphological properties of HH 12 can be interpreted under this assumption as follows: The eastern-most knots in the system are either small cloudlets (E, G) or dense protrusions into the flow (B) that have not yet been eroded away. There is no measurable displacement between the molecular and atomic emission in these knots; as was discussed in the previous section, a cloudlet geometry is consistent with this observation. The diffuse atomic emission (between knots B-C; D-E; E-F) arises from shocked wind material that is ubiquitous throughout these regions. The emission along the western edges of HH 12 represents the termination of the flow, and here offsets are found between the molecular and atomic emission. Knots C*n*, C*w*, and D*m* show both H_2 and [S II] emission from the shocked ambient medium. In knot D*i* and in the eastern side of knot C, only shocked atomic material is present. Here, as with HH 7, enough material 'piles up' for the shocked wind material to be offset an observable distance upstream from the shocked ambient material.

iii) Continuum

The bright infrared continuum source in this field is SVS 12 and its reflection nebula. The star itself is located at the extreme southeastern tip of the near-infrared reflection nebulosity; both the star and the nebula are highly obscured at optical wavelengths (Figure 5*e*). The axis of the nebula is aligned well with the line formed by SVS 12, HH 12G, and HH 12H. This appears to bolster the suggestion made by Cohen and Jones (1987), that an outflow from SVS 12 is responsible for the shock excitation of HH 12G and HH 12H (see also Garden *et al.* 1990). If SVS 12 is the

exciting star for all of HH 12, then the outflow must take the form of a broad cone (half angle ~40°) to encompass all of HH 12. In this view, the axis of the reflection nebula forms the NE boundary of the cone; the SE boundary follows the SVS 12 - HH 12F line.

The stellar continuum source SVS 12 has some striking characteristics. Very strong circumstellar extinction is evident from a comparison of the K and J band images (Figures 5*a* and 5*c*). The star is hardly visible at J; we find (m_J - m_K)≥ 6 mag. The reflection nebula is substantially less reddened: (m_J - m_K)= 3 mag. Embedded objects with extremely red J - K colors have been studied by Myers *et al.* (1987), who suggested that these are very young stars (T_{eff} ~3000 K) extincted by 20-30 magnitudes. The strong localized reddening indicates that SVS 12 may possess a substantial circumstellar disk.

The J band image (Figure 5*c*) shows several locations of significant emission which are not present in any of our narrowband continuum images (such as the 2.19 μm image shown in Figure 4*b*). The J features are spatially coincident with the HH 12 optical knots B,C,D,E, and F, and they exhibit similar morphology. This close association with known emission line regions, coupled with the observed lack of near-infrared continuum emission from those regions, strongly argues that we are observing line emission in the J image. A definite source of line emission in the J band (1.15-1.40 μm) is the 1.257 μm [Fe II] line which arises from the same upper state and has nearly equal transition probability as the 1.644 μm line. This is undoubtedly the primary source of the J band emission seen. This cannot be the whole explanation, however, since knot E should be relatively faint if [Fe II] 1.257 μm emission dominated its J flux. Paschen β (1.281 μm) may account for the remaining emission from knot E.

C. HH 34

HH 34 is located in the L1641 cloud in Orion. Mundt (1986) and Reipurth *et al.* (1986) independently discovered a highly collimated jet pointing toward HH 34 from an optically faint star 110″ to the north. They realized that HH 34 itself is probably the "working surface" of this jet, a bow shock formed where the jet actively carves out a cavity in the ambient medium. A symmetrically placed bow shock on the northern side of the star was found by Buhrke, Mundt, and Ray (1988). They designated the northern bow shock as HH 34N, and renamed the original object HH 34S. One of the intriguing aspects of this star-jet-shock system is the apparent lack of a jet directed toward HH 34N. Three fields were observed by us: the star/jet, the southern bow shock, and the northern bow shock. Figure 7 shows our infrared images of the star/jet field.

i) [Fe II]

The HH 34 jet is the only line emission feature in the [Fe II] image, Figure 7*d*. It is of interest to compare the [Fe II] spatial structure of the jet with the known [S II] structure, and this comparison is shown in Figure 8. The [Fe II] profile of the jet is very similar to the [S II] profile; the only prominent difference is the slightly lower spatial resolution of the [Fe II] data. The similarity of the optical and near infrared ionized gas emission line structure suggests that the lack of emission between the star and the bright knots of the jet is not due to local extinction. There is also strong [Fe II] line emission from the position of the star: in our 1% filters, the 1.64 μm flux density is 5 mJy and the 1.57 μm flux density is 2 mJy. Assuming that no other lines fall in our filter bandpass and that the 1.64 μm [Fe II] linewidth

is 100 km s^{-1}, the 1.64 μm [Fe II] emission line intensity must exceed the stellar continuum by a factor of twenty.

Figure *7d* shows no evidence of a counterjet in [Fe II] to the north of the HH 34 star. If the counterjet were as intrinsically bright as the southern jet, then it would have to be extincted by at least 3 mag at 1.64 μm to escape our detection. This corresponds to 14 mag at [S II] 6717Å. There are two reasons why such a large optical extinction seems implausible in the region where a counterjet is expected. First is the Hα flux ratio of 0.1 we measure between HH 34N and HH 34S. Assuming these two objects to be of comparable intrinsic brightness, this observation implies that the extinction toward HH 34N exceeds that toward HH 34S by only $A_{H\alpha} = 2.5$ mag. Secondly, ^{13}CO millimeter interferometry of the HH 34 star region (Chapter IV) shows that the dense circumstellar gas is confined to an area within 10″ of the HH 34 star. The spatial extent of this gas is therefore insufficient to obscure a northern jet of length equal to the southern jet ($\sim$ 20″). We therefore conclude that the primary reason for our non-detection of a northern jet is its intrinsic faintness in [Fe II] relative to the southern jet. The collimated flow to the north is therefore encountering little lateral confinement (and thus no shock interactions with the ambient medium) as it makes its way to the bow shock at HH 34N. A remaining speculative possibility is that the jet source mechanism is somehow intrinsically asymmetric in nature.

HH 34S is only a weak source of 1.64μm emission in comparison to the jet (image not presented here). The [Fe II] again appears to follow the optical [S II] distribution, but the details cannot be precisely determined because of image alignment uncertainties: there is no reference star in this field visible at both optical and infrared wavelengths. The bow shock [Fe II] flux may be weak because only a

single shock is present here; in the jet, multiple oblique shocks allow many [Fe II] emission regions. HH 34N was not detected in our [Fe II] observations. This non-detection requires that the total [Fe II] flux from HH 34N must be at least a factor of three less than the flux from HH 34S. The observed optical brightness ratio of these objects (a factor of ten) easily accounts for the HH 34N [Fe II] non-detection without any effects of extinction.

ii) H_2

Molecular hydrogen emission was not detected in any of the 3 HH 34 fields. The absence of H_2 emission from both bowshocks may reflect the prevalence of relatively low density molecular gas in the environs of this object. The widespread Hα emission in this field suggests a significant atomic component to the local ambient medium. If the ambient medium H_2 volume densities were below 10^3 cm^{-3}, the emissivity of the H_2 shocks would be low enough to render them unobservable.

The lack of H_2 emission from the HH 34 jet suggests that the jet may not contain any molecular material. The very low excitation spectrum of the jet is indicative of a physical environment which should be ideal for producing H_2 emission, yet none is observed. It may be that the jet density is also too low to produce observable H_2 emission; future observations with higher sensitivity may be able to provide definitive limits on the molecular fraction of the jet material.

iii) Continuum

Along with the HH 34 star near the center, two other stars in this field are obscured in the optical (See Figure 7*a-c*). One is 20″ to the west and is located

at the position of optical reflection nebulosity; the other is in the upper left of the images, and corresponds to Cohen and Schwartz (1983)'s HH 34 IRS 5. Our position for IRS 5 is α= $05^h33^m04.8^s$ δ= -06°28′26″ (1950), or 5″ NNE of Cohen and Schwartz's position. IRS 5 illuminates two patches of reflection nebulosity to its south and west. Faint jet emission is apparent in the J image, probably originating from the [Fe II] 1.257 μm line.

An interesting feature of the continuum images is the diffuse emission north of the HH 34 star. The emission is brighter at longer wavelengths, and in the K image (Figure 7*c*) appears to be concentrated around a distinct source. Recent millimeter-wave interferometry of the HH 34 star (Stapelfeldt 1991) reveals extended ^{13}CO J=1-0 emission in this region and the suggestion of a condensation at the position of the spot. It is unclear if this region is solely reflection nebulosity or if it also contains a separate, highly obscured stellar source. K band polarization measurements and high resolution 5 μm images of this field would be very useful for resolving this uncertainty.

D. Why the 1.64 μm emission must be [Fe II]

We have confidence that the emission detected in our 1.64 μm filter is in fact [Fe II] emission. First, there is no doubt that we have detected line emission at 1.64 μm: none of the HH objects we have discussed were detected in our 3% bandwidth 1.57 μm images. In the HH 34 jet, 1.64 μm [Fe II] line emission is expected because this object is known to be a strong emitter in the 8617 Å [Fe II] line (Reipurth *et al.* 1986). Furthermore, the fact that no H_2 1-0 S(1) or 1-0 Q(3) line emission is detected in the jet makes it very unlikely that higher-level H_2 lines (such as 3-1 O(7) and 6-4 Q(5)) could be present at the intensity required to account for the

observed 1.64 μm emission (see Black and van Dishoeck 1987). In HH 7-11 and HH 12, the observed distribution of 1.64 μm emission correlates well with 6717 Å [S II] emission, but does not follow the H_2 emission: crucial examples of this are found in western HH 7, HH 11, and HH 12D, where [Fe II] peaks appear coincident with [S II] and no H_2 emission peaks are present. Lastly, our wide-band J images of HH 12 and the HH 34 jet show faint but definite signs of the HH objects, as expected from the presence of the 1.26 μm [Fe II] line in the filter bandpass. Neither object is known to posess a significant continuum component in the optical or near-infrared. We therefore conclude that we have a strong basis for associating our observed 1.64 μm emission with [Fe II].

IV. Conclusions

The principal results of our high resolution, near infrared imaging of HH objects are:

(1) 1.64 μm [Fe II] emission has been detected in HH 7-11, HH 12, and HH 34. Its morphology resembles that of the red [S II] lines. The intensity of [Fe II] is typically 20 % that of H_2 1-0S(1). This line should be an excellent tracer of shocked ionized gas in highly obscured regions, and along with 1.26 μm [Fe II] measurements will allow an accurate determination of the local extinction. Variations in the [Fe II]/[S II] ratio within the HH object complexes we studied are generally small except in HH 12E, where the ratio is down by a factor of 7 relative to other knots in the object. At this location, incomplete cooling and recombination in the flow behind the shock can account for the exceptionally weak [Fe II].

(2) Extinction appears to be unimportant in determining the morphology of

these HH object systems. Standard extinction curves predict that the extinction in magnitudes at the 1.64 μm [Fe II] line is nearly five times less than that at the 6717 Å [S II] line yet no new regions of shock ionized gas were found at 1.64 μm. In addition, the H_2 Q(3) and S(1) line images appear very similar. Thus, the distribution of optical and near infrared line emission in these HH objects is dictated by hydrodynamic conditions rather than the distribution of absorbing dust. The outflow source stars themselves are highly obscured, however, which indicates the presence of substantial circumstellar dust.

(3) No near-infrared continuum emission was detected from any of the HH objects implying that these regions do not contain embedded stars. An infrared reflection nebula, possibly containing a new point source, has been discovered north of the HH 34 exciting star.

(4) At positions where the flow terminates against a large obstacle (HH 7 and the western portion of HH 12), there are significant offsets between the shocked flow material and the shocked ambient medium. At these locations the geometry is such that significant amounts of material can 'pile up' between the jet shock and the shock driven into ambient material, leading to an observable displacement between the two shocks. At locations where a flow is interacting with small clumps of ambient material (HH 9, HH 12E, etc.), the wind shock and ambient medium shock are generally coincident (within the limits of our resolution). At these locations the standoff distance between the wind and cloud shocks is expected to be smaller. The data fit an interpretation in which shocked jet/wind material is a source of atomic emission only, whereas shocked ambient material produces both molecular and atomic emission.

(5) We have observed a significant difference between the shapes of the H_2 and [S II] emission peaks on the east side of HH 7. The broader H_2 peak suggests that bright molecular emission is formed in a region *exterior* to the [S II] emission, as expected if the H_2 emission arises within a magnetic precursor.

The work described in this paper would not have been possible without the many years of dedicated work by JPL's Gary Bailey in developing infrared arrays for astronomical use. Gary died in January 1990. His insight into the practical applications of arrays, his trenchant wit and unwavering dedication to the progress of science will all be sorely missed by his colleagues.

It is a pleasure to thank the staff of Palomar Observatory for their assistance with the observations. The HIRIS project at JPL made the detector available; Richard Lucinio (Caltech) was helpful in preparing the camera for use. We thank John Trauger (JPL) for the use of the WF/PC II computing facilities and his [S II] filter. Deborah Padgett and Jim McCarthy provided valuable assistance to the optical observing and data reduction; Brian Gordon and Dwight Moody (JPL) assisted in the production of the images; and Jorden Woods integrated and improved the data reduction software. We acknowledge helpful discussions with John Carr, James R. Graham, Dave Hollenbach, John Raymond, and Dave van Buren. Thanks are also due to Pat Hartigan, who as referee provided comments that helped improve the discussion sections. The camera construction was supported by a grant from the Caltech President's Fund, with continuing funding from NASA grant RTOP 100-44-24-10. NZS acknowledges support from NSF grant AST 87-14405, and KRS acknowledges the support of a NASA fellowship.

REFERENCES

Beichman, C. A., Hester, J. J., and Gautier, T. N. 1991 in preparation.

Black, J. H. and Dalgarno, A. 1976, *Ap.J.*, **203**, 132.

Black, J. H. and van Dishoeck, E. F. 1987, *Ap.J.*, **322**, 412.

Burhke, T., Mundt, R. and Ray, T. P. 1988, *Astr.Astrophys*, **200**, 99.

Burton, M. G., Brand, P., Geballe, T. R., and Webster, A. S. 1988, *MNRAS*, **236**, 409.

Cohen, M. and Schwartz, R. D. 1983, *Ap.J.*, **265**, 877.

Cohen, M. and Jones, B. F. 1987, *Ap.J.*, **321**, 846.

Delbouille, L. *et al.* "Photometic Atlas of the Solar Spectrum from 1850 to 10000 cm^{-1}" 1981.

Edwards, S. and Snell, R. L. 1983, *Ap.J.*, **270**, 605.

Elias, J. H., Frogel, J. A., Matthews, K., and Neugebauer, G. 1982, *Astron.J.*, **87**, 1029.

Garden, R. P., Russell, A. P. G., and Burton, M. G. 1990, *Ap.J.*, **354**, 232.

Graham, J. R., Wright, G. S., and Longmore, A. J. 1987, *Ap.J.*, **313**, 847.

Hartigan, P. 1989, *Ap.J.*, **339**, 987.

Hartigan, P., Curiel, S. and Raymond, J. 1989, *Ap.J.*, **347**, L31.

Hartigan, P., Raymond, J., and Hartmann, L. 1987, *Ap.J.*, **316**, 323.

Herbig, G. H. and Terndrup, D. M. 1986, *Ap.J.*, **307**, 609.

Herbig, G. H. and Jones, B. F. 1983, *A.J.*, **88(7)**, 1040.

Hollenbach, D. and McKee, C. F. 1989, *Ap.J.*, **342**, 306.

Lane, A.P.: 1989, in *Low Mass Star Formation and Pre-Main Sequence Objects*, ESO Conference Proceedings No. 33, ed. Bo Reipurth.

Lizano, S., Heiles, J., Rodriguez, L., Koo, B., Shu, F. H., Hasegawa, T., Hayashi, S., and Mirabel, I.F. 1988, *Ap.J.*, **328**, 763.

Mundt, R. 1986, *CanadianJ.Phys.*, **64**, 407.

Mundt, R., Brugel, E. W., and Buhrke, T. 1987, *Ap.J.*, **319**, 275.

Myers, P. C., Fuller, G. A., Mathieu, R. D., Beichman, C. A., Benson, P. J., Schild, R. E., and Emerson, J. P. 1987, *Ap.J.*, **319**, 340.

Norman, C. A., and Silk, J. 1979, *Ap.J.*, **228**, 197.

Raga, A. C., and Bohm, K. H. 1985, *Ap.J.Suppl.*, **58**, 201.

Raymond, J. C., Hester, J. J., Cox, D. P., Blair, W. P., Fesen, R. A., and Gull, T. R. 1988, *Ap.J.*, **324**, 869.

Reipurth, B., Bally, J., Graham, J. A., Lane, A. P., and Zealey, W. J. 1986, *Astron.Astrophys.*, **164**, 51.

Rudolph, A., and Welch, W. J. 1988, *Ap.J.*, **326**, L31.

Schwartz, R. D. 1983, *Ann.Rev.Astr.Astrophys.*, **21**, 209.

Schwartz, R. D. 1978, *Ap.J.*, **223**, 884.

Schwartz, R. D., Williams, P. M., Cohen, M., and Jennings, D. G. 1988, *Ap.J.*, **334**, L99.

Schwartz, R. D., Cohen, M., Williams, P. M. 1987, *Ap.J.*, **322**, 403.

Snell, R. L. and Edwards, S. 1981, *Ap.J.*, **251**, 103.

Solf, J. and Bohm, K. H. 1987, *Astron.J.*, **93**, 1172.

Stapelfeldt, K. R. 1991 (in preparation).

Stapelfeldt, K. R., Trauger, J. T., and Scoville, N. Z. 1991 (chapter III).

Strom, K. M., Strom, S. E., and Stocke, J. 1983, *Ap.J.*, **271**, L23.

Strom, K. M., Strom, S. E., Wolff, S. C., Morgan, J., and Wenz, M. 1986, *Ap.J.Suppl.*, **62**, 39.

Strom, S. E., Vrba, F. J., and Strom, K. M. 1976, *A.J.*, **81**, 314.

Turner, J., Kirby-Docken, K., and Dalgarno, A. 1977, *Ap.J.*, **35**, 281.

Zinnecker, H., Mundt, R., Geballe, T. R., and Zealey, W. J. 1989, *Ap.J.*, **342**, 337.

TABLE 1

HH Object Fluxes and Peak Intensities

Object	Aperture Size arcsec^2	[Fe II] 1.644μm	H_2 1-0S(1) 2.122μm	H_2 2-1S(1) 2.248μm	H_2 1-0Q(3) 2.424μm
HH 7	134	10.3 (0.5)	66.6 (3.0)	5.9 (1.5)	65. (17.)
		0.9 (0.1)	5.6 (0.2)	1.1 (0.2)	5.3 (0.1)
HH 8	39	3.4 (0.3)	12.5 (0.8)	1.1 (0.3)	12.6 (3.3)
		0.6 (0.1)	3.0 (0.2)	0.4 (0.2)	2.7 (0.1)
HH 8b	6	0.3 (0.1)	1.1 (0.2)	< 0.5	1.3 (0.4)
		0.3 (0.1)	0.9 (0.2)	< 0.5	0.9 (0.1)
HH 9	4	0.3 (0.1)	0.5 (0.1)	< 0.6	0.4 (0.1)
		0.4 (0.1)	0.7 (0.2)	< 0.5	0.4 (0.1)
HH 10	81	5.2 (0.4)	22.9 (1.4)	1.5 (0.9)	25.5 (6.8)
		0.6 (0.1)	2.4 (0.2)	0.3 (0.2)	2.5 (0.1)
HH 11	18	2.8 (0.2)	1.8 (0.4)	< 0.6	1.9 (0.5)
		1.3 (0.1)	0.6 (0.2)	< 0.5	0.8 (0.1)
HH 11b	18	< 0.5	4.0 (0.4)	< 0.6	4.4 (1.2)
		< 0.3	1.1 (0.2)	< 0.5	1.3 (0.1)
HH 12B	18	5.7 (0.2)	3.6 (0.2)	< 0.4	4.0 (1.3)
		3.3 (0.2)	4.5 (0.1)	< 0.5	2.2 (0.2)
HH 12C	15	3.7 (0.2)	2.2 (0.2)	< 0.5	2.2 (0.7)
		1.0 (0.2)	0.8 (0.1)	< 0.5	0.6 (0.2)
HH 12Cn	15	0.5 (0.1)	2.7 (0.2)	< 0.4	2.2 (0.7)
		0.3 (0.2)	1.6 (0.1)	< 0.5	1.0 (0.2)
HH 12Cw	3	0.6 (0.1)	< 0.3	< 0.3	< 0.2
		0.9 (0.2)	< 0.3	< 0.5	< 0.5
HH 12Di	29	6.5 (0.2)	< 0.6	< 0.5	< 0.3
		1.4 (0.2)	< 0.3	< 0.5	< 0.5
HH 12Dm	13	1.5 (0.1)	2.9 (0.2)	< 0.3	2.6 (0.6)
		0.9 (0.2)	2.3 (0.1)	< 0.5	1.3 (0.2)
HH 12E	19	1.0 (0.1)	11.2 (0.5)	0.5 (0.1)	6.1 (1.9)
		0.8 (0.2)	6.6 (0.1)	0.4 (0.2)	2.9 (0.2)
HH 12F	23	6.5 (0.2)	< 0.5	< 0.4	< 0.4
		2.3 (0.2)	< 0.3	< 0.5	< 0.5
HH 12G	12	0.9 (0.1)	1.9 (0.2)	< 0.3	1.3 (0.4)
		0.6 (0.2)	1.1 (0.1)	< 0.5	0.7 (0.2)
HH 12H	15	< 0.3	2.1 (0.2)	< 0.3	1.6 (0.5)
		< 0.5	1.2 (0.1)	< 0.5	0.8 (0.2)

TABLE 1, continued

HH Object Fluxes and Peak Intensities

Object	Aperture Size arcsec^2	[Fe II] 1.644μm	H_2 1-0S(1) 2.122μm	H_2 2-1S(1) 2.248μm	H_2 1-0Q(3) 2.424μm
HH 34 jet	23	4.0 (0.2) 1.1 (0.1)	< 0.3 < 0.6	—	< 0.3 < 0.4
HH 34 S	43	2.9 (0.2) 0.4 (0.1)	< 0.7 < 0.7	—	< 0.4 < 0.4
HH 34 N	43	< 0.4 < 0.6	< 0.5 < 0.6	—	< 0.8 < 0.4

Notes to Table 1

1) The apertures employed are outlined in Figures 1f, 4f, and 5f.

2) Flux units are 10^{-14} ergs s^{-1} cm^{-2}.

3) Intensity units are 10^{-4} ergs s^{-1} cm^{-2} sr^{-1}.

4) Uncertainties given in parentheses; — indicates no data taken.

5) The Q(3) values quoted here are corrected for Q(1) contamination.

FIGURE CAPTIONS

Figure 1. Images of HH 7-11. Panels *a* – *d* are infrared images, panel *e* is the optical image, and panel *f* identifies the objects whose photometry is given in Table 1. Tick marks are given in ten pixel (7.65″) increments. The field of view is 98 arcseconds square.

Figure 2. An overlay of two contour plots of the emission from HH 7-11. The dark contours represent H_2 Q(3) emission; the light contours represent the 6717 Å [S II] emission. The contour interval is a factor of $\sqrt{2}$. The solid line through the head of HH 7 shows the path of the slit used to make the intensity plots in Figure 3.

Figure 3. Intensity plots across the head of HH 7. 3*a*, 3*b*, and 3*c* are plots of intensity versus position along a slit crossing the head of HH 7; the position and orientation of the slit is shown by the line in Figure 2. The slit width is 4″. The solid lines in 3*a*, 3*b*, and 3*c* represent the data; the dotted lines represent the best gaussian least-squares fit to the data. Note the substantial difference in FWHM between the H2 profile of 3*a* and the [S II], [Fe II] profiles of 3*b*, 3*c*.

Figure 4. Schematic drawings of two possible types of HH objects: *(a)* the bow shock structure associated with the termination of the jet; and *(b)* the shock structure around a small clump of material being acted on by the jet.

Figure 5. Images of HH 12. Panels *a* – *d* are infrared images, panel *e* is the optical image, and panel *f* identifies the objects discussed in the text. Tick marks are given in ten pixel (7.65″) increments. The field of view is 98 arcseconds square.

Figure 6. An overlay of two contour plots of the emission from HH 12. The dark contours represent H_2 Q(3) emission; the light contours represent the 6717 Å [S II] emission. The contour interval is a factor of $\sqrt{2}$.

Figure 7. Images of the HH 34 jet field. Panels $a - d$ are infrared images, panel e is the optical image, and panel f indentifies the objects discussed in the text. Tick marks are given in ten pixel (7.65″) increments. The field of view is 98 arcseconds square.

Figure 8. Comparison of the [Fe II] 1.64 μm and [S II] 6717+6731 Å emission structure in the HH 34 jet. A swath 6″ wide was used to bin the infrared data. Continuum subtraction was performed for the [Fe II] curve. The [S II] tracing is taken from Figure 4 of Buhrke *et al.* (1988).

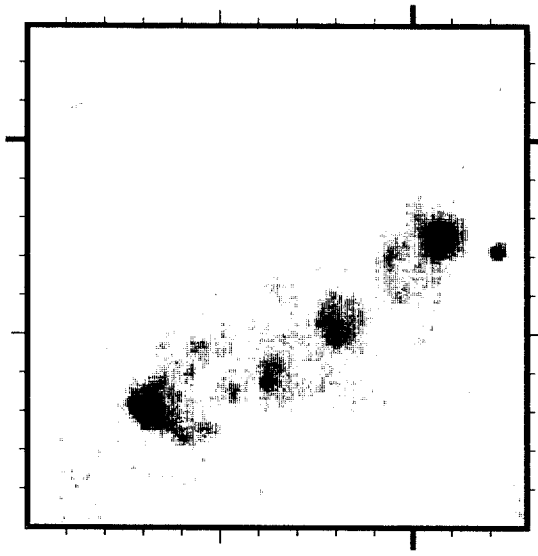

Figure 1A
H2 Q(3) 2.42 microns

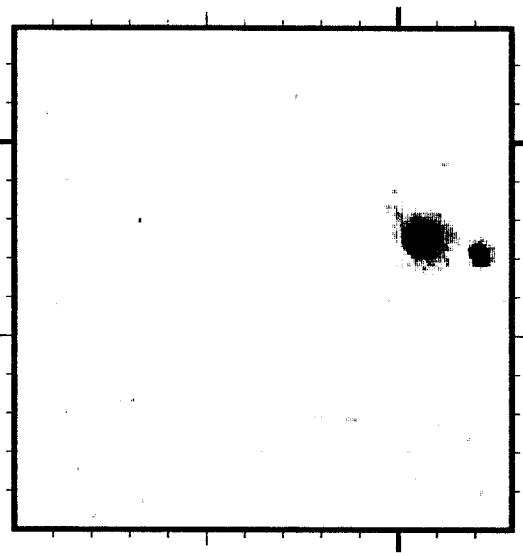

Figure 1B
2.19 continuum 1% BW

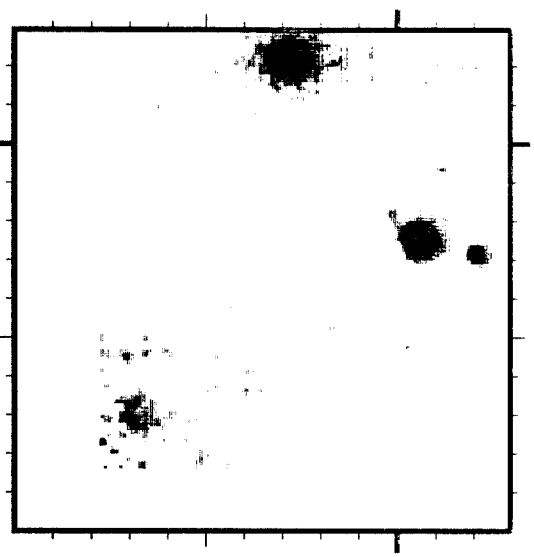

Figure 1C
H2 2-1S(1) 2.24 mu

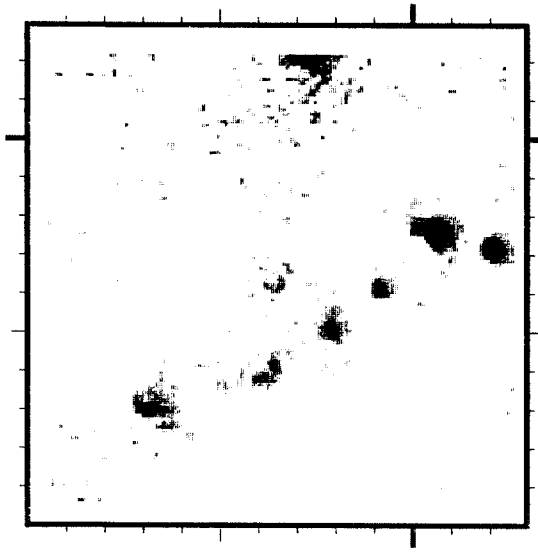

Figure 1D
[Fe II] 1.64 microns

Figure 1E
[S II] 6717 Angs

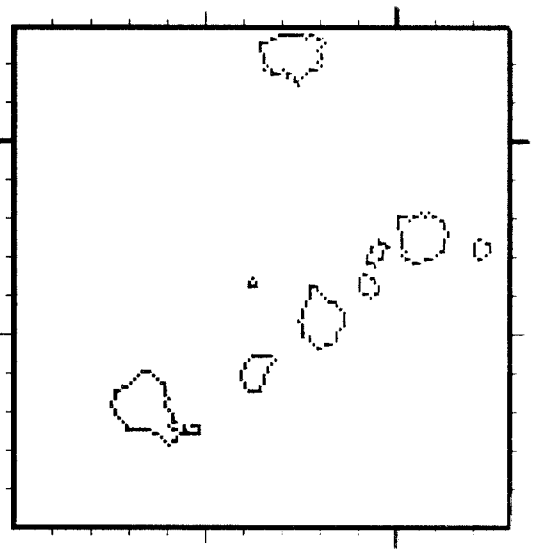

HH 7-11
Object IDs

Figure 1f
Chapter II

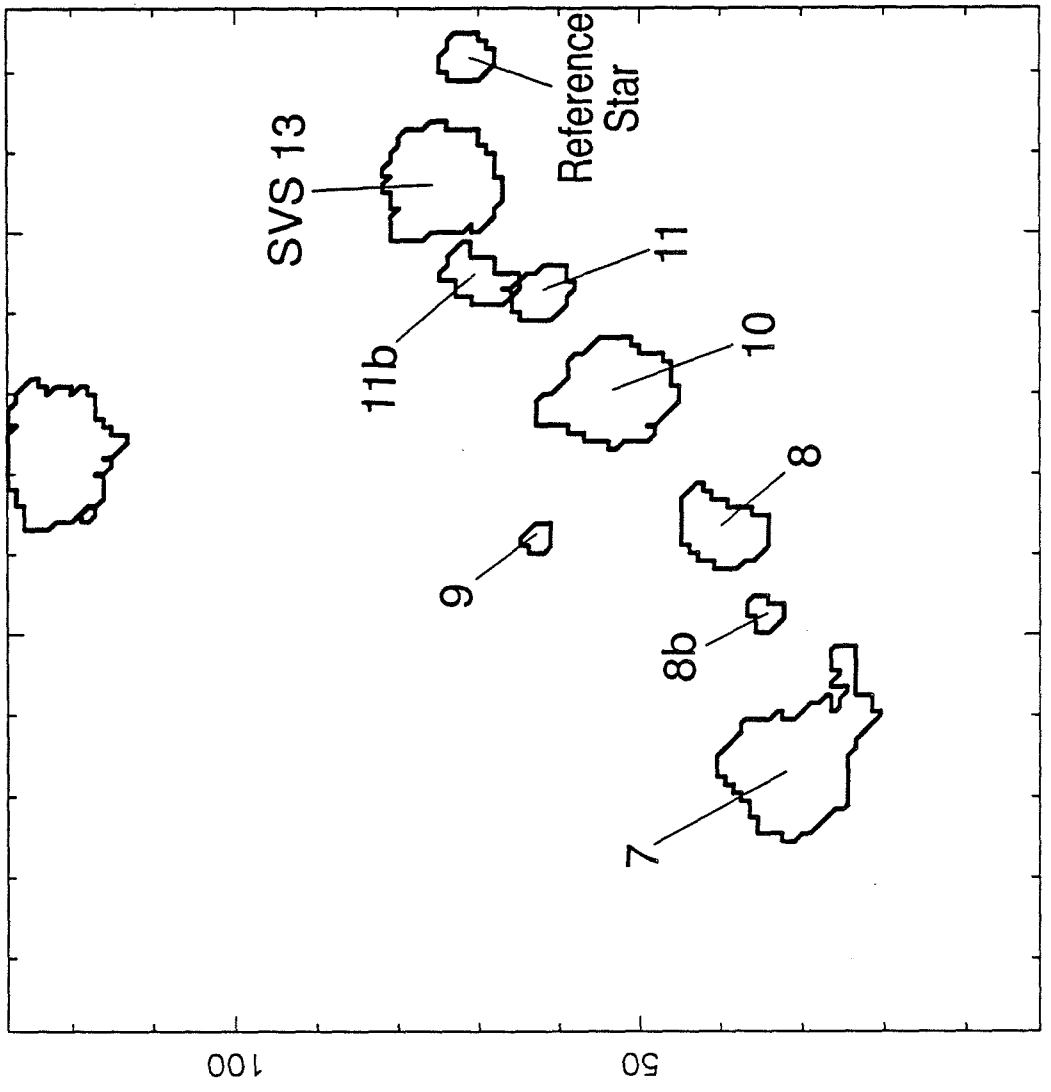

HH 7-11 Object Identifications

Figure 2

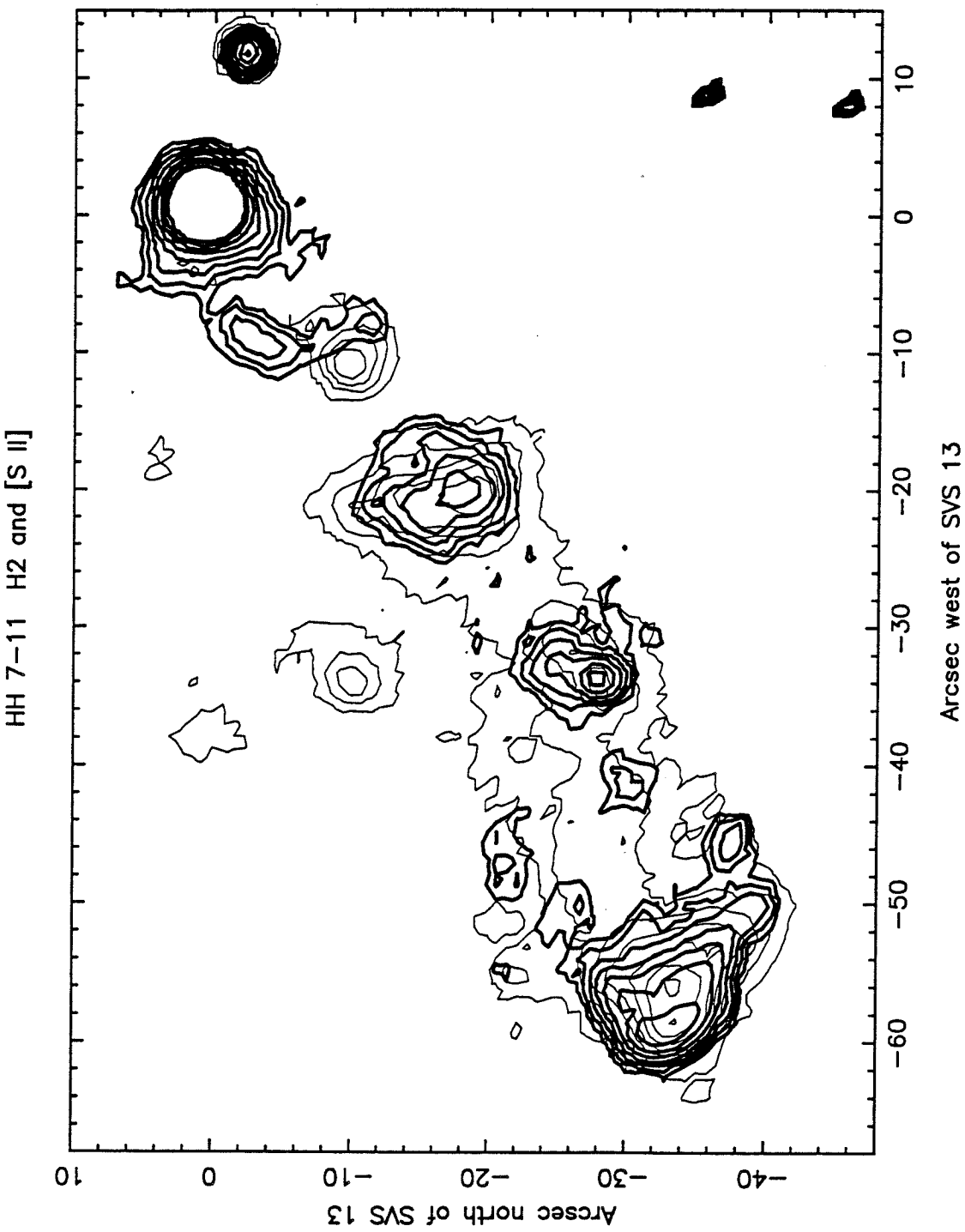
HH 7–11 H2 and [S II]
Arcsec north of SVS 13
10
0
−10
−20
−30
−40
Arcsec west of SVS 13
10
0
−10
−20
−30
−40
−50
−60

Figure 3

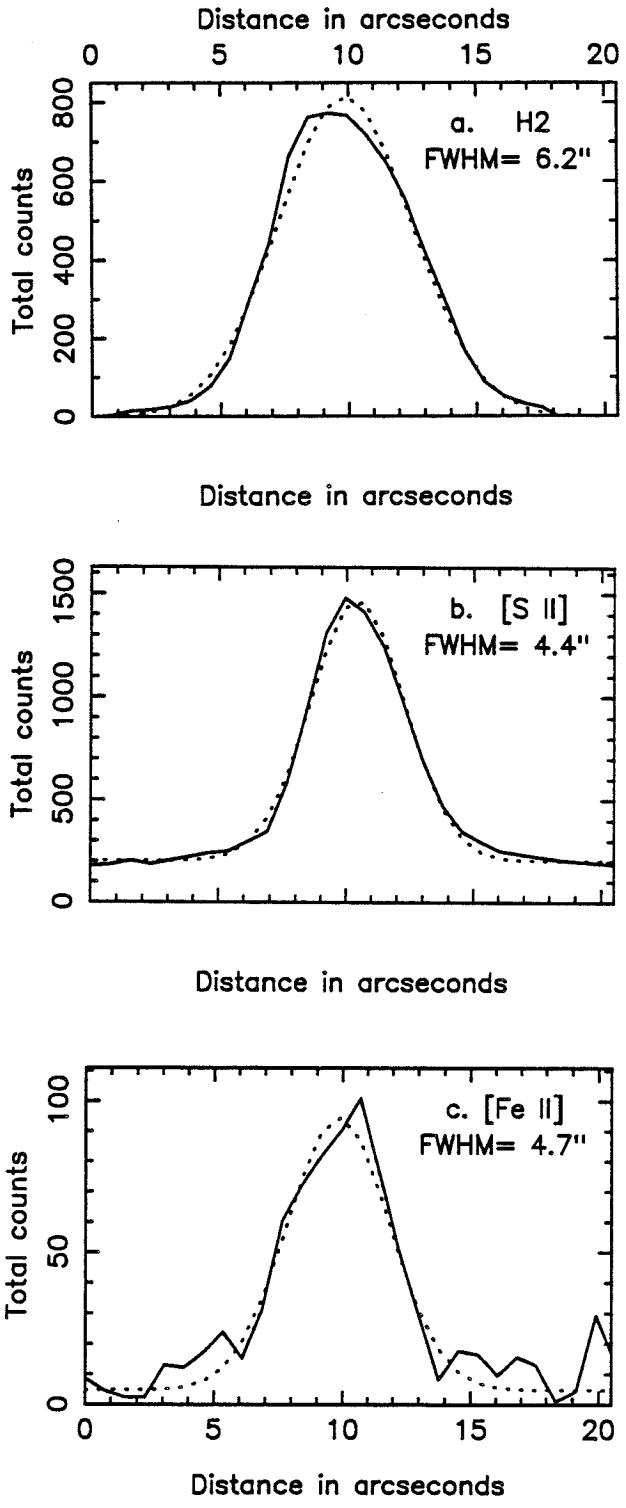
Distance in arcseconds
0
5
10
15
20
Total counts
0
200
400
600
800
a. H2
FWHM= 6.2"
Distance in arcseconds
Total counts
0
500
1000
1500
b. [S II]
FWHM= 4.4"
Distance in arcseconds
Total counts
0
50
100
c. [Fe II]
FWHM= 4.7"
0
5
10
15
20
Distance in arcseconds

Figure 4

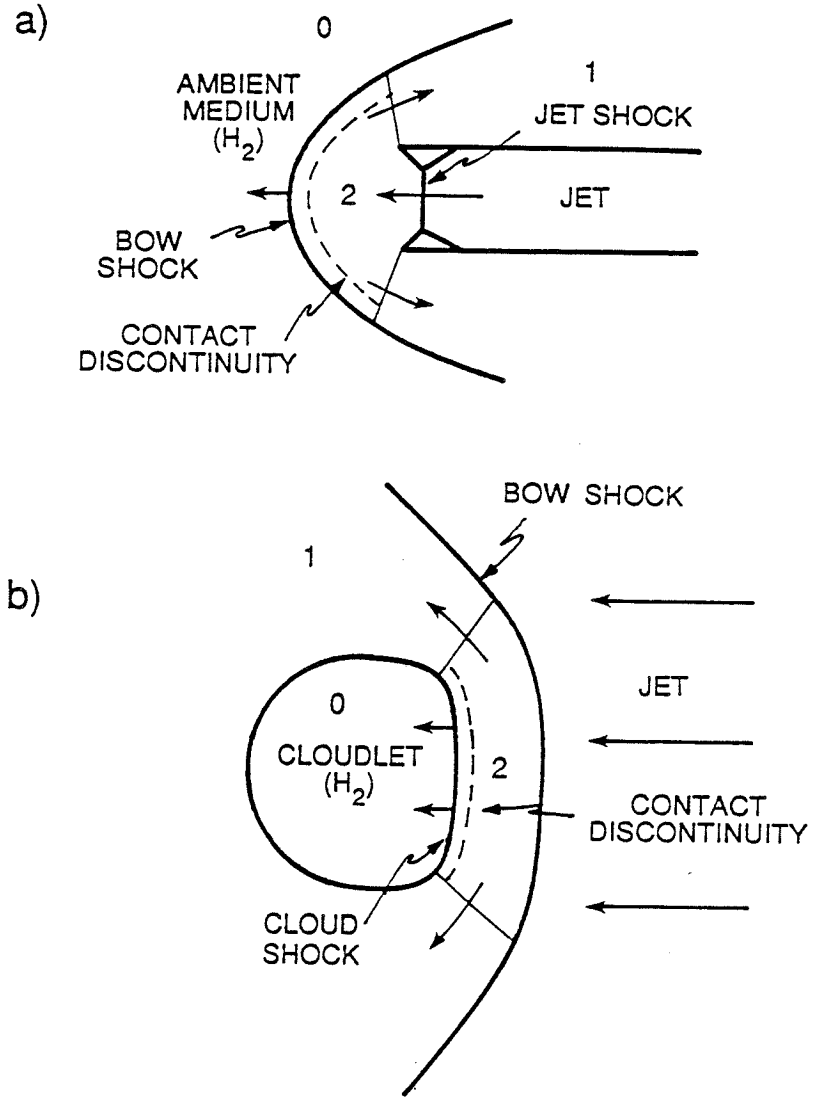
a)
0
AMBIENT MEDIUM (H_2)
1
JET SHOCK
2
JET
BOW SHOCK
CONTACT DISCONTINUITY
b)
BOW SHOCK
1
JET
0
CLOUDLET (H_2)
2
CONTACT DISCONTINUITY
CLOUD SHOCK

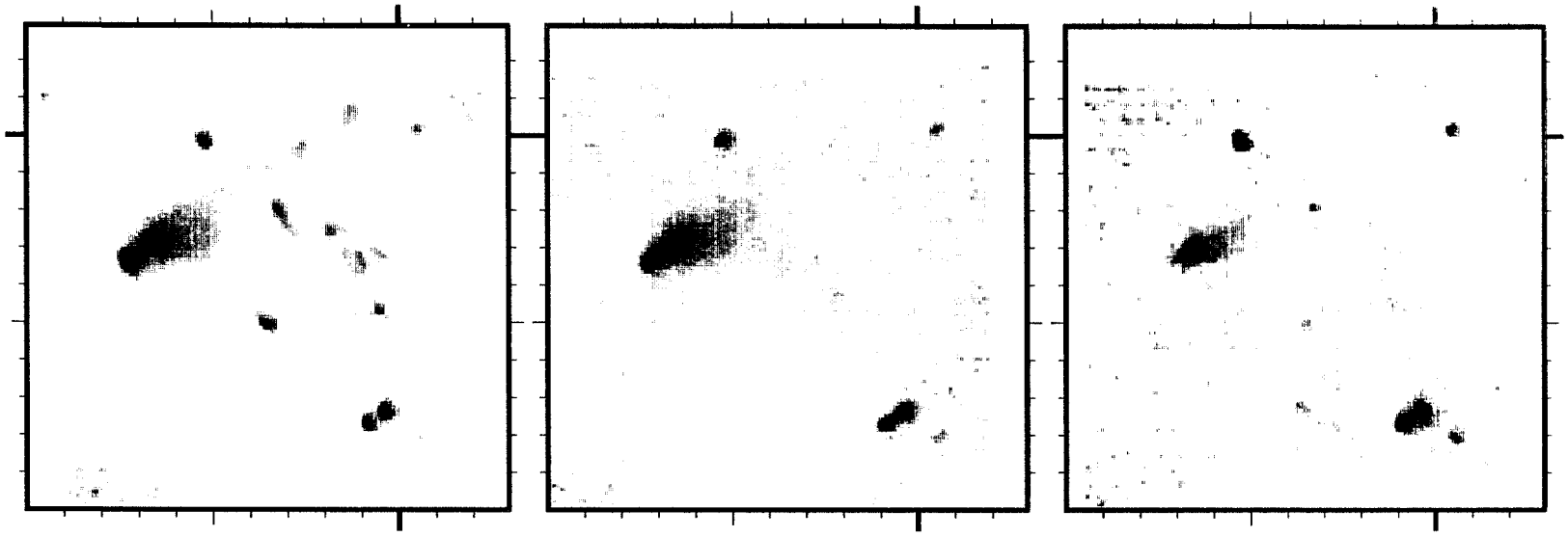

Figure 5A
H2 Q(3) 2.42 microns

Figure 5B
2.19 continuum 1% BW

Figure 5C
Wide-band 'J' filter

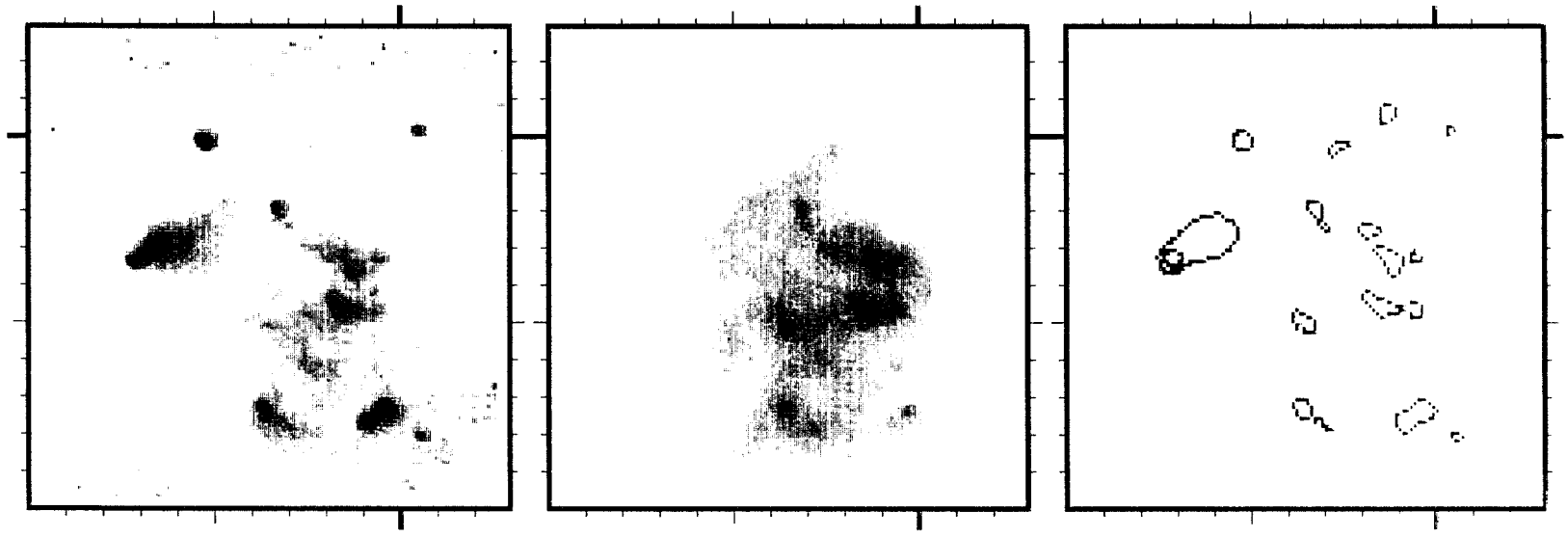

Figure 5D
[Fe II] 1 64 microns

Figure 5E
[S II] 6717 Angs

HH 12
Object 1D s

Figure 5f.

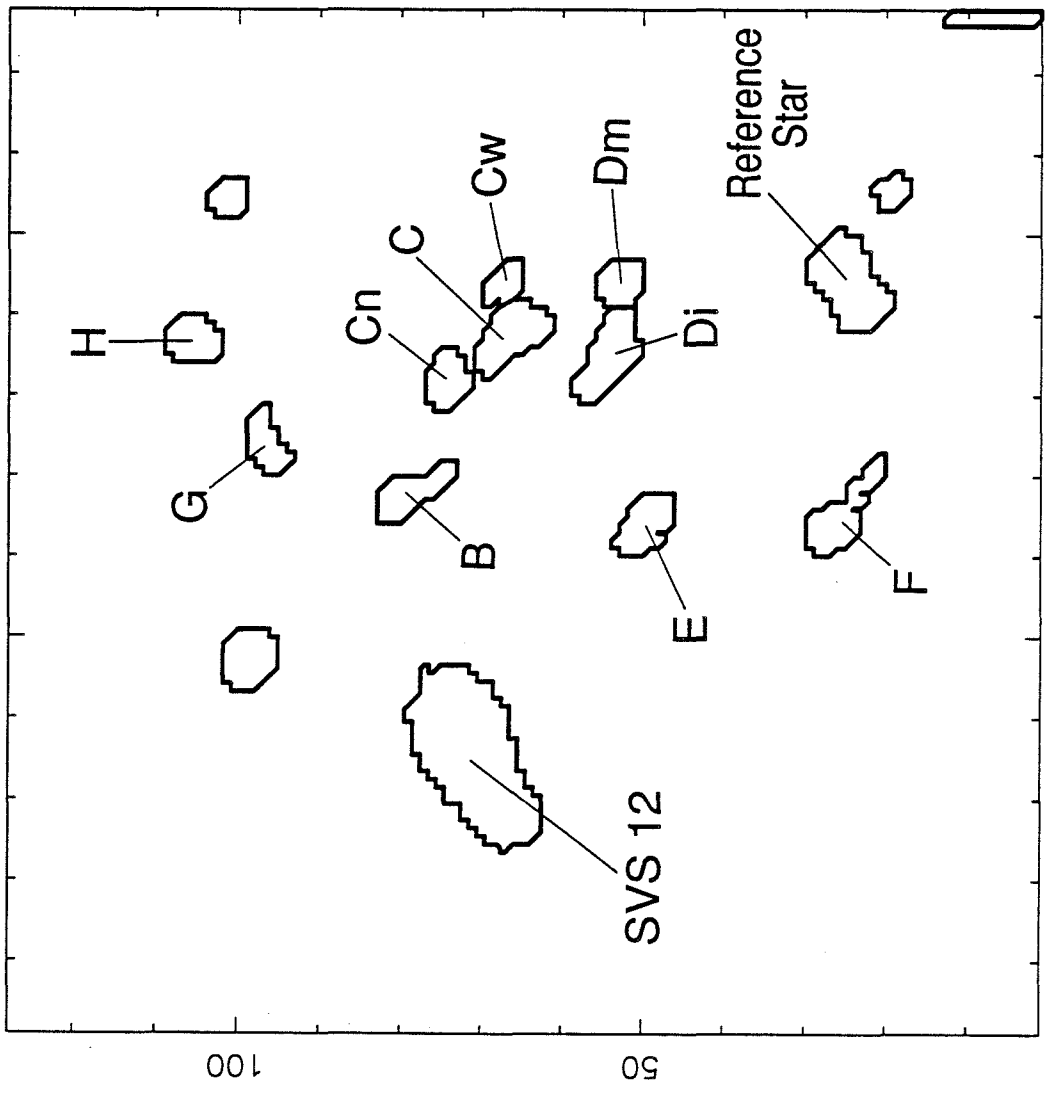

HH 12 Object Identifications

Figure 6

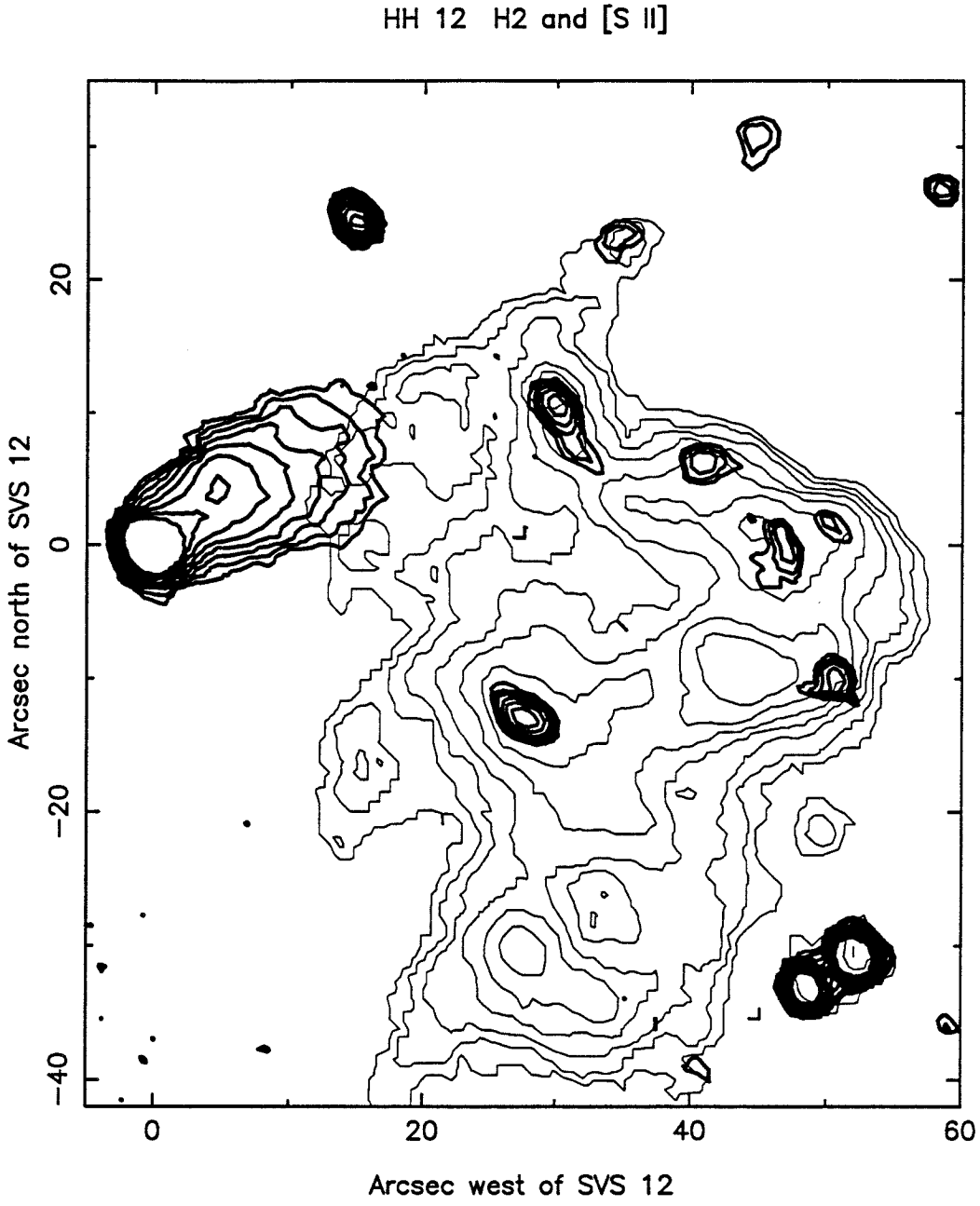
HH 12 H2 and [S II]
Arcsec north of SVS 12
20
0
−20
−40
0
20
40
60
Arcsec west of SVS 12

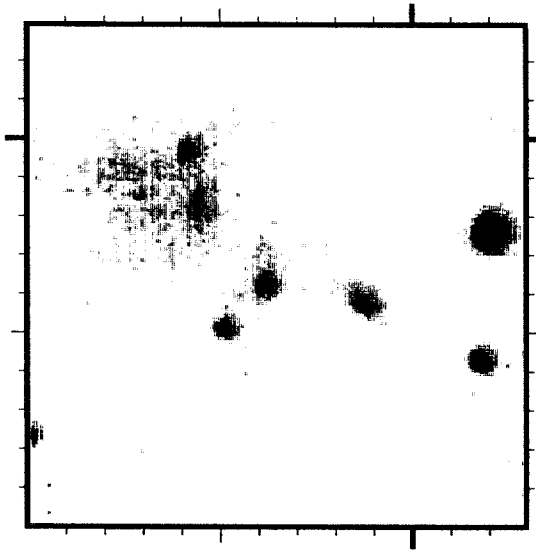

Figure 7A
Wide-band 'J' filter

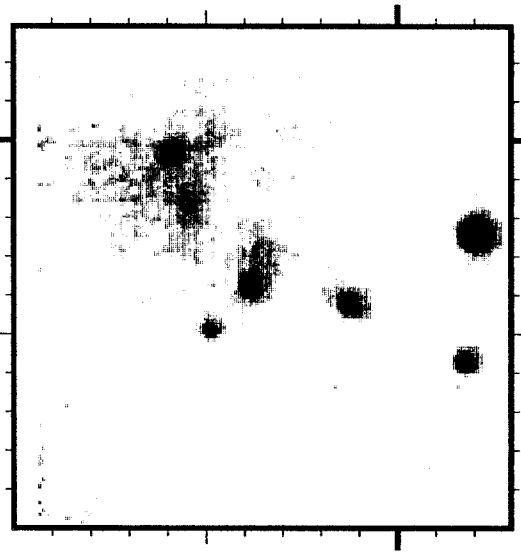

Figure 7B
Wide-band 'H' filter

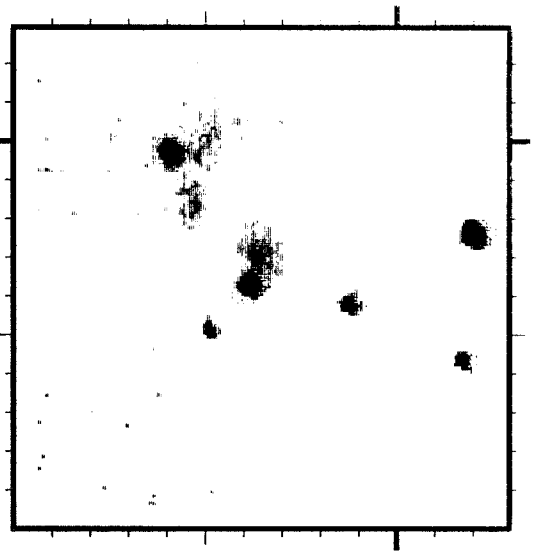

Figure 7C
Wide-band 'K' filter

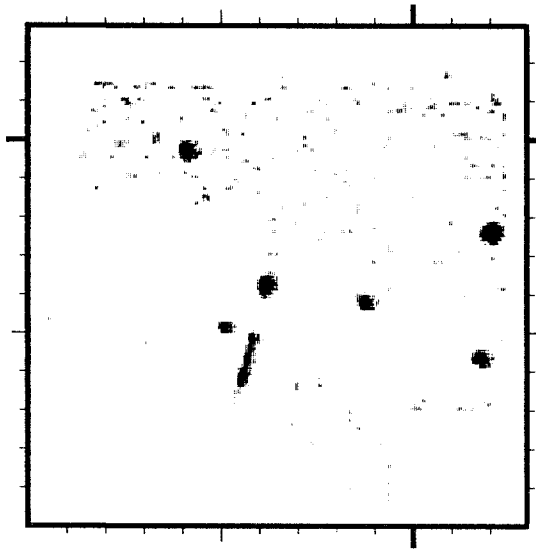

Figure 7D
[Fe II] 1.64 microns

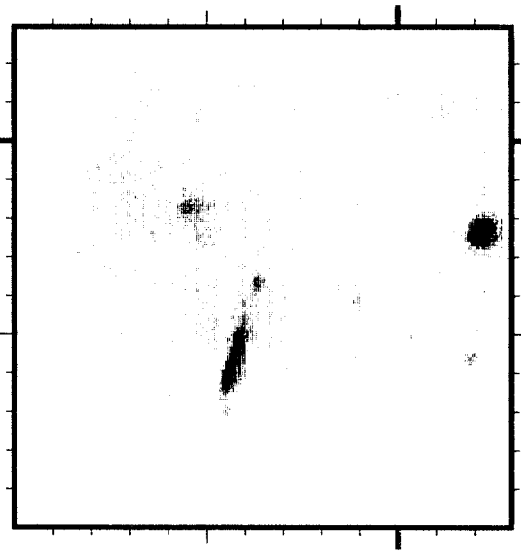

Figure 7E
[S II] 6717 Angs

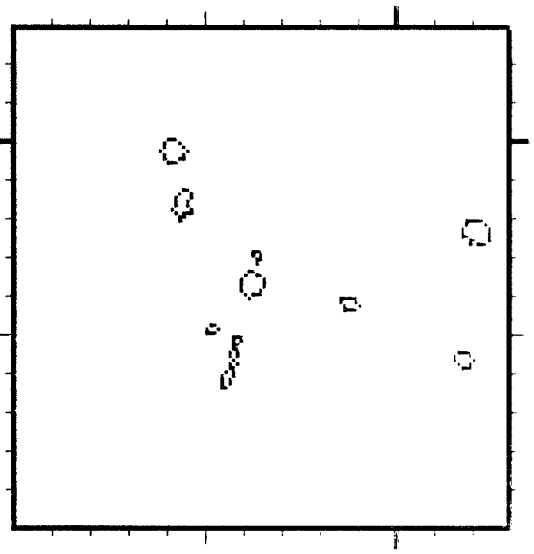

HH 34
Object ID s

Figure 7f.

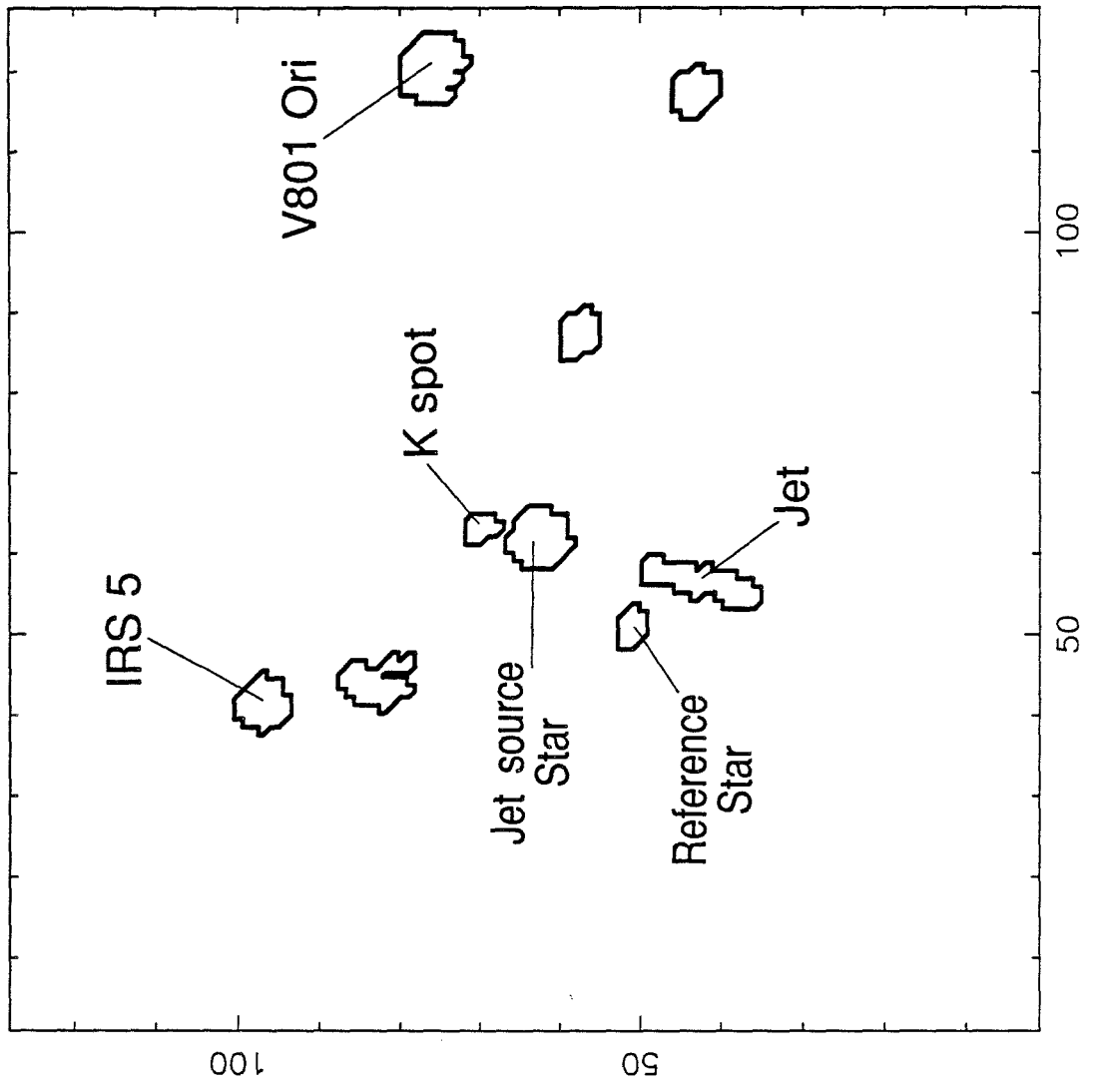
V801 Ori
K spot
IRS 5
Jet source Star
Reference Star
Jet
100
50
100
50

Figure 8
Chapter II

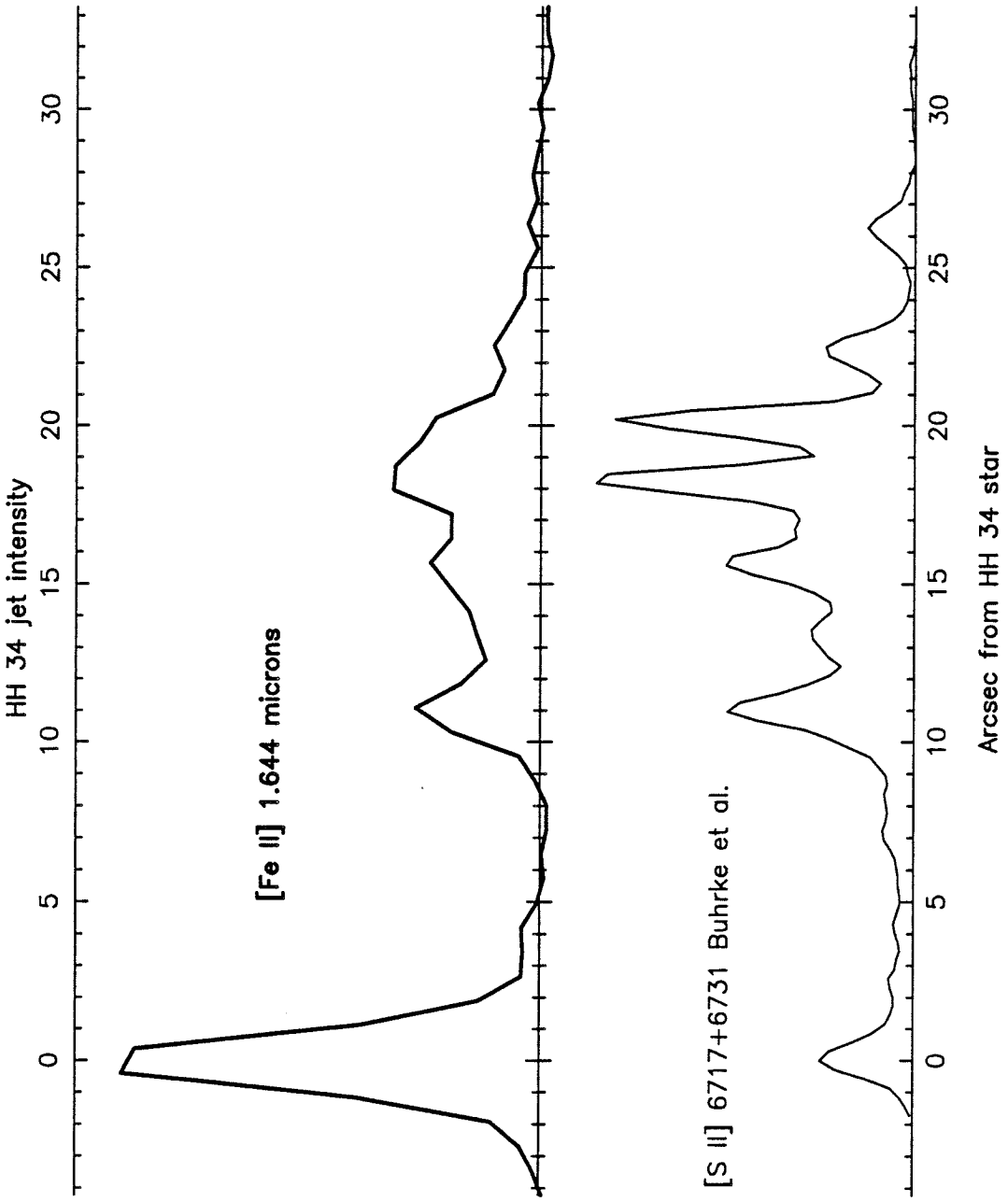

Chapter III.

The Velocity Structure of Three Herbig-Haro Objects Studied with Fabry-Perot Imaging Spectroscopy

Abstract:

The radial velocity structure of HH 1, HH 7-11, and HH 12 has been observed in the 6731 Å [S II] emission line using a Fabry-Perot imaging spectrometer. The resulting data cubes are the most spatially complete maps yet obtained of the kinematic structure of these Herbig-Haro objects. We find clear kinematic evidence of spatially isolated, high velocity peak within HH 7 which has the properties expected for the terminal shock of a jet at its working surface. At the northern tip of HH 1, we find a small region of double peaked [S II] emission which has not previously been identified. In HH 12 we find a fairly smooth radial velocity structure with velocity gradients aligned toward SVS 12, suggesting that despite the proper motions SVS 12 is the exciting star for HH 12. The results illustrate the value of spatially complete line profile information to the study of HH objects.

I. Introduction

The field of Herbig-Haro (HH) object research has grown rapidly over the past fifteen years, and as a result these objects are better understood today than at any time since their discovery by Herbig and Haro in the early 1950's. The conceptual key to our understanding of these small emission nebulae was provided by Schwartz (1975), who proposed that they are energized by the action of high velocity shocks. Based on their proper motions, association with molecular outflows, and proximity to young stellar objects it is now clear that the HH object shocks are formed by the action of an outflowing stellar wind on nearby ambient material (Schwartz 1983). More than 100 HH objects have been cataloged (Von Hippel, Bell-Burnell, and Williams 1988), and new ones continue to be discovered (Reipurth 1989).

Much of HH object research has dealt with the question of shock geometry. The large linewidths observed in many objects clearly rule out formation in a single planar shock. A curved shock surface can produce the range of velocities observed in the emission line profiles without requiring any ad-hoc internal motions. As a result, much effort has gone into modelling the expected optical emission line profiles from axisymmetric bowshocks (Raga and Bohm 1985; Hartigan, Raymond, and Hartmann 1987). These bowshocks are expected to form in the jet working surface model, an "interstellar bullet" stellar mass ejection model, and in a shocked cloudlet model. The specifics of the bowshock dependent on the nature of the obstacle. Although several spatially resolved HH objects morphologically resemble bowshocks, many others do not (Strom *et al.* 1986). Some objects appear to be collimated jets (Mundt, Brugel, and Buhrke 1987). Many objects have an irregular

appearance which makes their shock geometries difficult to interpret.

For any HH object, detailed information on the velocity structure of the emitting regions is needed to constrain the shock geometry. To obtain this information, several workers have employed long-slit spectroscopy to map the velocity fields: Raga and Bohm 1985 (HH 1 and 2); Solf and Bohm 1987 (HH 7-11); Solf 1987 (HH 24); Burhke, Mundt, and Ray 1988 (HH 34); Reipurth 1989 (HH 111); and Hartigan, Raymond, and Meaburn 1990 (HH 47). Many of these HH objects extend over regions on order of 1′ in size; to map their velocity structure, spectra must be taken at several slit positions. A drawback of the long-slit observing technique is that velocity data can only be obtained for regions where a slit was placed; for the more extended HH objects, it is usually not possible to observe every point of interest. In addition, there is usually some uncertainty as to the exact location of the spectrograph slit with respect to the HH object.

We must turn to imaging spectroscopy in order to produce spatially complete velocity maps of HH objects. A first attempt at this was made by Strom *et al.* (1986) using a narrow tiltable interference filter, but the velocity resolution of 250 km s^{-1} was too coarse to provide useful information about shock structure. The ideal instrument for high resolution mapping of the velocity structure of an emission nebula is the Fabry-Perot imaging spectrometer. This instrument allows the line profile of a single emission line to be measured over a wide area of sky, with a spectral resolution R≈10,000 (30 km s^{-1}). Fabry-Perot data can be rendered in the usual way as line profiles and position-velocity diagrams; in addition, monochromatic images in a very narrow bandpass can be synthesized. In comparison with long-slit methods, the Fabry-Perot offers complete areal coverage of extended objects; no uncertainty about the position of a spectrum; and improved ability isolate spectral

components that are localized to small regions. With the formidable Fabry-Perot data reduction task now made practical by modern computers, this instrument has gained wide acceptance in the past five years (Bland and Tully 1989).

The objects we selected for study were HH 1, HH 7-11, and HH 12. HH 1 is a well-studied, bright, compact object which allows a comparison of our observing methods and earlier work. The Fabry-Perot spectroscopy technique is used to greatest advantage in the study of spatially extended objects; for this reason we also chose to study HH 7-11 and HH 12, two objects 0.5′ x 1′ in size. Much of HH 7-11 has been observed by Solf and Bohm (1987) using slit spectroscopy. Kinematical study of HH 12 has been only fragmentary prior to this work, perhaps because of the large number of slits which would be needed to cover the entire object. We chose to map these three objects in the 6731 Å line of [S II], a line which is strong in low excitation HH objects (such as HH 7-11 and HH 12) and which models predict is produced in both shocked atomic and molecular media (Hartigan, Raymond, and Hartmann 1987; Hollenbach and McKee 1989).

II. Observations and Data Reduction

The imaging spectroscopy discussed in this paper was carried out at the Prime focus of the 5 meter Hale telescope on the nights of 5-8 January 1988. The instrument (see Figure 1) consisted of a CCD detector, a pressure-scanned Fabry-Perot etalon in the collimated beam, a blocking filter to isolate a single Fabry-Perot order, and collimating and focussing lenses. This optical configuration is a straightforward extension of the Palomar PFUEI instrument developed by Gunn. We used an 800 x 800 Texas Instruments CCD known as "Mark V" which was provided by the WF/PC project. With these camera optics, the detector has a 5′ field of view

with 0.44″ pixels. A narrowband filter centered near the 6731 Å line of [S II], with FWHM of 10 Å, was placed in the collimated beam to isolate a single interference order. The etalon consisted of two 100 mm diameter fused silica plates separated by three identical fixed spacers approximately 150 microns in thickness; this assembly was held in compression by three spring clamps to ensure mechanical stability of the etalon gap at different zenith angles. An airtight pressure vessel with two optical windows held the etalon in a dry nitrogen environent at the ambient temperature. The etalon's multilayer optical coating (Trauger 1976) has a reflectivity of 92% and an effective finesse of 25. For observations at 6731 Å this system operated with a free spectral range of 15.9 Å, and thus an effective spectral resolution of 0.6 Å or 28 km s^{-1}.

Two preliminary calibrations were necessary to prepare the imaging spectrometer for use. First, with the etalon removed, the proper tilt for the blocking filter was determined by observation of the planetary nebula NGC 2392. This object was chosen because it is a bright source with a radial velocity $V_{Hel} = +84$ km s^{-1} (Perek and Kohoutek 1967) close to those of the HH objects to be studied. The radial component of a planetary nebula's expansion velocity is zero at its edges; by maximizing the counts on the limb-brightened edges of the nebula as a function of filter tilt, the tilt angle corresponding to maximum instrumental [S II] throughput was determined. Secondly, with the etalon in the optical path and NGC 2392 on the optical axis, the N_2 pressure which gave maximum edge counts was determined. This datum gives an indication of what pressure value corresponds to the nebula's known radial velocity, and thus serves as a secondary wavelength calibration.

The etalon N_2 pressure was adjustable to within 1 torr by an observer at the Prime focus. A sequence of pressure-scanned Fabry-Perot frames was acquired

for each object using the following guidelines: (1) The object was first aquired at pressure setting near the middle of the scan range, usually about 2000 torr. (2) Subsequent frames were aquired at pressure intervals of 180 torr; this corresponded to one sample per spectral resolution element. (3) A full scan across the Fabry-Perot's entire free spectral range was *not* performed if it was observed that the target's velocity range had been completely covered by a partial scan; this was the case for HH 1 and HH 12. (4) A second scan to oversample the instrumental profile by a factor of 2 was performed after the first scan was completed for HH 7-11 and HH 12. The final data set on the HH objects consisted of 14 300 second frames on HH 1; 24 600 second frames on HH 7-11; and 14 500 second frames on HH 12. Dome flats were made through the blocking filter by removing the etalon from the optical path.

Each spectrometer frame is a two dimensional image of the emission on the sky, modulated by the Fabry-Perot interference pattern. This axially symmetric pattern defines the variation of transmitted wavelength with position over the CCD, and is given by the relation (Born and Wolf 1986)

$$m\lambda = 2nl\cos\theta = \frac{2nl}{\sqrt{1 + r^2/f^2}} \tag{1}$$

where m is the order number, λ is the transmitted wavelength, n is the refractive index of the gas between the etalon plates, l is the physical spacing of the etalon gap, θ is the angle from the optical axis, r is the radial distance from the optical axis, and f is the effective focal length of the camera lens. This Fabry-Perot spectral pattern is illustrated by an image of a uniform monochromatic source (Figure 2). The individual rings correspond to separate interference orders, with the lower order

numbers at the larger radii. This entire pattern can be scanned across the detector by varying n, which is a montonic function of the gas pressure. Greater pressures yield larger values of n, thus incrementing the transmitted wavelength at a given position on the CCD detector. For dry nitrogen, n(P) has been experimentally determined by Peck and Khanna (1966), who derive the empirical relation

$$(n-1) = \left(6.497\text{x}10^{-5} + \frac{3.0738\text{x}10^{-2}}{144. - \sigma^2}\right) \frac{288.16}{(\text{T} + 273.16)} \frac{\text{P}}{760} \qquad (2)$$

where σ is the wavenumber in cm^{-1}, T is the centigrade temperature, and P is the pressure in torr. We measured P relative to an evacuated reference plenum, and obtained T from the Hale telescope's resident Prime focus temperature sensor.

In order to use equation (1) to reduce the data, the instrumental parameters f, l, and m must be determined. A set of four calibration frames, each at a different pressure, was acquired by observing the dome flat-field screen illuminated by an Hα lamp. One of these frames is shown in Figure 2. An Hα blocking filter was used in place of the [S II] filter for these observations. Detailed analysis of these four frames yielded the needed instrumental parameters and wavelength calibration. The first step of the data reduction was bias-subtraction and flat fielding of all images following usual CCD data reduction procedures. A great deal of original work was necessary to carry out the remainder of the data reduction, for standard astronomical image processing software does not treat the case of Fabry-Perot imaging spectroscopy. All of the subsequent data analysis was carried out using a number of FORTRAN programs written specifically for this project.

Each of the calibration frames was analyzed to determine the position of the optical axis on the CCD (the ring center) and the radius (in pixels) of each ring.

A program called CONBLOB was used to identify all contiguous pixels with data number values well above background levels. With each ring defined in this way, intensity-weighted positional moments were calculated to find the ring pattern center and each ring's radius. The measured ring radii lead directly to a determination of f; by comparing the ring radius of a specific order observed at two different pressures, the following relation can be derived from equation (1) assuming $r_2 \geq r_1$ and fixed l:

$$f^2 = \frac{r_2^2 - r_1^2(n_2/n_1)^2}{((n_2/n_1)^2 - 1)} \tag{3}$$

This equation was applied to fifteen pairs of same-order, different pressure ring radii to yield a f value of 3806 $\pm$ 65 pixels, or 57.1 $\pm$ 1 mm. This effective focal length value is only slightly different from the specification focal length of our camera lens (58 mm), indicating that the operating configuration of the instrument was quite close to the design configuration.

The etalon physical spacing l can be determined using another relationship derived from equation (1). Considering now the Hα ring pattern within a single calibration frame, and using the fact that a given ring's order number exceeds that of the next exterior ring by *exactly* 1, the physical spacing can be expressed in terms of f and the ring size as

$$l = \frac{\lambda}{2n(\cos\theta_m - \cos\theta_{m-1})} \tag{4}$$

Equation (4) was applied to eight pairs of adjacent-order rings, yielding a measured etalon physical spacing of 142.6 $\pm$ .2 μm. This result allows calculation of the

Fabry-Perot spectrometers' free spectral range (the wavelength separation between orders): $\Delta\lambda = \lambda^2/2l = 15.9\text{Å} = 700$ km s^{-1}.

Once f and l are determined, the order m of any calibration ring can be found from its measured radius using equation (1). The data show that the central Hα ring corresponds to $m = 435$. This is *not* the order number to be used with the HH object spectra, however, because the objects were observed in [S II]. The wavelength difference between Hα and [S II] is equivalent to 10.6 spectral orders, suggesting $m \approx 424$ at [S II]. This estimate was confirmed by [S II] observations of NGC 2392: on the outer edge of this object, the known radial velocity and measured r determined $m = 424 \pm .05$ as the central [S II] order.

An example of how a spectrum can be extracted from a Fabry-Perot frame is shown in Figure 3. To make this plot from the frame shown in Figure 2, a column of pixels extending from the optical axis upward through the first the Hα ring was analyzed. Each pixel position in the column is equivalent to a different sampled wavelength (or velocity) according to equation (1); the intensity in each pixel is therefore the intensity at that corresponding wavelength. This figure shows the instrumental profile at Hα, with a FWHM of 30 km s^{-1}. It also serves as a check on the accuracy of the wavelength calibration, showing that the instrumental parameters determined above yield a measured radial velocity of -4 km s^{-1} for the Hα calibration lamp.

Although three spectrometer orders are present on separate regions of the detector (see Figure 2), only the order corresponding to the central ring was analyzed. This simplification was possible because the typical angular size of the HH objects studied (1′) was less than the angular separation between the central fringe and the

next exterior ring (which was 114″ at 6731 Å in our instrument). We were therefore able to avoid the need to patch together spectra from different orders, which is an added complication to the reduction of Fabry-Perot spectra of more extended objects.

With the analysis of the calibration frames complete, the reduction process began on the HH object spectral images. Two kinds of image 'cleaning' were performed. First, the data from a bad CCD column was replaced by a one-dimensional row-by-row interpolation across that column. Second, all images were smoothed using a 3 x 3 pixel median filter to remove cosmic rays hits. Over the duration of a pressure scan sequence (which was nearly six hours in the case of HH 7-11), reference star positions were observed to shift by as much as ten pixels. The correction of these shifts, by resampling the original images to produce new ones where the reference star lies at the same pixel position in all frames, is known as image registration. There is a special added concern when registering Fabry-Perot frames: keeping track of the position of the optical axis. The axis position on the CCD is the same in all *un*registered images; but since the each registered image has been shifted by a different amount, the optical axis position will be different in each one. The shift of the optical axis *with respect to the object being observed* is exactly equal, and of opposite sign, to the position shift of the reference star between the original object frames. Following this rule a revised optical axis position was calculated and entered into the header of every registered spectral frame. As a final data editing step, registered 192 x 160 pixel subimages were extracted for the next steps of the analysis. The programs HDRCONPT and SUBIM were used to carry out the cleaning, registration, and subimaging steps just discussed.

To check the stability of atmospheric transparency we measured the brightness

of a reference star in each Fabry-Perot frame. For an ideal flat continuous stellar spectrum the star's observed brightness variations can be used to correct for differential airmass effects between frames. We decided not to employ this correction to our data. In the cases of HH 1 and HH 12 the only available reference stars were unsuitable because of a bright stellar [S II] emission line (HH 1), and low signal-to-noise (HH 12). The reference star in the HH 7-11 field was well-behaved, with about 5% rms amplitude variation among the frames and no discernable trend versus airmass.

At this point the spectral subimages comprised a 'data cube' for each HH object. The term 'cube' is indicative of the three axes (two spatial, one spectral) over which the intensity values have been measured: $I(\alpha, \delta, \lambda)$. The data can be rendered as hardcopy results in several different ways. The first and most straightforward rendering is a line profile at a selected position. A line profile is simply a one-dimensional cut through the cube along the wavelength direction: $I(\alpha_0, \delta_0, \lambda)$. For each frame in the cube, λ is calculated using the frame's value of P and the selected position's optical axis distance according to equations (1) and (2). All the line profiles shown in this chapter were produced by binning together data over 3 x 3 pixel regions. This improved the signal to noise of the spectra without degrading spatial resolution in the binned data, which was comparable to the seeing of (1.4″)

Moment analysis and gaussian fitting were carried out for all line profiles where the signal-to-noise was greater than four. Velocity moments were calculated by the program VNUMMAP, and are presented in the results section. Moment maps are a concise way to summarize the spatial variation of the line properties, but they do not convey all the available information about line *shape*. To examine this aspect of the data, line profile plots were produced covering the full spatial extent of all three

objects. Each profile was fit by a multicomponent gaussian, and the functional fit was plotted along with the data points on each spectrum. A two component gaussian model was used to fit the HH 1 and HH 12 data; a third component was allowed, if necessary, in fitting of the HH 7-11 data. The line profile plotting and fitting were performed by a program called FPSPLOT, which produced a total of 881 fitted profiles. For the sake of brevity very few of these will be presented below; however, these 140 pages of plots were an important resource for the location and study of regions with interesting velocity structure.

Another way to present the data cubes is in the form of monochromatic images, or in the terminology of radio interferometry, velocity channel maps. These are two dimensional slices of the data cube, $I(\alpha, \delta, \lambda_0)$; they are very useful for showing how an object's morphology changes with the observed velocity. In the case of HH 7 this means of rendering the data is especially demonstrative. The velocity maps were made by a program called MKVMAPS, which performed spline interpolation on the line profiles to produce monochromatic images at 20 km s^{-1} intervals. Due to the axial dispersion of the Fabry-Perot spectrometer, velocity maps at the endpoints of the pressure scan sequence are not spatially complete. At the largest blueshifted velocities, the monochromatic images are incomplete near the optical axis; and at the largest redshifted velocities, the images are incomplete outside a certain radius from the axis. These effects are noticable in the velocity channel maps of HH 1 and HH 12, the two objects which only needed a partial scan of the instrument's free spectral range to cover their velocity structure. Full *object* coverage by the partial scans is evident in Figures 5 and 15; the objects' intensity fades as the velocity maps' spatial incompleteness boundary approaches them. In any case, the reader should be aware that the entire field of view was not sampled as thoroughly as the central HH objects were.

Still another way to render the results in the data cubes is in the form of position-velocity diagrams. Long slit spectra are usually presented in this way, and consequently a great deal of HH object modelling has been presented in the form of theoretical position-velocity diagrams (Hartigan, Raymond, and Meaburn 1990; Raga and Bohm 1985). With the spatial coverage and spatial resolution of the Fabry-Perot data cube, any desired long slit spectrum can be synthesized by resampling. A program called PVDIAGRAM was used to to interactively select the endpoints of a synthetic long slit, using a cursor moving over an image of the object. PVDIAGRAM then generated a position-velocity diagram from the desired slit position and specified slit width.

III. Results and Discussion

A. HH 1

Located in the Orion L1641 molecular cloud, HH 1 is one of the brightest Herbig-Haro objects in the sky. As the designation indicates, it was the first object of its class to be cataloged. Physically HH 1 is a slightly arcuate region of line emission, 10″ in diameter, containing several bright knots. The discovery of large, oppositely directed proper motions for HH 1 and its companion object HH 2 (Herbig and Jones 1981) demonstrated that these HH objects are formed in a bipolar outflow. The highly obscured outflow source star identified by Pravdo *et al.* (1985) lies 70″ to the SE of HH 1 and is designated HH 1/2 VLA1. Strom *et al.* (1985) discovered a small optical jet pointing from this source toward HH 1.

HH 1 has been the subject of several detailed spectroscopic studies. All find small radial velocities in the optical emission lines. In view of this and the large

proper motions, it is assumed that this outflow is moving nearly in the plane of the sky. Hartmann and Raymond (1984) find approximate agreement between the observed emission line fluxes and those predicted by bowshock models. Position-velocity diagrams in a number of emission lines (Bohm and Solf 1985) also show general agreement with a bowshock model. Raga *et al.* (1988) have suggested that observed variations in the emission knot structure of HH 1 are due to the growth and decay of thermal instabilities present in their time-dependent bowshock models.

Moment Maps

Figure 4*a* shows the mean LSR radial velocity over the region of HH 1 where the peak spectral signal-to-noise was greater than 5. The measured mean LSR radial velocities lie in the range between -20 and 0 km s^{-1}. Using the knot naming convention of Herbig and Jones (1981), we find that bright knots HH 1F and HH 1A have mean LSR radial velocities of -17 and -10 km s^{-1} respectively. Given the LSR-Heliocentric velocity difference of 18 km s^{-1} in this direction, these results agree well ($<$ 5 km s^{-1}) with those of Hartmann and Raymond (HR, 1984). The lower (*i.e.*, more positive) velocities are found at the periphery of HH 1, especially toward the southeast. [S II] velocity dispersions (Figure 4*b*) change very little over HH 1, with values ranging from 35 km s^{-1} in HH 1A, to 40 km s^{-1} in HH 1F, and 50 km s^{-1} in the southern parts of the object. The [S II] linewidth of HH 1F is almost the same as the Hα linewidth found by HR; however, in HH 1A the [S II] linewidth is substantially greater than the Hα linewidth of HR. It is interesting to note a slight increase of the [S II] linewidth south of HH 1F; this behavior is contrary to that observed in Hα and other bright lines. Peculiar behavior of the [S II] lines was noted by Bohm and Solf (1985), who found that HH 1F's [S II] position-velocity diagram lacked the southern narrow line region seen in other emission lines.

Velocity Channel Maps

In Figure 5, the spatial distribution of HH 1 [S II] emission is shown as a function of LSR velocity. Emission from HH 1F is present in all velocity channels (-120 to +100 km s^{-1}; HH 1A is visible over a smaller velocity range (-80 to +60 km s^{-1}). The positions of the HH 1F and HH 1A emission peaks do not vary significantly as a function of velocity. In the velocity range between -100 and -60 km s^{-1}, the optical jet from VLA 1 can be seen in the southeast corner of the maps. Unfortunately the spectral coverage of this part of the field was incomplete, and thus we have no information about the extent of the jet to radial velocities to the red of -60 km s^{-1}. Nevertheless, our observations do confirm the report by Strom *et al.* (1985) of a high velocity wing of [S II] emission in the VLA 1 jet. Lastly, we find faint emission 20″ south of HH 1F centered at the same radial velocity as most of HH 1.

Line Profiles

At most locations the HH 1 [S II] line profiles have an approximately Gaussian shape. An exception to this is seen at the peak position of HH 1F, where a partially resolved double peak is observed (Figure 6). Two low-amplitude, narrow peaks (at -30 and 0 km s^{-1}) are present atop the broad line component present throughout HH 1. These two peaks are present in a region that has a spatially unresolved seeing profile shape in the east-west direction, and a spatially resolved size of 2″ in the north-south direction. A double peak has not been reported in any previous study of HH 1. The partially resolved double peak is also visible in a position-velocity diagram made with a slit width comparable to the seeing (Figure 7). Allowing the slit to be three times wider washes out the identity of the double velocity peak, however. It is therefore plausible that the double peak in our data might not have

been visible in slit spectra, given typical slit widths and positional uncertainties.

With only a single spectral data point to indicate the central dip in the line profile, we must consider possible spurious sources for this feature in the data. We investigated the possibility that the 'dip' was the result of a data cube image registration error by producing an 'image' of the double peaked region (by adding together the two peak frames and then subtracting the central 'dip' frame twice). The position of the synthesized 'dip peak' was found to be the same as the peak position of HH 1F to within 0.5 pixels (0.2″), thus ruling out misregistration. A transient drop in sky transparency could also produce a 'dip' in our pressure-scanned line profile. If this had occurred we would expect to find an erroneous double peak over a wide area of HH 1, and yet the observed double peak is present only in a small (but spatially resolved) region of HH 1F. We therefore conclude that the best explanation for the double peak in our data is that it is a real structural feature of HH 1F. Future Fabry-Perot observations at higher spectral resolution will be needed to confirm this result.

Interpretation

Shocks at two separate velocities are needed to produce two emission peaks in HH 1. One possibility is that we are seeing distinct emission peaks from both the ambient medium bowshock and the terminal shock of the HH 1 jet. Hartigan (1989) predicts that the terminal jet shock (or Mach disk) should be visible in HH 1 and noted that the spatial separation between it and the bowshock apex may not be large enough to be observable. Although this is an appealing scenario, our data do not fit it very well. The apex of a bowshock is expected to be a region of high velocity dispersion (Raga and Bohm 1985); the linewidth of the small peak near

$v_{rad} = 0$ is much too narrow for it to represent overall bowshock emission. It is also difficult to ascribe the small peak near $v_{rad} = 30$ to a terminal jet shock; because this flow is nearly in the plane of the sky, the observed radial velocity difference between the two peaks would imply a true flow velocity difference of at least 40 and perhaps as much as 100 km s^{-1} between the two emission regions. This velocity difference is so large that *another* visible jet shock would be needed to equalize the jet and bowshock flow velocities at the working surface. This additional shock is not seen in our data, and its existence would spoil the simple interpretation of the observed $v_{rad} = 30$ peak as a jet terminus shock.

Another possibility is that the double peak is produced at the two points where the line of sight intersects the bowshock surface. For a flow in the plane of the sky, models predict that a double peaked line profile should be present over much of the bowshock area (Raga and Bohm 1985; Hartigan, Raymond, and Meaburn 1990). These models predict that a double peak will be most easily observed at regions well separated from the bowshock apex, because the high velocity dispersion of the apex region fills in the gap in the line profile. It is therefore surprising that the double peak in our data is found *only* at the intensity peak of HH 1F, a location which most models of HH 1 agree corresponds to the bowshock apex. Nevertheless, we lean toward a bowshock interpretation for the observed [S II] double peak feature. The fact that the double peaked region is unresolved spatially in the direction perpendicular to the flow axis is reasonable in a bowshock model, for emission on the flow axis should be double peaked while emission from the bowshock limbs should not.

Although emission from the HH 1 jet is centered at radial velocities comparable to those of HH 1 itself, the jet also includes a blue wing of emission not present

in HH 1 (Strom *et al.* 1985). Our observations confirm the reality of this feature in [S II]. It is surprising to find such a high radial velocity feature within a flow that is generally agreed to be moving in the plane of the sky. The blue wing is seen only in the low excitation [O I] and [S II] emission lines, a characteristic that suggests an origin in low velocity or oblique shocks. Both Strom *et al.* (1985) and Solf and Bohm (1991) have suggested that this blue wing could be produced by the scattering of jet line emission by nearby dust.

B. HH 7-11

HH 7-11 is a complex of optical emission line nebulosity associated with the molecular outflow eminating from SVS 13, a highly obscured young star. A neutral atomic wind is believed to carry most of the momentum in the outflow (Lizano *et al.* 1987). Proposed models for shock emission in HH 7-11 include shocked ambient cloudlets (Rudolph and Welch 1988); Kelvin-Helmholtz instabilities at the walls of a jet (Garden, Russell, and Burton 1990); and even a precessing helical jet (Lightfoot and Glencross 1986). The most complete kinematic study of HH 7-11 was made by Solf and Bohm (SB, 1987). The kinematics of the H_2 2.12 μm line emission have been studied by Carr (1991) and Zinnecker *et al.* (1989), who find generally lower radial velocities than those seen in the optical lines.

At the Palomar 60 inch telescope in December 1990, we observed that SVS 13 had brightened by two magnitudes in the red since a previous observing run in November 1988. This brightening has been also been independently discovered by R. Mundt (S. Beckwith, personal communication). No significant variability has been previously reported for this source. This behavior is reminiscent of an FU Orionis eruption, a rapid brightening which has been observed in a small number

of pre-main sequence stars (Kenyon and Hartmann 1988). If similar past eruptions have occurred during the flow lifetime, there is a possibility of significant time variation in the outflow characteristics which could be reflected in the HH object kinematics.

HH 7

HH 7 is a comet shaped region of emission line nebulosity at eastern end of the chain of HH objects excited by SVS 13. Two bright emission knots are present in the core of HH 7, surrounded by a plateau of emission that extends westward toward HH 8 and SVS 13. Bright infrared molecular hydrogen emission has been found in HH 7, coinciding with the eastern optical peak (see Chapter II).

The velocity field of HH 7 exhibits systematic structure which is very revealing of the outflow kinematics. Mean velocities plotted in Figure 8 are highest at the center of HH 7 and smoothly decrease away in all directions. The two bright peaks in HH 7 are centered at velocities of -60 and -70 km s^{-1}, with the lower velocity peak 3″ E of the latter (*i.e.*, further from SVS 13). Also present in Figure 9 is a plateau of emission extending back towards SVS 13 at high to intermediate velocities (-100 to -20 km s^{-1}), and low velocity (-20 to 0 km s^{-1}) emission at the northern and southern tips of HH 7.

The kinematics within HH 7 is best seen in the velocity channel maps (Figure 9) and in a position-velocity diagram made with a slit running east to west across the two peaks (Figure 10). In the latter figure, one can clearly see two kinematic components: A broad feature at -60 km s^{-1} which is brightest on the eastern peak but which is present throughout the diagram; and a narrower component at -85 km s^{-1} centered at HH 7's western peak. The narrow high velocity feature stands on a

pedestal of broader emission, yielding an asymmetric line profile in western HH 7. The presence of multiple velocity components in HH 7 was suggested by Solf and Bohm (1987), who were able to infer velocities comparable to those reported here by multicomponent fitting of their long slit spectra. They were unable to associate the high velocity component with HH 7's western knot, however, apparently because their slits only grazed the position of that object. As can be seen in Figure 9, the highest velocity emission (-140 to -100 km s^{-1}) is clearly concentrated in the western knot. From the Gaussian fitting we find that the high velocity component makes up about half the total [S II] intensity from the western HH 7 peak.

The kinematic structure of HH 7 is remarkably similar to that expected for the working surface of a supersonic stellar jet. A bow shock in the ambient medium is suggested by the cometary shape of HH 7, its position as the last HH object in the chain associated with SVS 13, and by the molecular hydrogen emission. At the wings of the bowshock we expect to see lower projected postshock velocities and this is precisely what is observed on the northern and southern edges of HH 7. Theoretical models for the jet working surface also predict a terminal jet shock (or Mach disk) in the wind material. This shock is expected to have emission at velocities greater than or equal to the bowshock velocites, but with narrower linewidths, and with intensity comparable to that of the bowshock apex (Hartigan 1989). The -85 km s^{-1} velocity component that delineates the western HH 7 emission peak has these properties and is in about the right location for a terminal jet shock. It also lacks the H_2 emission characteristic of the shocked ambient medium in HH 7-11, suggesting that it is shocked jet/wind material.

In a simple bowshock model without an interior jet shock, higher radial velocities can be observed on the outflow source side of the bowshock apex. This

can occur because the radial component of the postshock velocity increases as the bowshock surface curves toward the observer; the exact behavior depends on the orientation of the bowshock to the line of sight. It does not appear that this effect can account for the high velocity component in western HH 7. A gradually curving bowshock should show a smooth increase in radial velocity away from the apex; the observations show a discontinuous radial velocity jump between eastern and western HH 7 (Figure 10). If the western HH 7 peak had a bowshock origin, it is also difficult to understand why it lacks H_2 emission. We therefore conclude that a terminal jet shock best explains the properties of the western HH 7 emission peak.

Norman, Winkler, and Smarr (NWS 1983) have carried out numerical simulations of the propagation of gaseous jets, and find that density ratio between the jet and the ambient medium has an important effect on the flow morphology. In particular, a light jet boring into a dense ambient medium develops a thick surrounding cocoon of turbulent gas, whereas a dense jet does not. The observed kinematics of HH 7 permit an approximate determination of this density ratio. For a steady flow, the rate at which momentum is input to the ambient medium must equal the rate at which it is lost from the jet. Assuming pressure equilibrium at the contact discontinuity between two cooled postshock gases, momentum conservation at the head of the jet can be expressed quantitatively as

$$\rho_j \left(v_j - v_{bs}\right)^2 = \rho_a v_{bs}^2 \tag{5}$$

where ρ_j and ρ_a are respectively the preshock densities of the jet and ambient medium, v_j is the jet flow velocity, and v_{bs} is the bowshock velocity. A static ambient medium is assumed. This equation can be re-expressed to show the jet/ambient

medium density ratio in terms of observed quantities:

$$\left(\frac{\rho_j}{\rho_a}\right) = \frac{v_{bs}^2}{(v_j - v_{bs})^2} \tag{6}$$

Assuming that the same projection angle applies for both the jet and bow shock allows the use of measured radial velocities in equation (6). From Figure 10, the bowshock radial velocity is about 60 km s^{-1}. Our observations do not determine the jet radial velocity; the -85 km s^{-1} component in HH 7 represents jet material that has already been shocked. We will adopt 150 km s^{-1} as the jet radial velocity, a compromise value between the H I radial velocity of Lizano *et al.* (1987) and the CO radial velocity of Carlstrom and Narayanan (1991). Substituting these values, and allowing a factor of two for the effects of jet propagation efficiency (NWS), we find the jet and ambient medium densities to be comparable in HH 7-11.

In HH 34 and HH 47, similar analyses have yielded a jet/ambient density ratio of about 50 (Hartigan 1989). Considering the relative brightnesses of H_2 emission from HH 7-11, HH 34, and HH 47, it is not surprising that for HH 7-11 (which has bright H_2 emission) the jet/ambient density ratio is much lower than for HH 34 and HH 47 (which show no associated H_2 emission). HH 7-11 is therefore the first HH object outflow where ρ_j/ρ_a is *not* $\gg 1$.

A dense ambient medium for HH 7 helps to reconcile a discrepancy noted by Solf and Bohm (1987): why would a high velocity outflow (as evidenced by the kinematics of HH 11, see below) have such a low excitation emission spectrum at its terminus ? A jet much denser than the ambient medium will easily bore through it, and will shock the ambient medium at nearly the jet velocity. Jets with a density

less than or comparable to the ambient medium cannot accelerate the ambient medium to near-jet velocities as easily. As a result, a "light" jet dissipates a greater fraction of its flow kinetic energy at the terminal jet shock than does a "heavy" jet, which dissipates most of its energy at the ambient medium bowshock. In other words, a "light" jet will show lower-excitation bowshock emission than a "heavy" jet of the same velocity. The dissociation energy of H_2, and the smoothing of the shock transition by a magnetic precursor are two effects which also act to reduce the bowshock's emission line excitation.

HH 8

HH 8 is composed of two compact knots of emission separated by 4″ along the flow axis. The brighter eastern knot is spatially coincident with a knot of H_2 emission. At the fainter western knot, H_2 emission is displaced 1″ east (or downstream) of the optical emission peak (Chapter II). The presence of stronger shocks in western HH 8 is indicated by the smaller [S II]/Hα ratio in this region. Our radial velocity data show that both knots are centered at -65 km s^{-1}; there is some indication of larger velocity dispersions for the western knot (100 km $^{-1}$ versus 70 km s^{-1}). The western knot also includes a narrow (30 km s^{-1} FWHM) component centered at -30 km s^{-1} not present in eastern HH 8.

The velocity structure of HH 8 does not provide much insight into the nature of the object. It is not clear whether the two peaks of HH 8 arise from single or multiple flow obstacles. The slight H_2 offset from the western HH 8 peak suggests that that shocked ambient material is displaced downstream from shocked wind material at this location, in which case the western peak could represent a distinct flow obstacle. In such case the eastern peak might be considered a separate obstacle, perhaps an unresolved shocked cloudlet.

HH 9

This is the smallest and faintest of the objects comprising HH 7-11. It lies 10″ north of the axis between SVS 13 and HH 7. We find that HH 9 has the lowest mean radial velocity (-10 km s^{-1}; dispersion 35 km s^{-1}) in the HH 7-11 complex. The shape of HH 9 is pointlike, although a faint extension to the NW (toward the observed 1.64 μm [Fe II] peak) is observed in our -20 km s^{-1} channel map.

To the north of HH 9, there are three faint unnamed HH objects spaced along a line running west back to SVS 13. The [S II] emission from these three objects is kinematically identical to that found in HH 9.

HH 10

This is a large, bright object at the western edge of a continuous bridge of emission that extends to HH 7. Millimeter molecular line observations have found emission peaks of CO and HCO^+ just to the east of HH 10 (Grossman *et al.* 1987; Rudolph and Welch 1988), leading to the suggestion that this object may be a shocked clump of ambient medium. The velocity structure of this object is enigmatic. A velocity gradient is present between the S (-30 km s^{-1}) and N (-5 km s^{-1}) sides of the object (see Figure 11). It is noteworthy that this velocity gradient is oriented nearly perpendicular to the direction to SVS 13. Our observations confirm Solf and Bohm (1987)'s report of [S II] velocities 30 km s^{-1} smaller than Hα velocities in this object. The molecular hydrogen emission peak in HH 10 is found at the southern end of the object, as is the largest [S II]/Hα ratio (Hartigan, Curiel, and Raymond 1989). These two indicators show that the low excitation conditions are inversely correlated with radial velocity in HH 10. Our velocity channel maps of HH 10 are presented in Figure 12.

A correlation between low excitation and high radial velocities is expected in a shocked cloudlet model, where gas impacting the couldlet head-on passes through stronger shocks than gas near the side which is shocked obliquely. However, such a cloudlet should show symmetric low excitation, higher velocity regions on each side of its higher excitation, lower velocity center — which HH 10 does not. This analysis applies to shocked wind material only; since we believe no H_2 is present in the outflowing wind (Chapter II), the shocked H_2 at the southern edge of HH 10 must then be explained separately, perhaps by wind ablation of cloudlet material. A modified cloudlet model, such as a cloudlet partially embedded in the walls of the flow cavity, is needed to account for the observations of HH 10.

The velocity difference observed between the Hα and [S II] lines has two possible explanations: (1) the flow of shocked wind gas is slowed or curved on a timescale short compared the the cooling time; or (2) much of the [S II] emission arises in shocked ambient material, whereas the Hα emission is predominantly from wind material. The fact that the [S II] and H_2 radial velocities are similar in HH 10 (J. Carr, personal communiation) argues in favor of the latter explanation.

HH 11

HH 11 is the only HH object associated with SVS 13 which exhibits significant proper motion (Herbig and Jones 1983); the inferred transverse velocity is 60 km s^{-1} directly away from SVS 13. HH 11 also has the largest radial velocities (-200 to -140 km s^{-1}, Solf and Bohm 1987) in the HH 7-11 complex, and no emission at zero radial velocity. HH 11 has a low excitation optical emission spectrum, and yet lacks any coincident molecular hydrogen emission (Chapter II). The combination of high radial velocity and low excitation emission suggests that HH 11 originates from shocks within a moving medium (Hartigan, Raymond, and Hartmann 1987).

Our Fabry-Perot observations of HH 11 did not extend to radial velocities blueward of -200 km s^{-1}. Lacking data on the blue line wing, we cannot determine the mean velocities and velocity dispersions for most of this object. Velocity channel maps can be made over a limited range, however, and we find emission from HH 11 extending down to the -60 km s^{-1} channel. As the emission fades, the peak moves 3″ to the SW. At this position the [S II] emission spatially overlaps a faint knot of H_2 emission seen in infrared images (Chapter II, Figure 2). Recent high resolution mapping has shown that at this position, the CO radial velocity is about the same as the [S II] (Carlstrom and Narayanan 1991). This CO emission is believed to be high velocity neutral wind gas and not swept up matter because the highest velocity CO (at -120 km s^{-1}) is observed within 5″ of SVS 13. We therefore conclude that shocks formed *within* the outflowing gas provide a reasonably consistent explanation for the low excitation of HH 11. The geometry of these shocks cannot be as simple as the crossing shocks thought responsible for the emission in the HH 34 and HH 111 jets (Reipurth 1989), because the HH 11 emission line velocity dispersions are significantly larger (90 vs 30 km s^{-1}). A jet that possesses a high velocity core and lower velocity envelope could produce crossing shock emission with the linewidths observed in HH 11.

C. HH 12

HH 12 is an extended region of emission line nebulosity coincident with the blue lobe of a molecular outflow (Edwards and Snell 1983). Morphologically, this object is characterized by many bright emission knots (designated A-G by Herbig and Jones 1983) and by a secondary component of widespread diffuse emission. The distribution of near-infrared molecular hydrogen emission in this field was discussed

in Chapter II, where it was shown to be very clumpy with little or no extended emission. The northern half of HH 12 resembles a large resolved bowshock concave open to the east. Blushifted radial velocities of -65 km s^{-1} have been reported for an unspecified region of HH 12 by Strom, Grasdalen, and Strom (1976).

There are two prominent candidates for the outflow source: HH 12/107, an optically visible star which lies along a wisp of Hα emission 90″ to the south; and SVS 12, an infrared source located 20″ to the east. The primary argument in favor of HH 12/107 is given by the observed northward-pointing proper motions of HH 12 (Herbig and Jones 1983). Strom *et al.* (1983) suggested that a wisp of Hα emission associated with HH 12/107 was an optical jet directed at HH 12 from this star. However, this wisp does not show the low-excitation character (bright [S II] emission) seen in other stellar jets; and it does not become redshifted on the side of HH 12/107 opposite HH 12, as would be expected for a counterjet (Strom *et al.* 1986). Arguments in favor of SVS 12 rest primarily on the star's proximity to HH 12 and the statistical statement that HH object exciting stars are usually optically obscured infrared sources.

An unusual explanation is required to reconcile the northward HH 12 proper motions with the choice of SVS 12 as the exciting star. In HH 1 and HH 2 proper motion vectors point back toward the obscured exciting star, suggesting that the proper motions represent genuine flow velocities in the plane of the sky. In HH 12 the proper motion vectors are oriented roughly perpendicular to the direction of SVS 12. To adopt SVS 12 as the exciting star one must interpret the HH 12 proper motions as phase effects (such as a moving jet striking a stationary screen), and not as genuine flow velocities.

Cohen and Jones (1987) have conducted a spectral study of the northeastern edge of HH 12. They describe this region (including knot G) as a collimated optical jet eminating from SVS 12. The region is covered by diffuse emission extending to the south and west, and its interpretation as an optical jet is not an obvious one. CJ report radial velocities of -100 km s^{-1} for the 'jet', significantly different from the velocities reported elsewhere in HH 12. This velocity difference, the association of the 'jet' with SVS 12, and the southern outflow source suggested by the proper motions led CJ to propose that HH 12 may be a composite Herbig-Haro object energized by two separate but overlapping outflows.

It is somewhat improbable that two outflows from widely separated sources would be found to overlap each other on the sky, since HH objects are not a common phenomenon. In addition, the significance of the radial velocity difference between the SVS 'jet' of CJ and the rest of HH 12 is questionable because (1) The CJ spectra are of only moderate resolution ($\approx$ 13Å); and (2) CJ did not make comparative radial velocity measurements elsewhere in HH 12. The radial velocity difference in question (35 km s^{-1}) is thus comparable to the measurement errors of CJ. These considerations point to the need for a comprehensive kinematic study of HH 12 so that the overlapping outflow model can be properly tested.

Moment Maps

Figure 13 shows the mean LSR radial velocity and velocity dispersions over the region of HH 12 where the peak spectral signal-to-noise was greater than 5. The measured mean radial velocities lie in the range between -60 and 0 km s^{-1}, with the majority the emission between -40 and -20 km s^{-1}. The largest radial velocities are found at the positions of HH 12B (-50 km s^{-1}) and HH 12F (-60 km s^{-1}), the lowest found at the western periphery of HH 12. The velocity dispersions are remarkably

uniform, staying in the 35-40 km s^{-1} range over the entire object.

Velocity Channel Maps

In Figure 14, the spatial distribution of HH 12 [S II] emission is shown as a function of LSR velocity. The blue wings of HH 12B and HH 12F (the knots with the most negative radial velocities) are apparent in the -100 km s^{-1} channel. All the major knots are apparent in the -60 km s^{-1} channel, including those in NE HH 12 for which a link to SVS 12 is indicated. At the north of HH 12 in the -40 km s^{-1} channel map, there is a broken line of low-intensity emission aligned in the direction toward SVS 12. This feature, signs of which are also present in the -60 km s^{-1} channel, is very likely what CJ described as the SVS 12 'jet'. Our results show no evidence of -100 km s^{-1} velocities in the region, as reported by CJ. Given that our observations are of much higher spectral resolution, we adopt our value of -45 km s^{-1} as the correct radial velocity for the 'jet ' feature. This is significant, since it implies that this region is not kinematically distinct from the rest of HH 12. Nearby knot HH 12B, which is reported to show the largest northward proper motion in the system (Herbig and Jones 1983), has virtually the same radial velocity as the 'jet' feature. Finally, we note that the red wings of HH 12 C,D, and E are apparent in the +20 km s^{-1} velocity channel, where it can be seen that the most positive radial velocities are found on the western sides of HH 12C and HH 12D.

Position-Velocity Diagrams

Position-velocity diagrams of HH 12C and HH 12D (Figures 15*a* and 15*b*) show a gradual decrease in radial velocity with increasing distance from SVS 12. The smooth decrease in velocity could well be due to projection effects; as the wall of the outflow cavity becomes tangent to the line of sight, the observed radial velocity

should decrease. These velocity gradients are the largest within HH 12, and they are oriented toward SVS 12.

Interpretation

The velocity field of HH 12 does not show a bimodal structure. If HH 12 was formed by two overlapping outflows, then the fact that they are kinematically indistingushable must be regarded as purely coincidental. There is a weak correlation between the knot radial velocities measured here and the proper motions of Herbig and Jones (1983): knots B and F have the highest radial velocities, highest excitations from the Hα/ [S II] ratio, and the largest proper motions in HH 12, whereas knots D and E show lower proper motions, excitations, and radial velocities. The correlation is not as striking here as it is in HH 7-11, where the radial velocity of the high proper motion object HH 11 is very distinct (by 140 km s^{-1}) from the rest of the system.

The proper motion of HH 12B (15″/cent; HJ 1983), if interpreted as the true velocity of outflowing material, implies a space motion of 250 km s^{-1}. Unless the pre-shock medium is already moving with respect to the LSR, shocks with strength comparable to the outflow velocity must be present in HH 12B. The signature of a shock in a moving medium is that the emission line profile does not include zero velocity; examples of this are the crossing shocks in the HH 34 jet, which have low excitation, narrow linewidth, and high radial velocity (Buhrke, Mundt, and Ray 1988). As is evident from Figure 14, the line profile of HH 12B includes zero velocity. In a bowshock geometry this observation implies no significant motion of the preshock medium (Hartigan, Raymond, and Meaburn 1990), and therefore that shock velocities as high 250 km s^{-1} must be present in HH 12B. It is difficult to reconcile this result with the presence of bright molecular hydrogen emission in knot

B, for H_2 is completely dissociated in hydrodynamic shocks at velocities above 50 km s^{-1}. Unless a strong magnetic field is present in the ambient medium (which seems unlikely given the jumbled appearance of HH 12), we therefore have a contradiction in HH 12B: the large shock velocities implied by the proper motions are in conflict with the presence of H_2 emission. In HH 12F the line profile is displaced from zero velocity (by about 20 km s^{-1}), thus permitting a moving medium interpretation and preventing any direct contradiction between our observations and the proper motions.

The observed velocity gradients in an idealized bowshock are predicted to point back toward the outflow source (Raga and Bohm 1986). The trend toward lower radial velocities at the western side of HH 12 suggests that an outflow from SVS 12 is slowing as it interacts with the ambient medium. It is significant that these areas of low [S II] velocities are the same areas where H_2 emission is observed in western HH 12; the observed velocity gradient may due to an emission transition from shocked wind material to shocked ambient material. A similar interpretation can be made for HH 12F, where lower radial velocities and H_2 emission can be found on the side of the object opposite SVS 12; and in HH 7, where the high velocity peak lacks H_2 emission. The shape of western HH 12 is suggestive of a large resolved bowshock concave open to SVS 12. Given the kinematic evidence for SVS 12 as the outflow source and the difficulty reconciling the proper motions and H_2 emission in HH 12B, it appears that the proper motion of HH 12B does not reflect the true space velocity of outflowing material.

In addition to the velocity data, two other arguments can be made to link SVS 12 and HH 12. First is the good geometrical alignment between SVS 12, the axis of its infrared reflection nebula, and the NE edge of HH 12 (knots G and

H). This alignment suggests a physical association, perhaps a 'wall' of molecular cloud material which both reflects starlight and is weakly shocked by the stellar wind. Secondly, the SVS 12 infrared reflection nebula actually overlaps diffuse [S II] emission at the edge of HH 12 (see Chapter II, Figure 6). For the optically obscured reflection nebula to overlap the visible edge of HH 12, a large extinction gradient must be present between HH 12 and the nebula. It therefore appears that the high extinction environment of SVS 12 defines the northeastern visible boundary of HH 12. This relationship is to be expected if SVS 12 is the exciting star, whereas it can only be explained as a chance superposition if another exciting star is chosen. Note that the extinction proximate to HH 12 apparently does not obscure significant shock emission regions, because no optically invisible knots were revealed in the infrared H_2 and [Fe II] images of the region (chapter II).

IV. Conclusions

(1) The kinematic structure of HH 7 is well described by a jet working surface, with the bow shock as the dominant contributor to the optical emission. Within the bowshock we have isolated the terminal shock of the SVS 13 jet, as distinguished by its location, kinematics, and emission spectrum.

(2) We have found two narrow, low-intensity emission peaks superposed on

the broad line emission in a small region of HH 1F. This kinematic feature is best understood as emission from the two points where the line of sight intersects the surface of an axisymmetric bowshock. However, the location and spatial extent of this feature differ from the standard predictions of a bowshock model.

(3) HH 12 shows a relatively smooth velocity structure, with no kinematic evidence for overlapping outflows. Velocity gradients within the object are oriented toward SVS 12. The kinematics and emission spectrum of HH 12B are difficult to reconcile with the assumption that the object's proper motion reflects the true flow velocity. The total weight of evidence thus favors SVS 12 as the only exciting star for HH 12, and that the proper motions represent pattern motion within in the outflow. This result shows that HH object proper motions should be interpreted with caution.

(4) In regions where [S II] and H_2 emission knots are spatially coincident, we observe lower [S II] radial velocities. This observation is explained as [S II] emission arising in *both* ambient medium and wind material shocks, with lower velocities in the shocked ambient medium.

(5) In all three regions studied, the highest radial velocities are observed at the brightest emission peaks. Radial velocities decrease systematically away from these peaks, usually in the direction downstream from the exciting source.

Acknowledgements

We express our thanks to the staff of Palomar Observatory for their assistance with the observations and instrument set-up. We also thank Deborah Padgett (CIT)

for help with the observations, Jim Westphal for the use of the Mark V CCD system, and Brian Gordon (JPL) for writing the SFLOOP subroutine that improved the data reduction software. Jeff Hester (IPAC) participated in several useful conversations. KRS acknowledges the support of a NASA Graduate Fellowship.

References

Bland, J. and Tully, R. B. 1989 AJ 98 723

Bohm, K.-H., and Solf, J. 1985 Ap.J. 294 533

Born, M. and Wolf, E. 1986 *Principles of Optics* 6th edition Pergamon Press New York

Burhke, T., Mundt, R., and Ray, T. P. 1988 Astr.Astrophys 200 99

Carlstrom, J. and Narayanan, G. 1991 in preparation.

Cohen, M. C., and Jones, B. F. 1987 Ap.J. 321 846

Garden, R. P., Russell, A. P. G., and Burton, M. G. 1990 Ap.J. 354 232

Grossman, E. N., Masson, C. R., Sargent, A. I., Scoville, N. Z., Scott, S. L., and Woody, D. P. 1987 Ap.J. 320 356

Hartigan, P. 1989 Ap.J. 339 987

Hartigan, P., Raymond, J., and Meaburn, J. 1990 Ap.J. 362 624

Hartigan, P., Curiel, S., and Raymond, J. 1989 Ap.J. 347 L31

Hartigan, P., Raymond, J., and Hartmann, L. 1987 Ap.J. 316 323

Hartmann, L. and Raymond, J. C. 1984 Ap.J. 276 560

Herbig, G. H., and Jones, B. F. 1983 AJ 88 1040

Herbig, G. H., and Jones, B. F. 1981 AJ 86 1232

Hollenbach, D. and McKee, C. F. 1989 Ap.J. 342 306

Kenyon, S. J., and Hartmann, L. 1988 Ap.J. 325 231

Lightfoot, J. F., and Glencross, W. M. 1986 MNRAS 221 993

Lizano, S., Heiles, J., Rodriguez, L., Koo, B., Shu, F. H., Hasegawa, T., Hayashi, S., and Mirabel, I. F. 1988 Ap.J. 328 763

Mundt, R., Brugel, E. W., and Buhrke, T. 1987 Ap.J. 319 275

Mundt, R. (1985) in *Protostars and Planets II*, D. C. Black and M. S. Matthews eds., University of Arizona Press, Tuscon, p. 414.

Norman, M. L., Winkler, K.-H. A., and Smarr, L. (1983) in *Astrophysical Jets*, A. Ferrari and A. G. Paholczyk eds., Reidel Publishing, Dordrecht, pp. 227-251.

Peck, E. R. and Khanna, B. N. 1966 J.Opt.Soc.Am. 56 1059

Perek, L. and Kohoutek, L. 1967 *Catalog of Galactic Planetary Nebulae* Czechoslovak Academy of Sciences, Prague

Pravdo, S. H., Rodriguez, L. F., Curiel, S., Canto, J., Torrelles, J. M., Becker, R. H., and Sellgren, K. 1985 Ap.J. 293 L35

Raga, A. C., and Bohm, K.-H. 1985 Ap.J.Suppl. 58 201

Raga, A. C., Mateo, M., Bohm, K.-H., and Solf, J. 1988 AJ 95 1783

Reipurth, B. in *Low Mass Star Formation and Pre-Main Sequence Objects*, ESO Conference Proceedings No. 33 (1989), ed. Bo Reipurth, p. 247

Rudolph, A., and Welch, W. J. 1988 Ap.J. 326 L31

Schwartz, R. D. 1983 Ann.Rev.Astr.Astrophys. 21 209

Schwartz, R. D. 1975 Ap.J. 195 631

Solf, J. 1987 Ast.Astrophys. 184 322

Solf, J. and Bohm, K.-H. 1987 AJ 93 1172

Stapelfeldt, K. R., Beichman, C. A., Hester, J. J., Scoville, N. Z., and Gautier, T. N. III 1991 ApJ 371 226 (chapter II)

Strom, K. M., Strom, S. E., Wolff, S. C., Morgan, J., and Wenz, M. 1986 Ap.J.Suppl. 62 39

Strom, K. M., Strom, S. E., and Stocke, J. 1983 Ap.J. 271 L23

Strom, S. E., Strom, K. M., Grasdalen, G. L., Sellgren, K., Wolff, S., Morgan, J., Stocke, J., and Mundt, R. 1985 AJ 90 2281

Strom, S. E., Grasdalen, G. L., and Strom, K. M. 1974 Ap.J. 191 111

Trauger, J. T. 1976 Appl.Opt. 15 1989

Von Hippel, T., Bell-Burnell, S. J., and Williams, P. M. 1988 Ast.Astrophys.Suppl. 74 431

Zinnecker, H., Mundt, R., Geballe, T. R., and Zealey, W. J. 1989 Ap.J. 342 337

CHAPTER III. FIGURE CAPTIONS

Figure 1. A sketch of the optical arrangement of the Fabry-Perot imaging spectrometer.

Figure 2. This calibration image shows the ring pattern produced on the detector when observing the dome flat screen illuminated by an Hα lamp. The N_2 pressure was 2700 torr.

Figure 3. Instrument spectral line profile, derived from the Hα calibration frame shown in Figure 2. The instrumental full width at half maximum is 30 km s^{-1}.

Figure 4. Moment maps of the [S II] kinematic structure of HH 1. Values for first velocity moment (central velocity) are shown on panel *a*; values for the second velocity moment (corresponding to the line half-width) are shown on panel *b*. All velocities are LSR. Dotted contours of total [S II] intensity are shown on both panels; the contour interval is a factor of $\sqrt{2}$.

Figure 5. Velocity channel maps of HH 1 [S II] emission, shown in contour representation. The central LSR velocity of each channel is indicated on each of the twelve panels; the velocity width of each is 30 km s^{-1}. The contour interval is a factor of $\sqrt{2}$, with identical contour levels for all maps. A dotted line marks each map's spatial completeness boundary (discussed in section II).

Figure 6. Gaussian-fitted line profiles from a region centered on HH 1F. Each panel shows binned data from a 1.4″ square region of sky. The spatial relationship of the panels is the same as coordinates on the sky: north is up, and east is to the

left. A double peaked line profile is just spectrally resolved. Spatially, the double peaked region is unresolved in the east-west direction and barely resolved to a size of 2″ in the north-south direction.

Figure 7. A position-velocity diagram of HH 1F. The slit was placed on a line running NNW through HH 1F, with a width of 1.4″. The contour interval is a factor of $\sqrt{2}$. The double peak in HH 1F can be seen.

Figure 8. Moment maps of the [S II] kinematic structure of HH 7. Values for first velocity moment (central velocity) are shown on panel *a*; values for the second velocity moment (corresponding to the line half-width) are shown on panel *b*. All velocities are LSR. Dotted contours of total [S II] intensity are shown on both panels; the contour interval is a factor of $\sqrt{2}$.

Figure 9. Velocity channel maps of HH 7 [S II] emission, shown in contour representation. The central LSR velocity of each channel is indicated on each of the nine panels; the velocity width of each is 30 km s^{-1}. The contour interval is a factor of $\sqrt{2}$. The position of the H_2 emission peak is marked by a cross.

Figure 10. A position-velocity diagram of HH 7, made with a slit width of 4.2″. The contour interval is a factor of $\sqrt{2}$.

Figure 11. Moment maps of the [S II] kinematic structure of HH 10. Values for first velocity moment (central velocity) are shown on panel *a*; values for the second velocity moment (corresponding to the line half-width) are shown on panel *b*. All velocities are LSR. Dotted contours of total [S II] intensity are shown on both panels; the contour interval is a factor of $\sqrt{2}$.

Figure 12. Velocity channel maps of HH 10 [S II] emission, shown in contour representation. The central LSR velocity of each channel is indicated on each of the twelve panels; the velocity width of each is 30 km s^{-1}. The contour interval is a factor of $\sqrt{2}$.

Figure 13. Moment maps of the [S II] kinematic structure of HH 12. Values for first velocity moment (central velocity) are shown on panel *a*; values for the second velocity moment (corresponding to the line half-width) are shown on panel *b*. All velocities are LSR. Dotted contours of total [S II] intensity are shown on both panels; the contour interval is a factor of $\sqrt{2}$.

Figure 14. Velocity channel maps of HH 12 [S II] emission, shown in contour representation. The central LSR velocity of each channel is indicated on each of the eight panels; the velocity width of each is 30 km s^{-1}. The contour interval is a factor of $\sqrt{2}$. A dotted line marks each map's spatial completeness boundary (discussed in section II).

Figure 15. Two position-velocity diagrams of HH 12. Both were made with east-west oriented slits; as shown, left is the direction to SVS 12. A fixed contour interval was used. Panel *a* shows the velocity stucture within HH 12C; panel *b* shows the same for HH 12D.

Figure 1

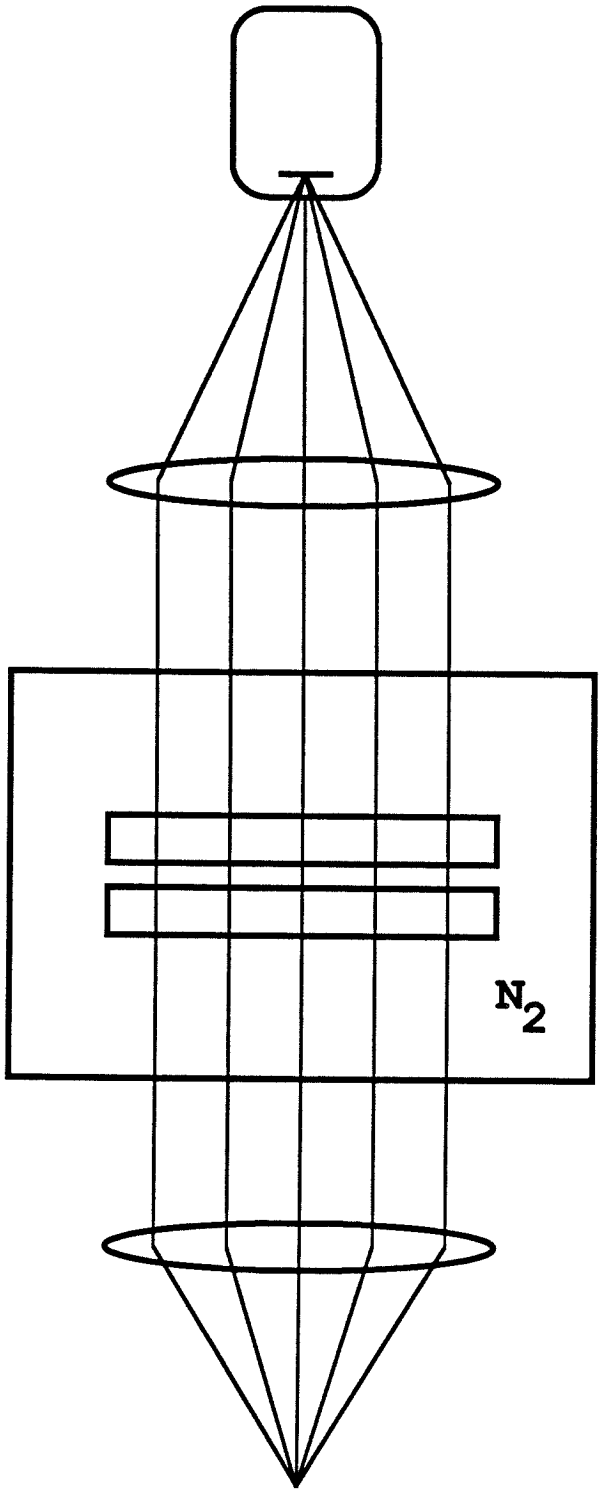

CCD Dewar

Camera Lens

Fabry-Perot
Etalon

Pressure Vessel

Collimating Lens

200 inch
Prime Focus

Figure 2

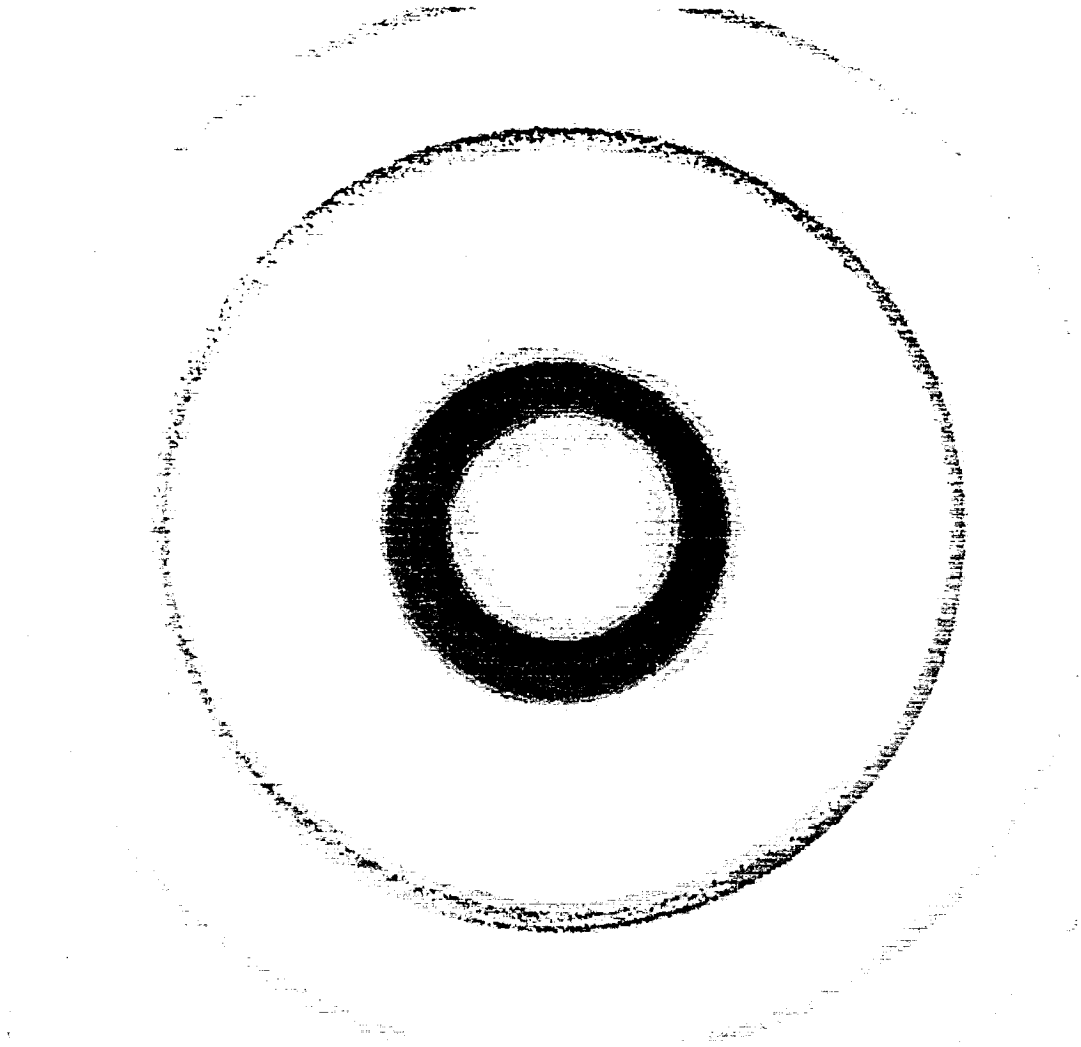

Figure 3

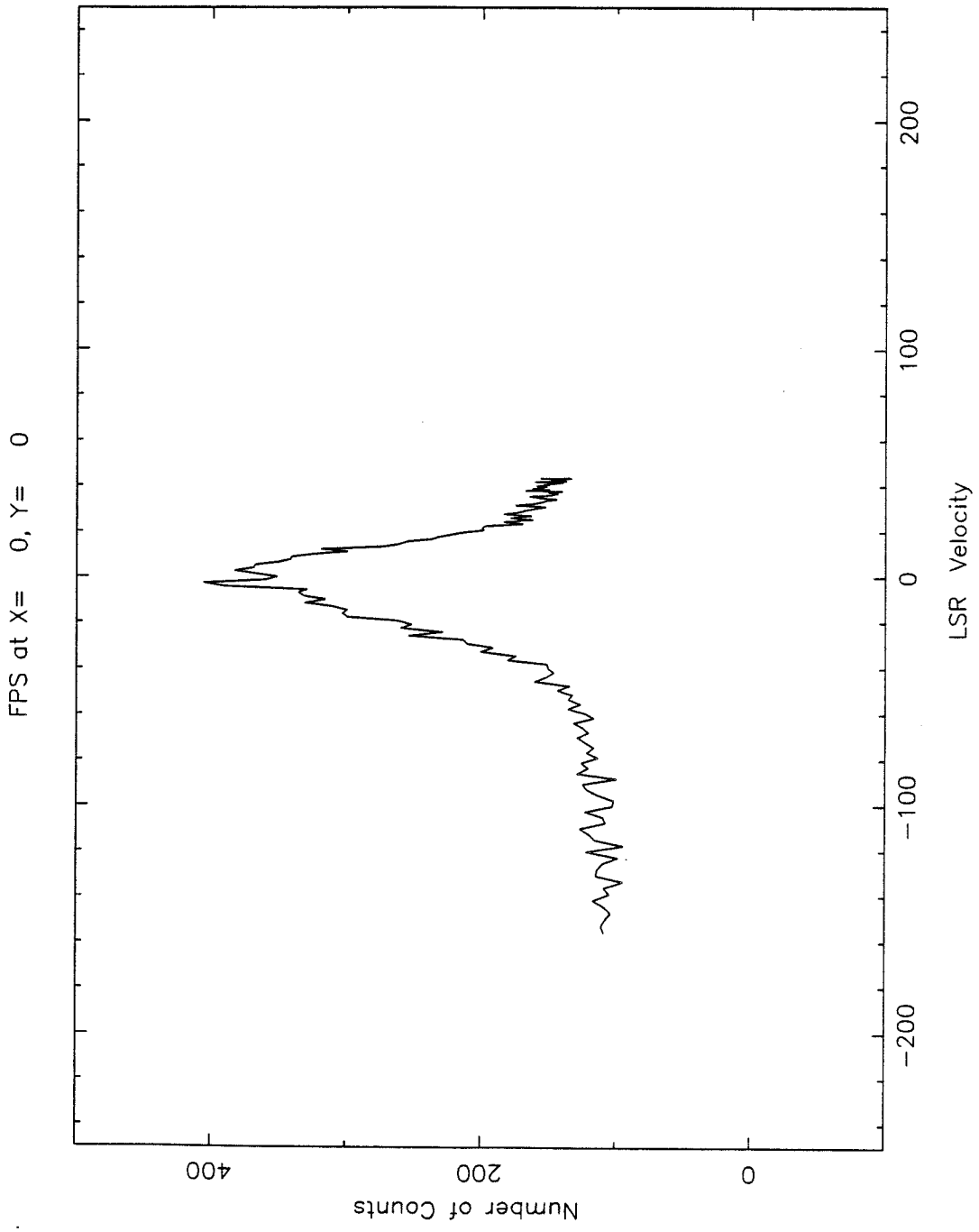
FPS at X= 0, Y= 0
Number of Counts
0
200
400
LSR Velocity
200
100
0
-100
-200

Figure 4a

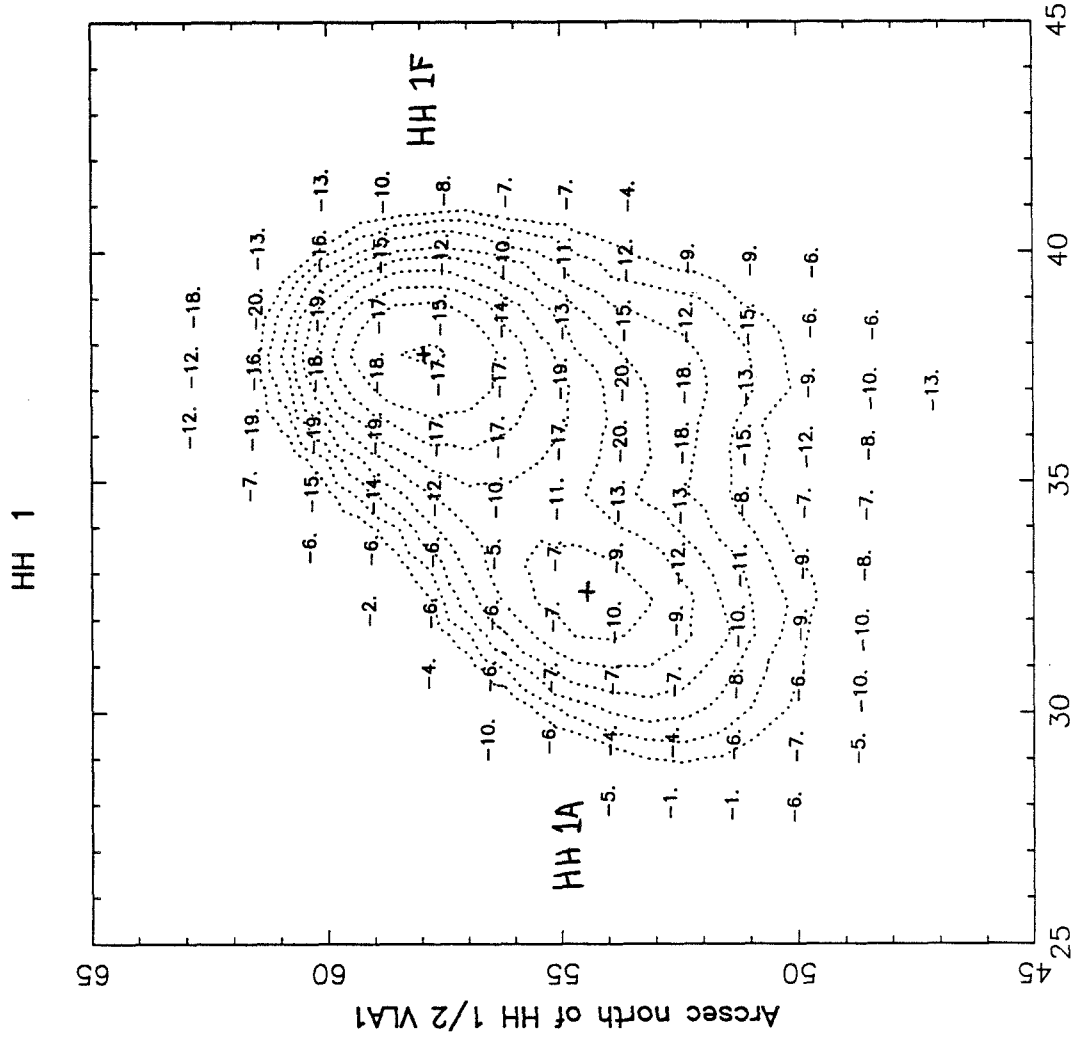
HH 1
HH 1F
HH 1A
Arcsec north of HH 1/2 VLA1
Arcsec west of HH 1/2 VLA1
65
60
55
50
45
45
40
35
30
25

Figure 4b

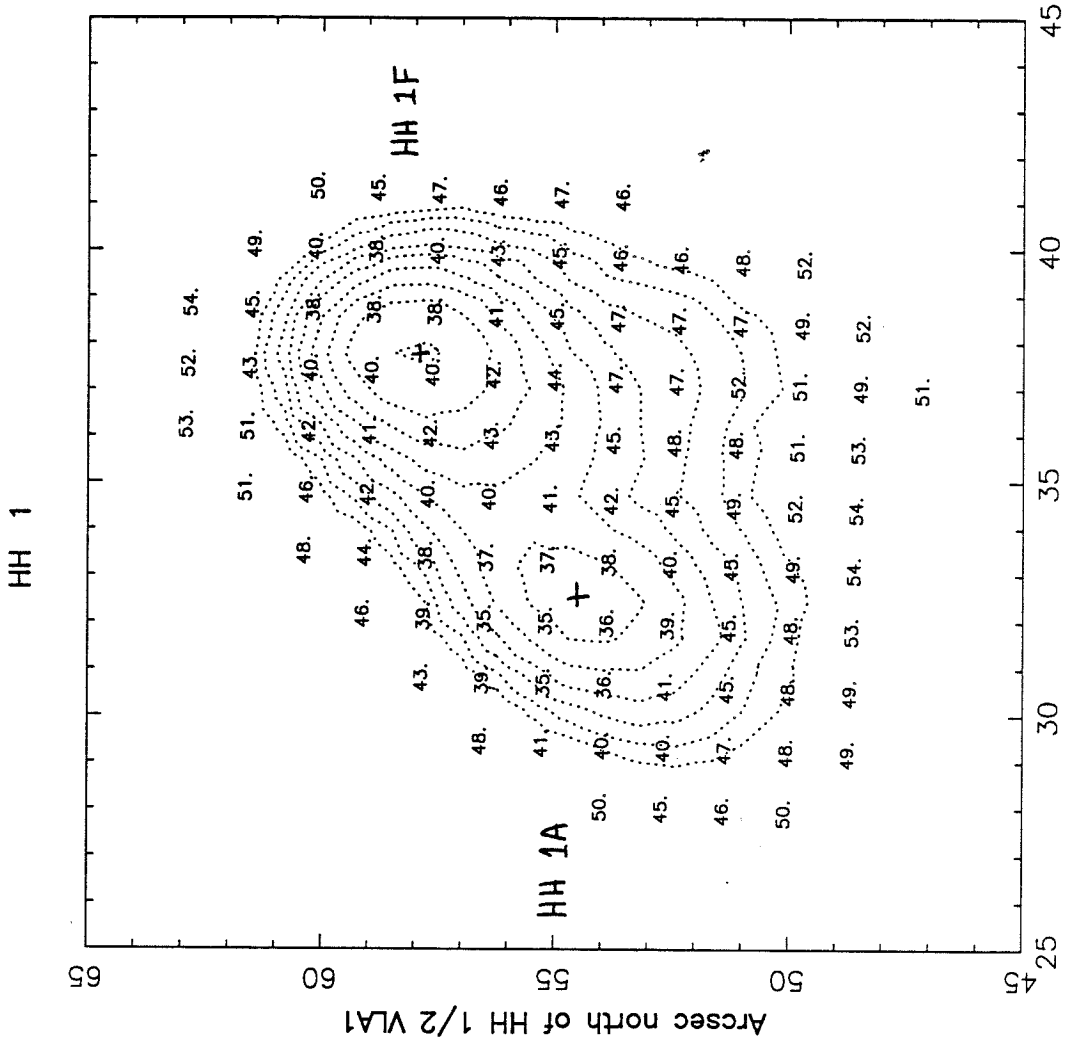
HH 1
HH 1F
HH 1A
Arcsec north of HH 1/2 VLA1
Arcsec west of HH 1/2 VLA1
65
60
55
50
45
25
30
35
40

Page 106
Figure 5
part 1

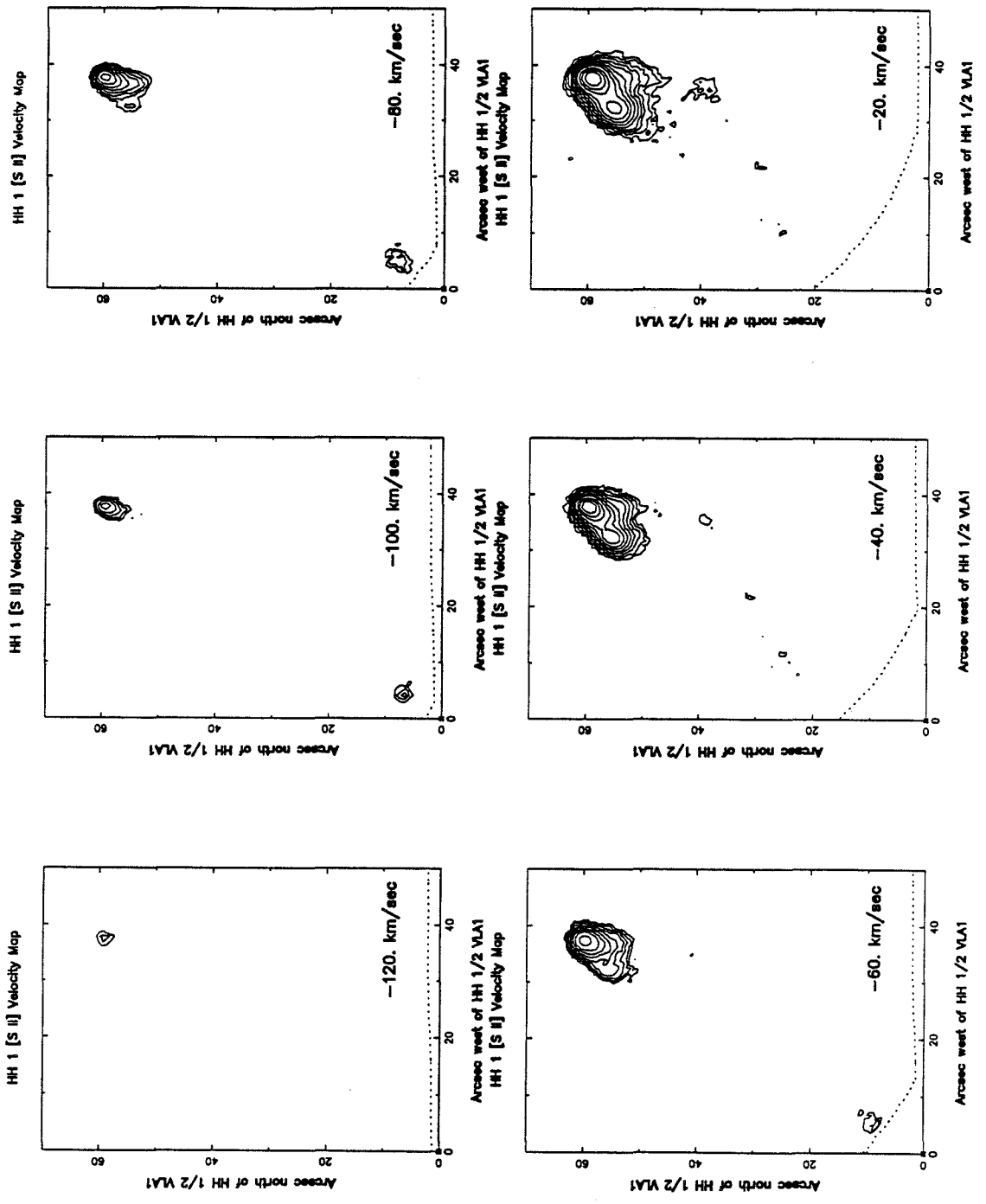

Page 107
Figure 5
part 2

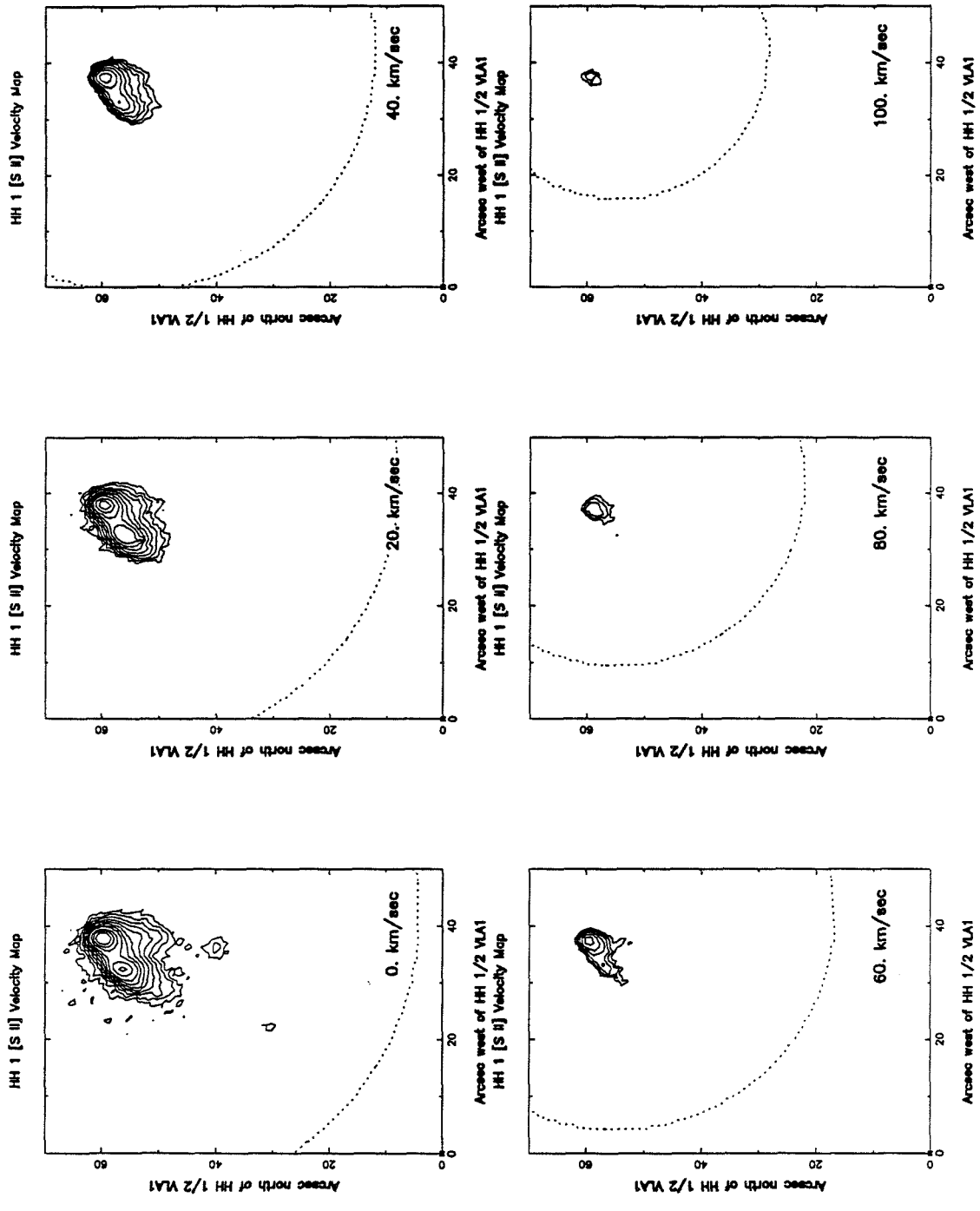

Page 108
Figure 6

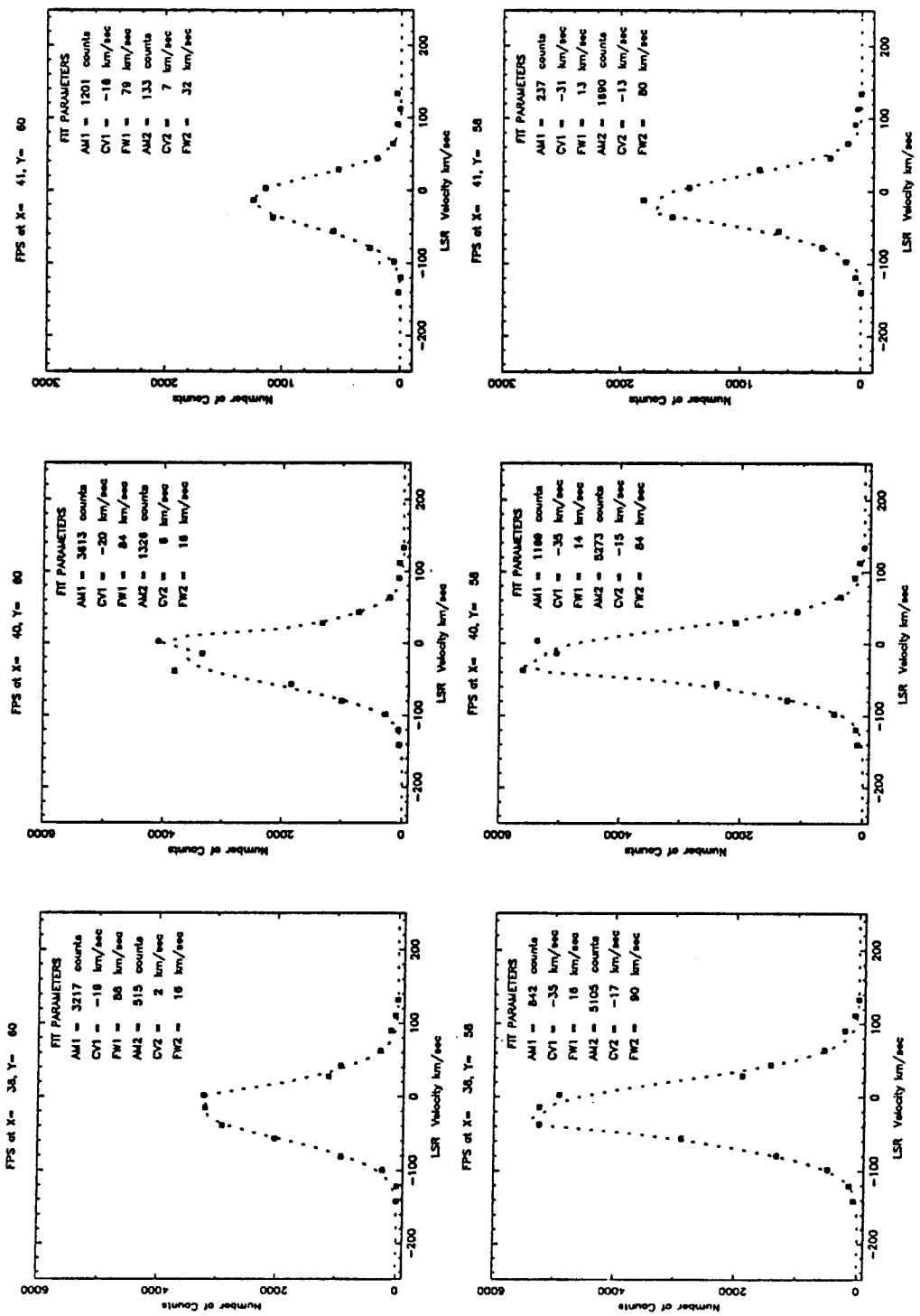

Figure 7

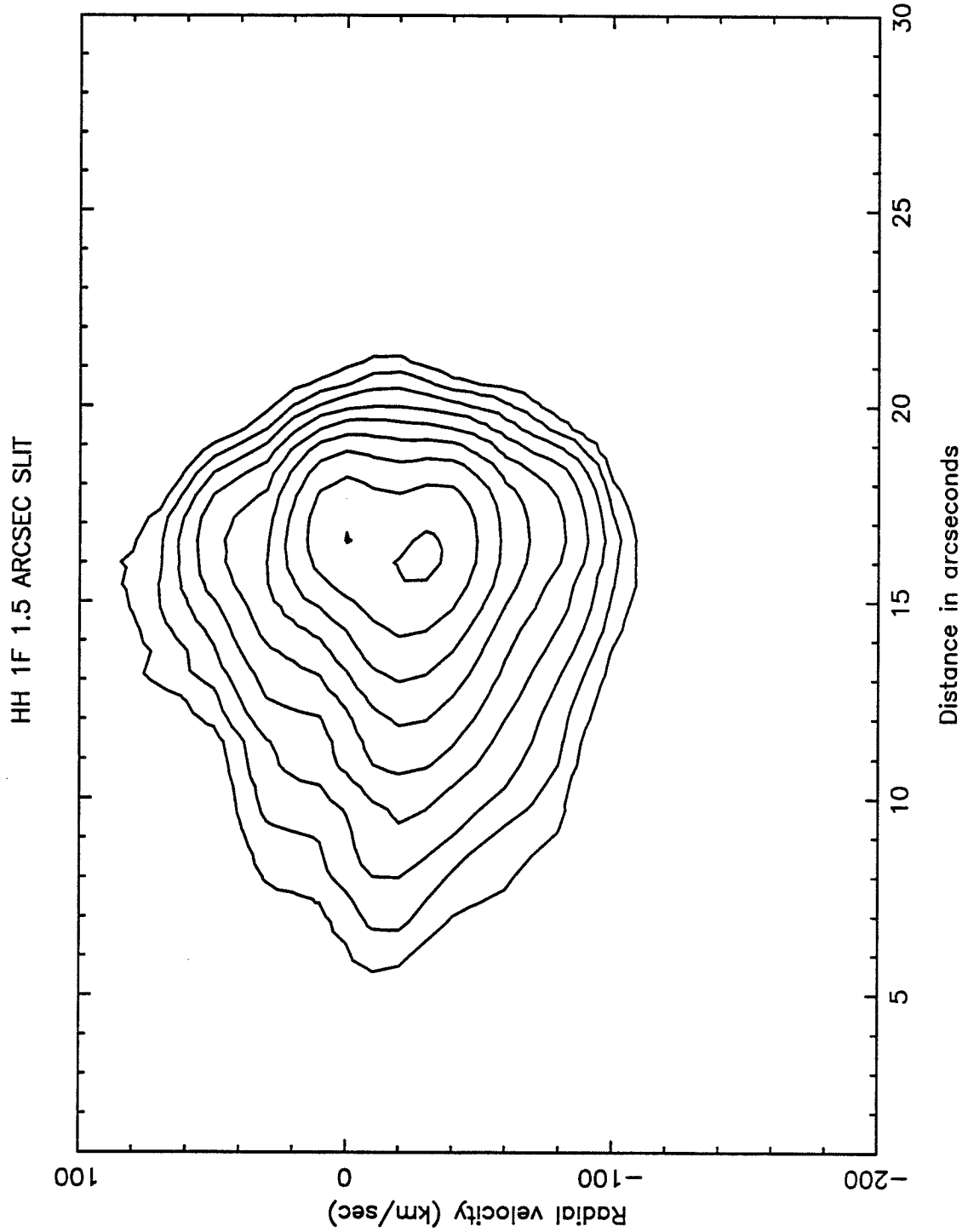
HH 1F 1.5 ARCSEC SLIT
Radial velocity (km/sec)
100
0
−100
−200
Distance in arcseconds
5
10
15
20
25
30

Figure 8a

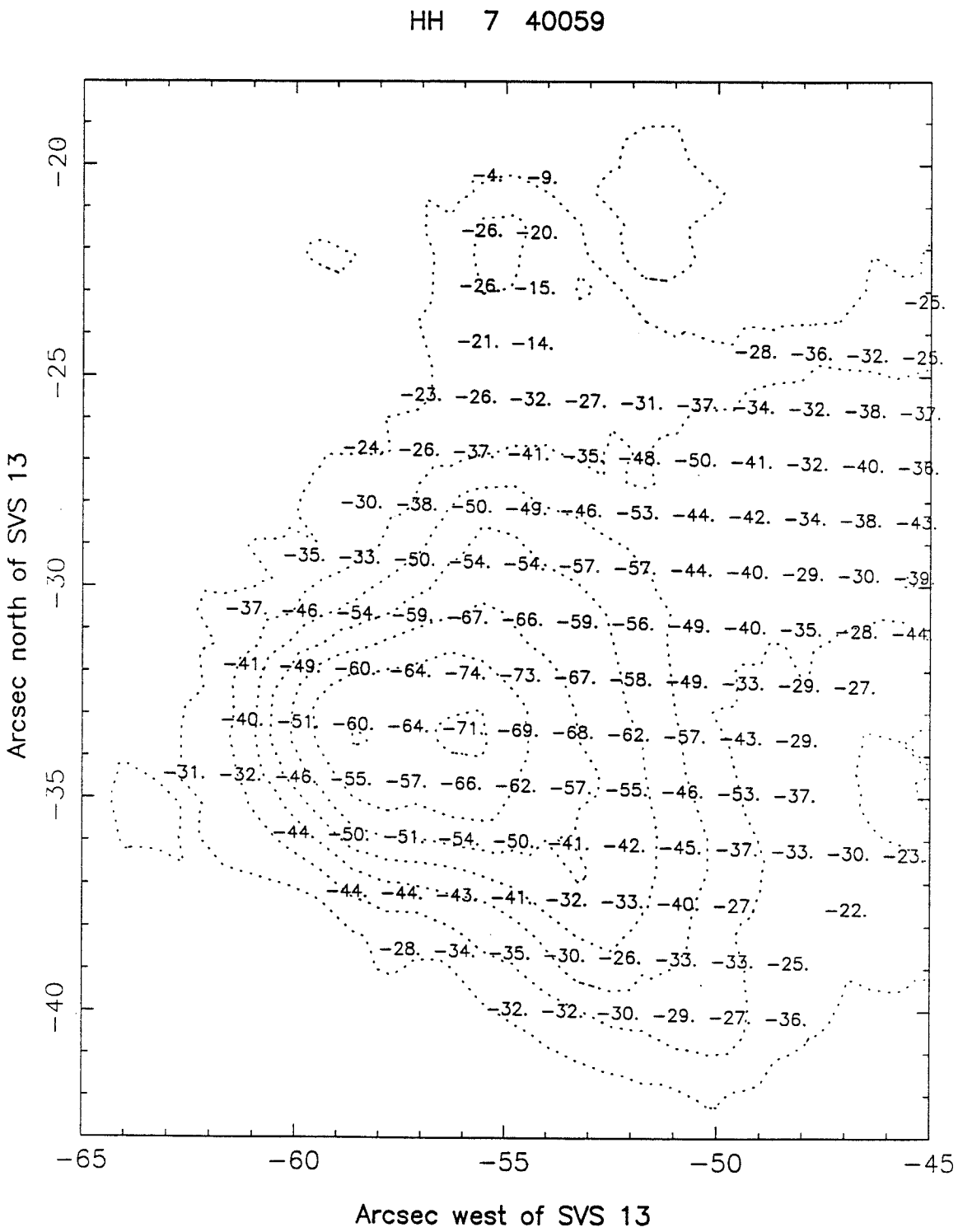
HH 7 40059
Arcsec north of SVS 13
Arcsec west of SVS 13
-20
-25
-30
-35
-40
-65
-60
-55
-50
-45
-4. -9.
-26. -20.
-26. -15.
-21. -14.
-25.
-28. -36. -32. -25.
-23. -26. -32. -27. -31. -37. -34. -32. -38. -37.
-24. -26. -37. -41. -35. -48. -50. -41. -32. -40. -38.
-30. -38. -50. -49. -46. -53. -44. -42. -34. -38. -43.
-35. -33. -50. -54. -54. -57. -57. -44. -40. -29. -30. -39.
-37. -46. -54. -59. -67. -66. -59. -56. -49. -40. -35. -28. -44.
-41. -49. -60. -64. -74. -73. -67. -58. -49. -33. -29. -27.
-40. -51. -60. -64. -71. -69. -68. -62. -57. -43. -29.
-31. -32. -46. -55. -57. -66. -62. -57. -55. -46. -53. -37.
-44. -50. -51. -54. -50. -41. -42. -45. -37. -33. -30. -23.
-44. -44. -43. -41. -32. -33. -40. -27. -22.
-28. -34. -35. -30. -26. -33. -33. -25.
-32. -32. -30. -29. -27. -36.

Figure 8b

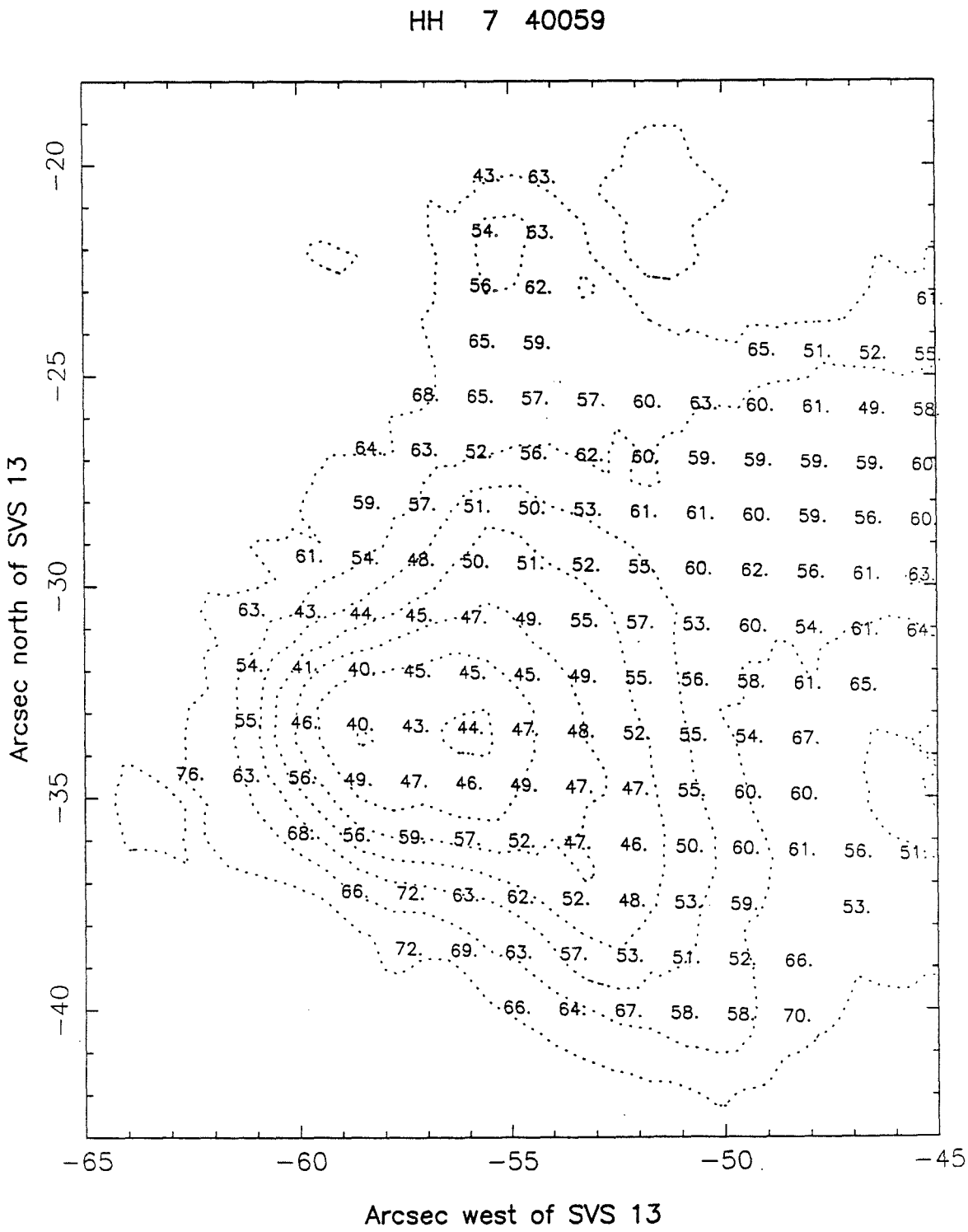
HH 7 40059
Arcsec north of SVS 13
Arcsec west of SVS 13
-20
-25
-30
-35
-40
-65
-60
-55
-50
-45

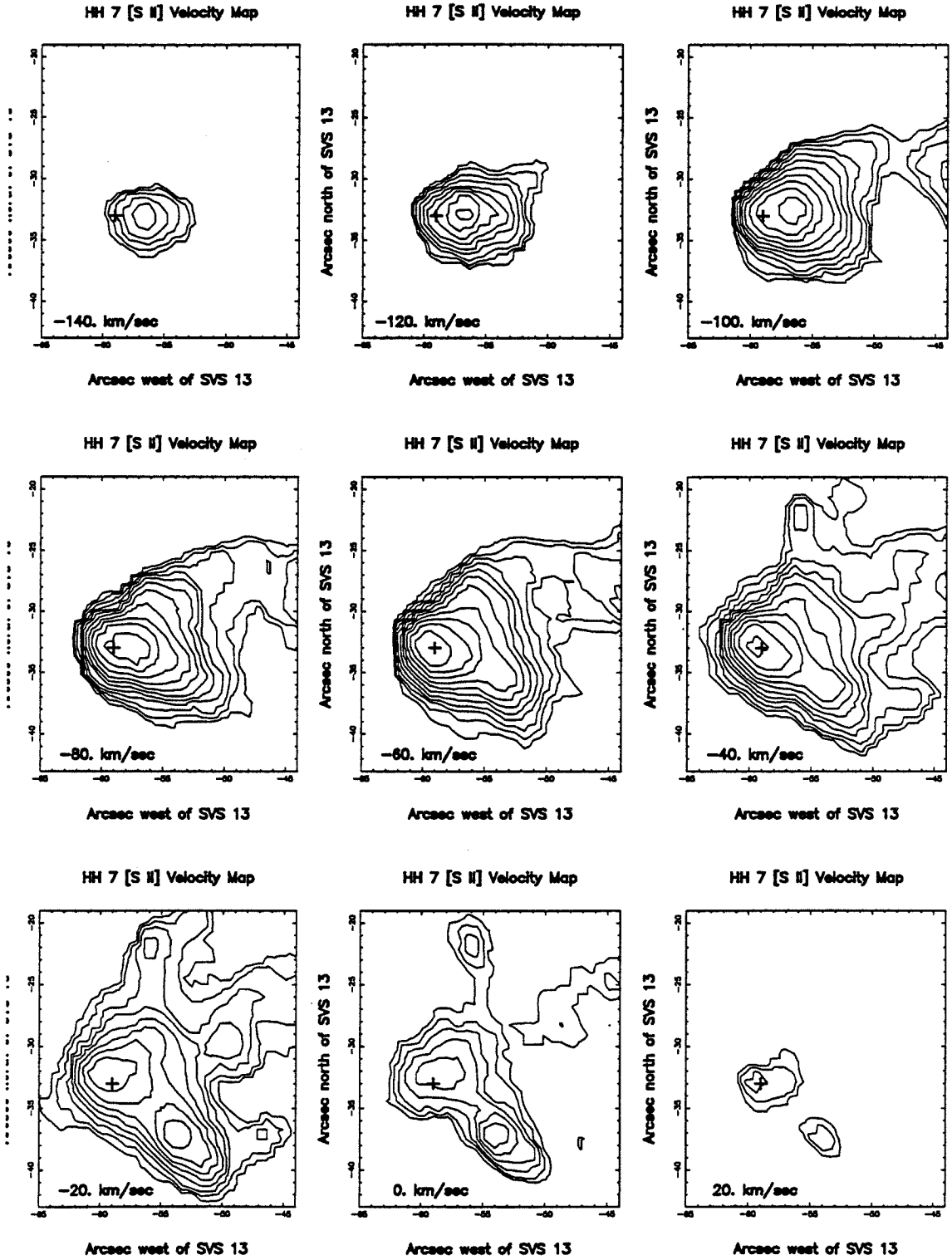
HH 7 [S II] Velocity Map
−140. km/sec
HH 7 [S II] Velocity Map
−120. km/sec
HH 7 [S II] Velocity Map
−100. km/sec
HH 7 [S II] Velocity Map
−80. km/sec
HH 7 [S II] Velocity Map
−60. km/sec
HH 7 [S II] Velocity Map
−40. km/sec
HH 7 [S II] Velocity Map
−20. km/sec
HH 7 [S II] Velocity Map
0. km/sec
HH 7 [S II] Velocity Map
20. km/sec
Arcsec north of SVS 13
Arcsec west of SVS 13

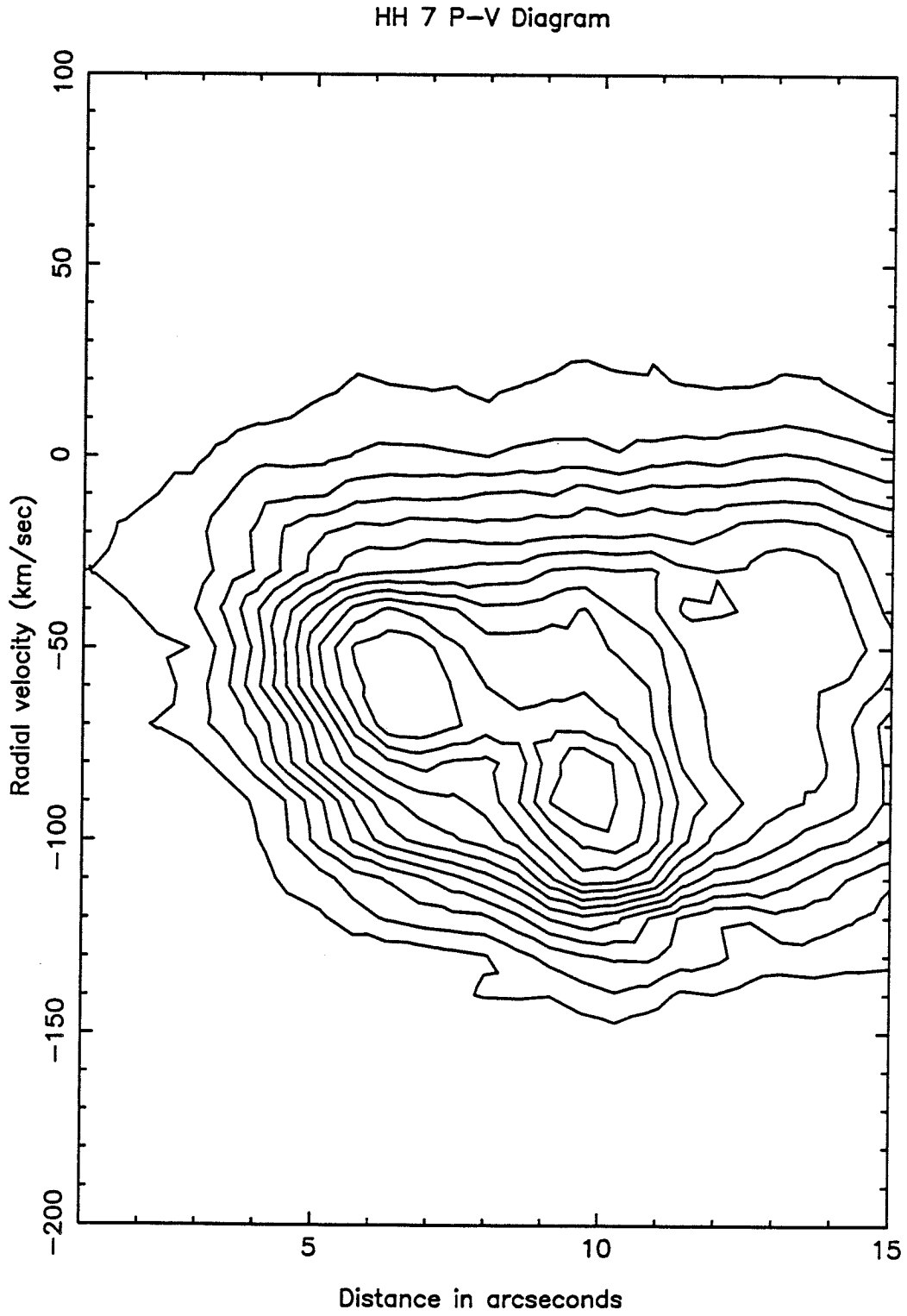
HH 7 P–V Diagram
Radial velocity (km/sec)
100
50
0
−50
−100
−150
−200
5
10
15
Distance in arcseconds

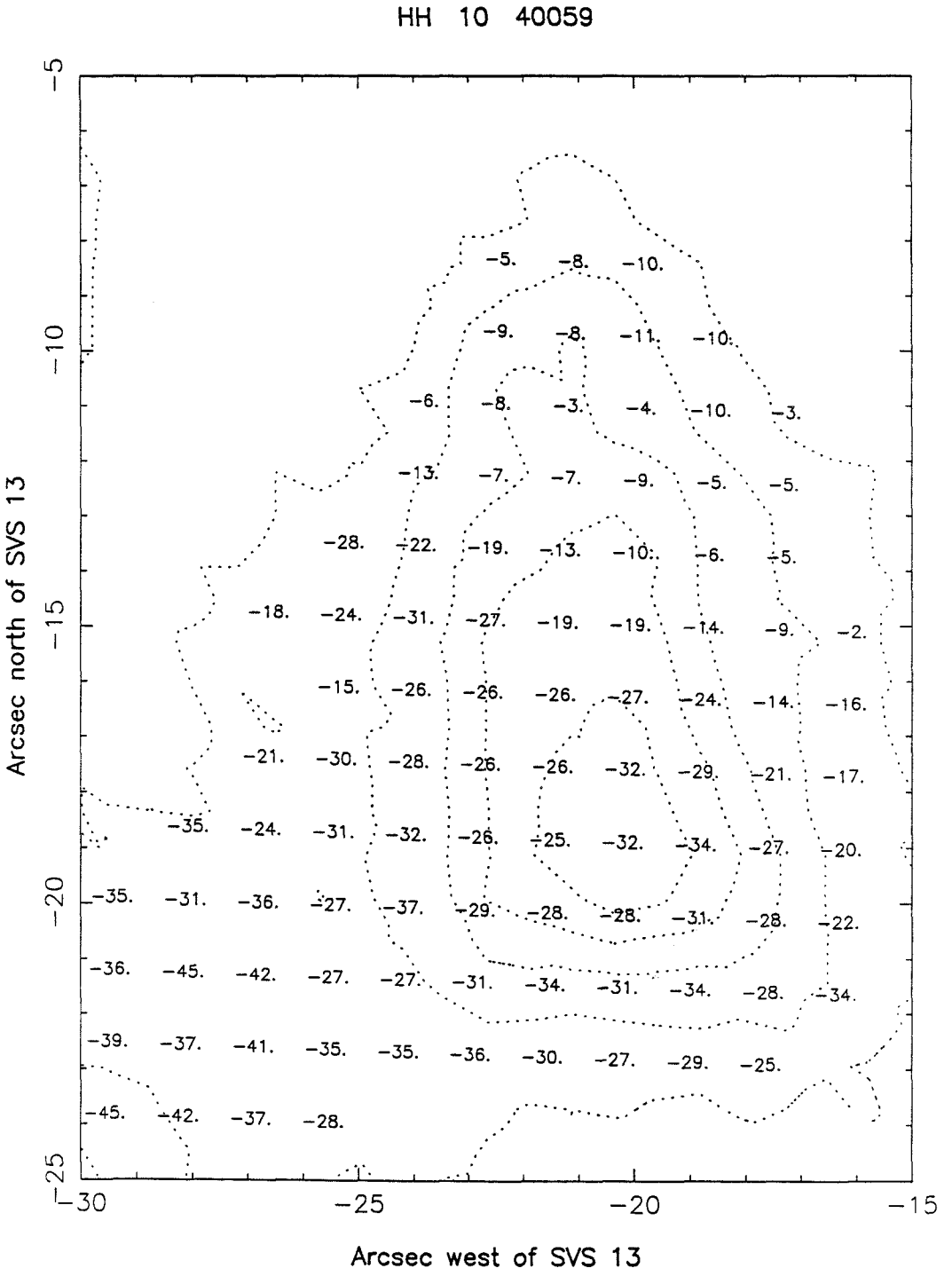
HH 10 40059
Arcsec north of SVS 13
Arcsec west of SVS 13
-5
-10
-15
-20
-25
-30
-25
-20
-15
-5. -8. -10.
-9. -8. -11. -10.
-6. -8. -3. -4. -10. -3.
-13. -7. -7. -9. -5. -5.
-28. -22. -19. -13. -10. -6. -5.
-18. -24. -31. -27. -19. -19. -14. -9. -2.
-15. -26. -26. -26. -27. -24. -14. -16.
-21. -30. -28. -26. -26. -32. -29. -21. -17.
-35. -24. -31. -32. -26. -25. -32. -34. -27. -20.
-35. -31. -36. -27. -37. -29. -28. -28. -31. -28. -22.
-36. -45. -42. -27. -27. -31. -34. -31. -34. -28. -34.
-39. -37. -41. -35. -35. -36. -30. -27. -29. -25.
-45. -42. -37. -28.

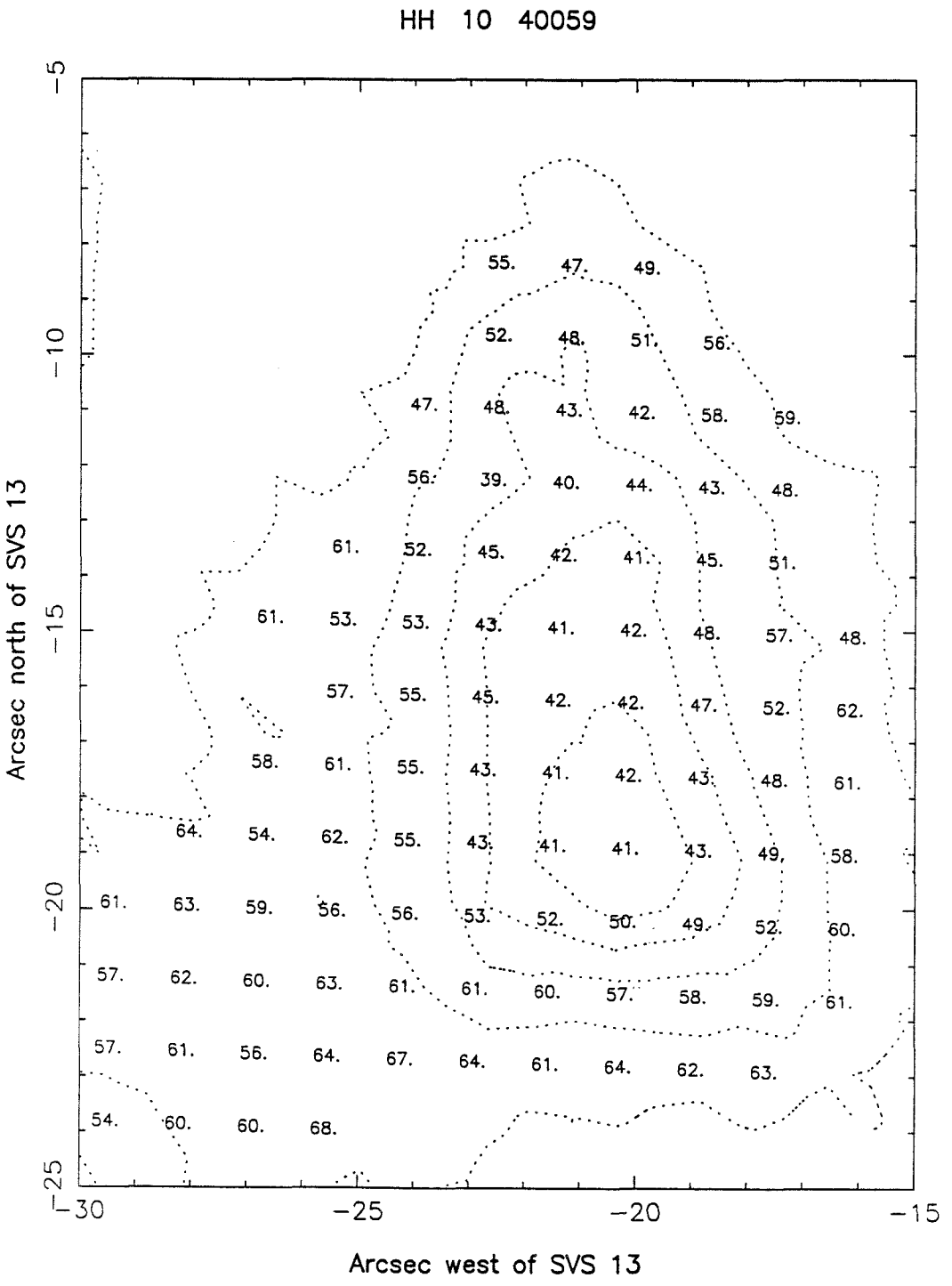
HH 10 40059
Arcsec north of SVS 13
Arcsec west of SVS 13
−5
−10
−15
−20
−25
−30
−25
−20
−15
55. 47. 49.
52. 48. 51. 56.
47. 48. 43. 42. 58. 59.
56. 39. 40. 44. 43. 48.
61. 52. 45. 42. 41. 45. 51.
61. 53. 53. 43. 41. 42. 48. 57. 48.
57. 55. 45. 42. 42. 47. 52. 62.
58. 61. 55. 43. 41. 42. 43. 48. 61.
64. 54. 62. 55. 43. 41. 41. 43. 49. 58.
61. 63. 59. 56. 56. 53. 52. 50. 49. 52. 60.
57. 62. 60. 63. 61. 61. 60. 57. 58. 59. 61.
57. 61. 56. 64. 67. 64. 61. 64. 62. 63.
54. 60. 60. 68.

Figure 12

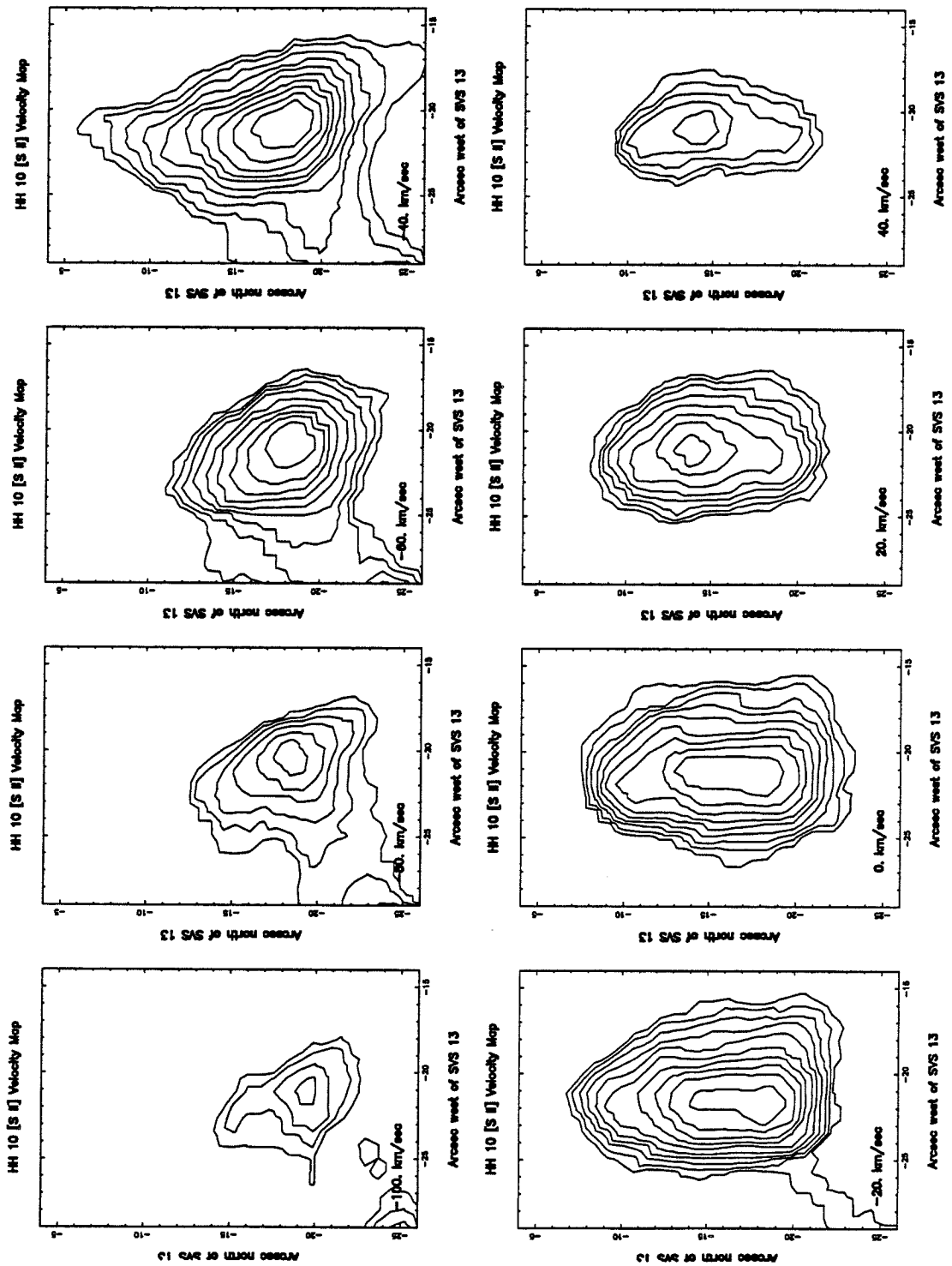
HH 10 [S II] Velocity Map
Arcsec north of SVS 13
Arcsec west of SVS 13
40. km/sec
20. km/sec
0. km/sec
-20. km/sec
-40. km/sec
-60. km/sec
-100. km/sec

Figure 13a

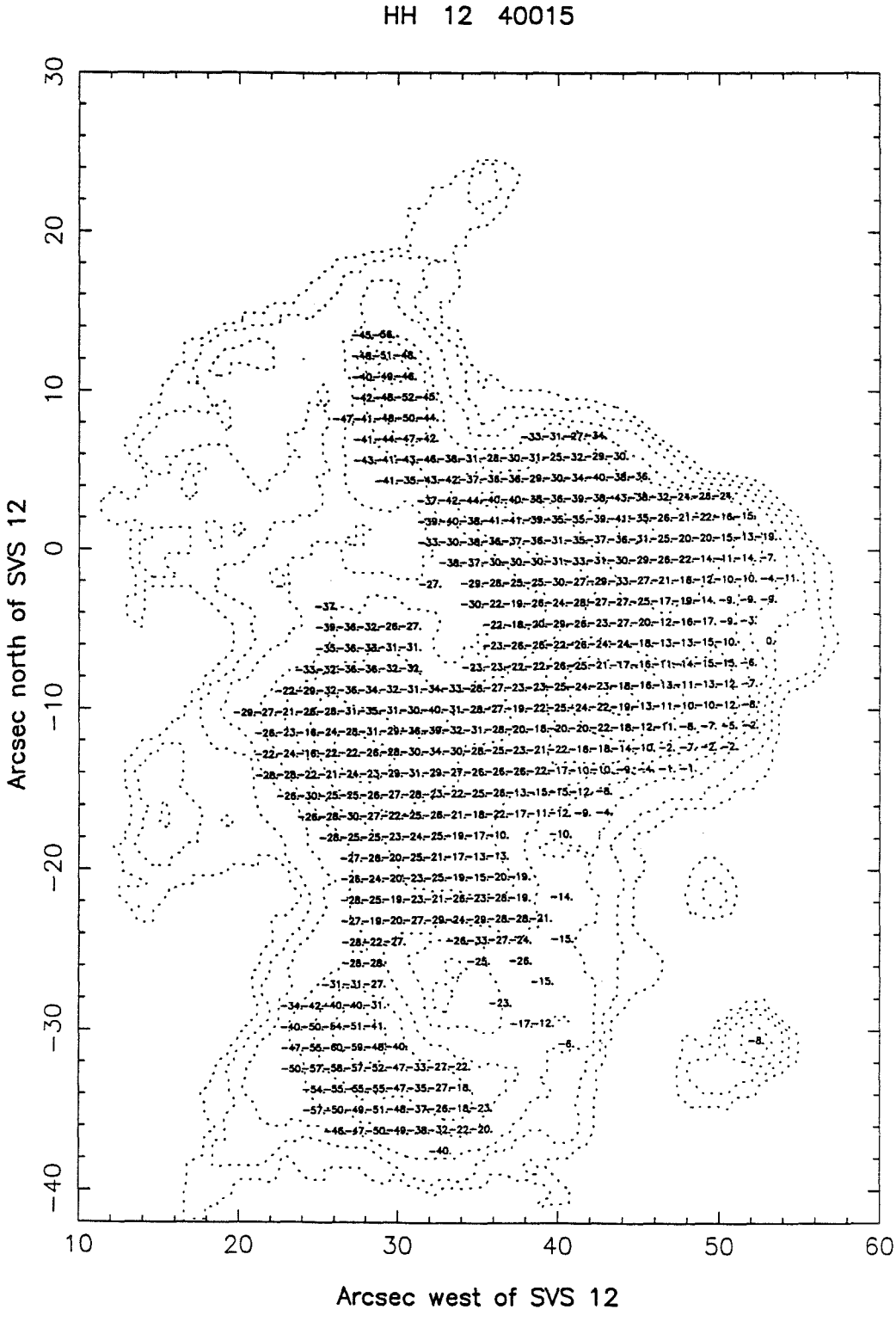
HH 12 40015
Arcsec north of SVS 12
Arcsec west of SVS 12
30
20
10
0
−10
−20
−30
−40
10
20
30
40
50
60

Figure 136

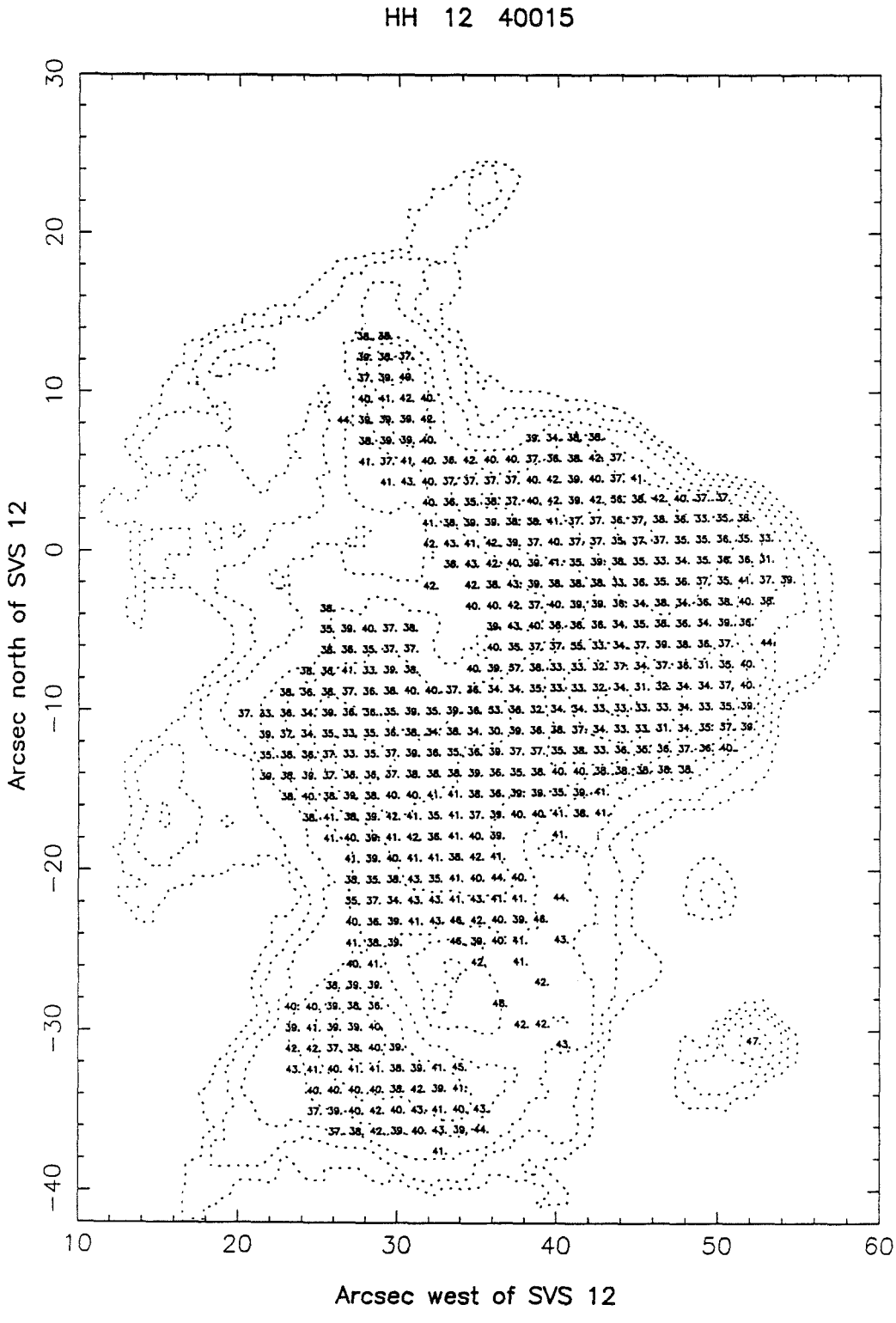
HH 12 40015
Arcsec north of SVS 12
Arcsec west of SVS 12
30
20
10
0
-10
-20
-30
-40
10
20
30
40
50
60

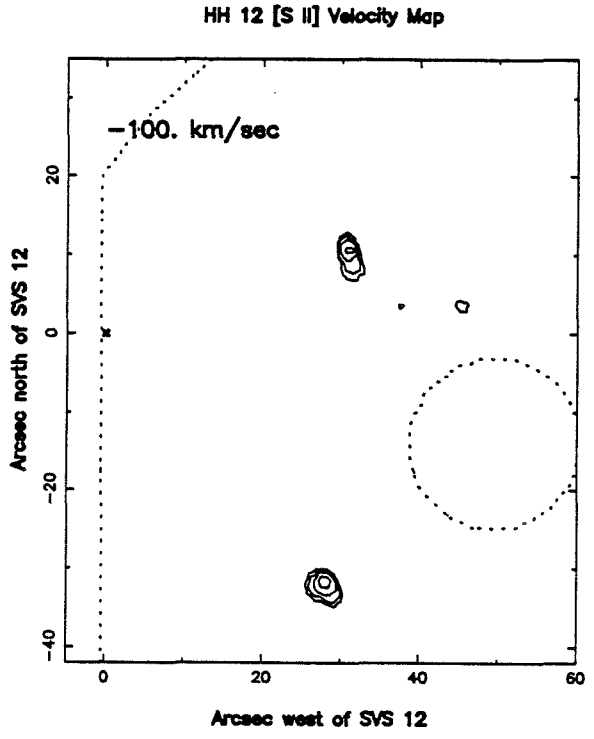
HH 12 [S II] Velocity Map
−100. km/sec
Arcsec north of SVS 12
Arcsec west of SVS 12
20
0
−20
−40
0
20
40
60

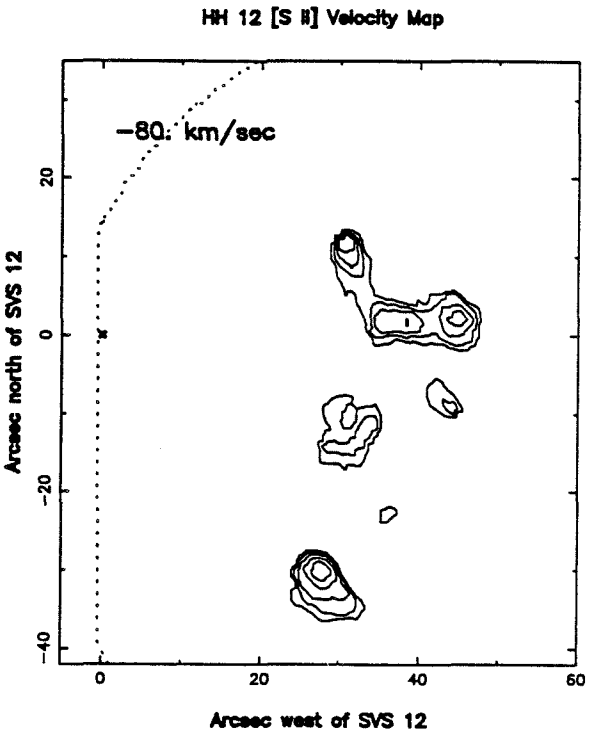
HH 12 [S II] Velocity Map
−80. km/sec
Arcsec north of SVS 12
Arcsec west of SVS 12
20
0
−20
−40
0
20
40
60

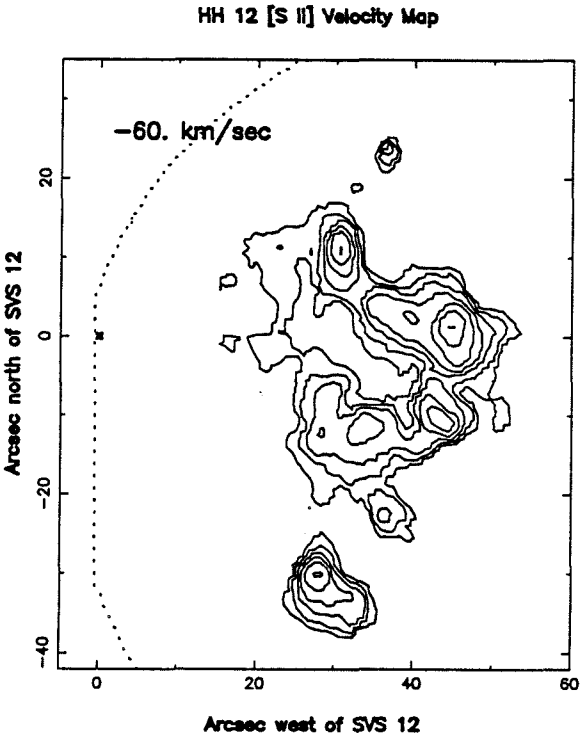
HH 12 [S II] Velocity Map
−60. km/sec
Arcsec north of SVS 12
Arcsec west of SVS 12
20
0
−20
−40
0
20
40
60

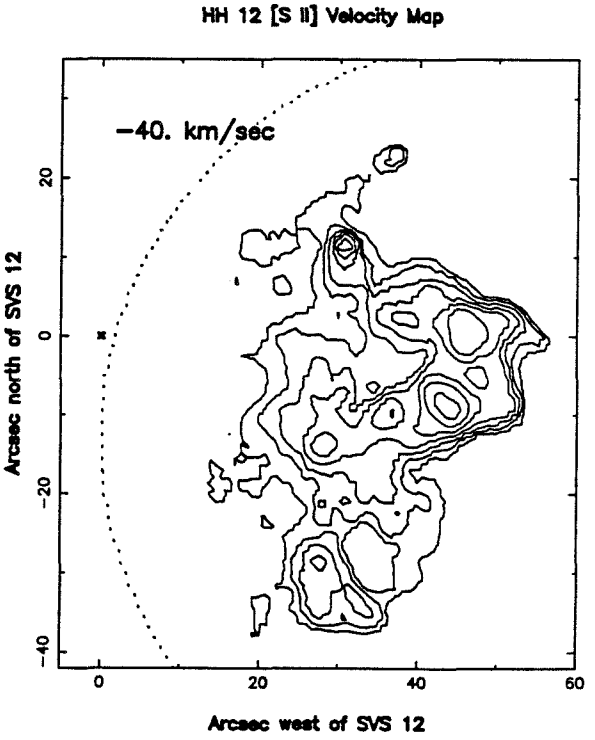
HH 12 [S II] Velocity Map
−40. km/sec
Arcsec north of SVS 12
Arcsec west of SVS 12
20
0
−20
−40
0
20
40
60

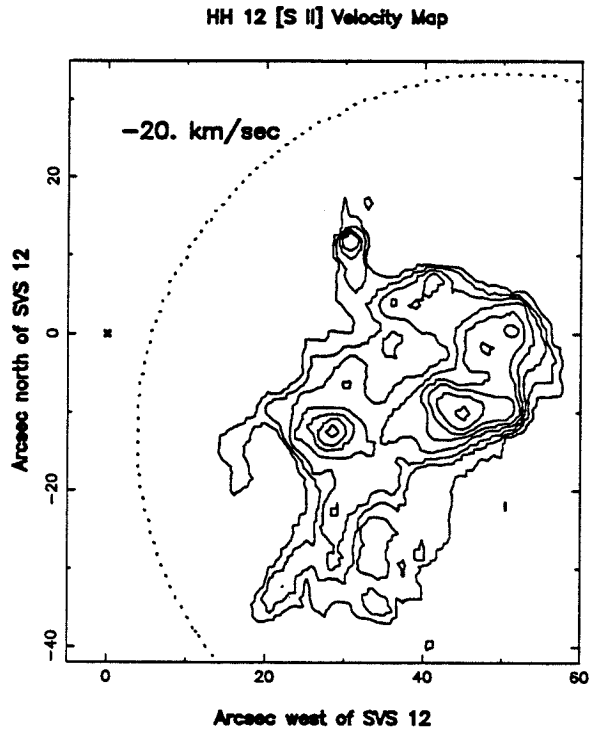
HH 12 [S II] Velocity Map
−20. km/sec
Arcsec north of SVS 12
Arcsec west of SVS 12
20
0
−20
−40
0
20
40
60

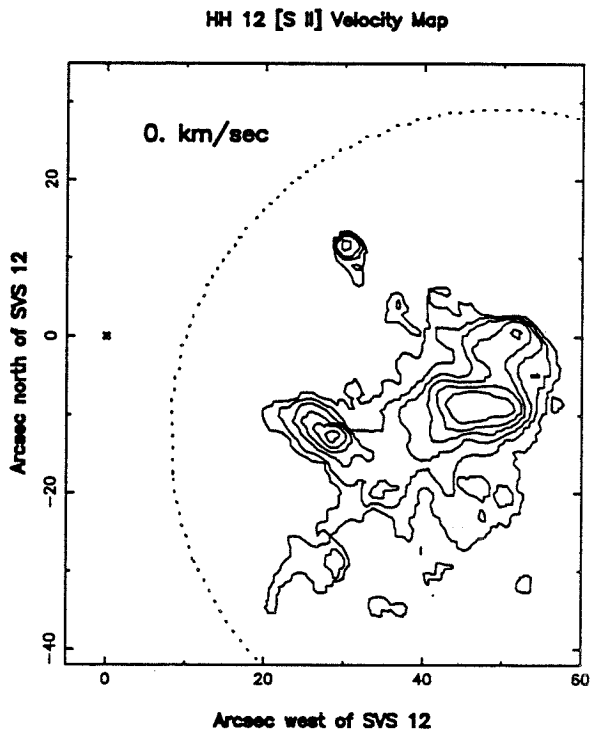
HH 12 [S II] Velocity Map
0. km/sec
Arcsec north of SVS 12
Arcsec west of SVS 12
20
0
−20
−40
0
20
40
60

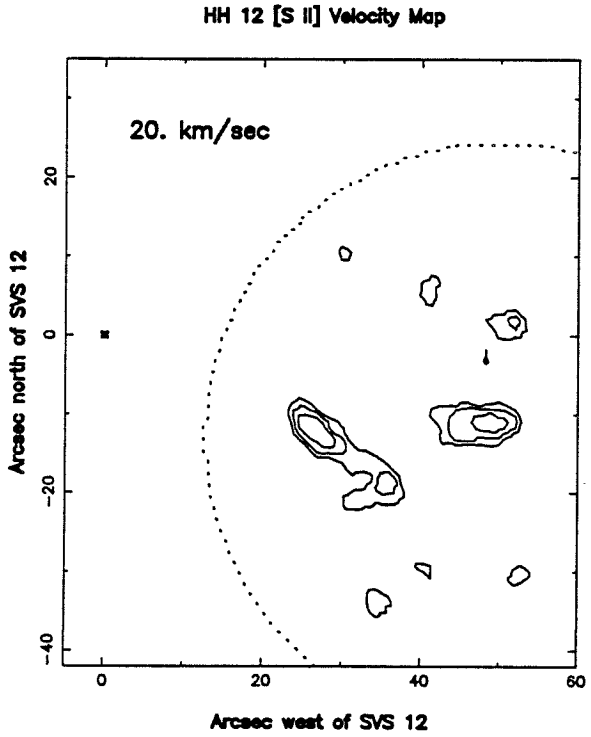
HH 12 [S II] Velocity Map
20. km/sec
Arcsec north of SVS 12
Arcsec west of SVS 12
20
0
−20
−40
0
20
40
60

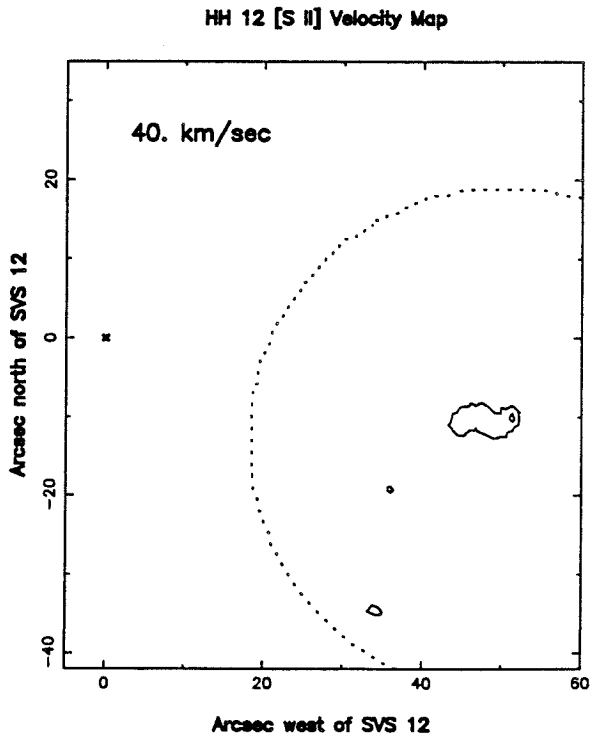
HH 12 [S II] Velocity Map
40. km/sec
Arcsec north of SVS 12
Arcsec west of SVS 12
20
0
−20
−40
0
20
40
60

Figure 15

a.

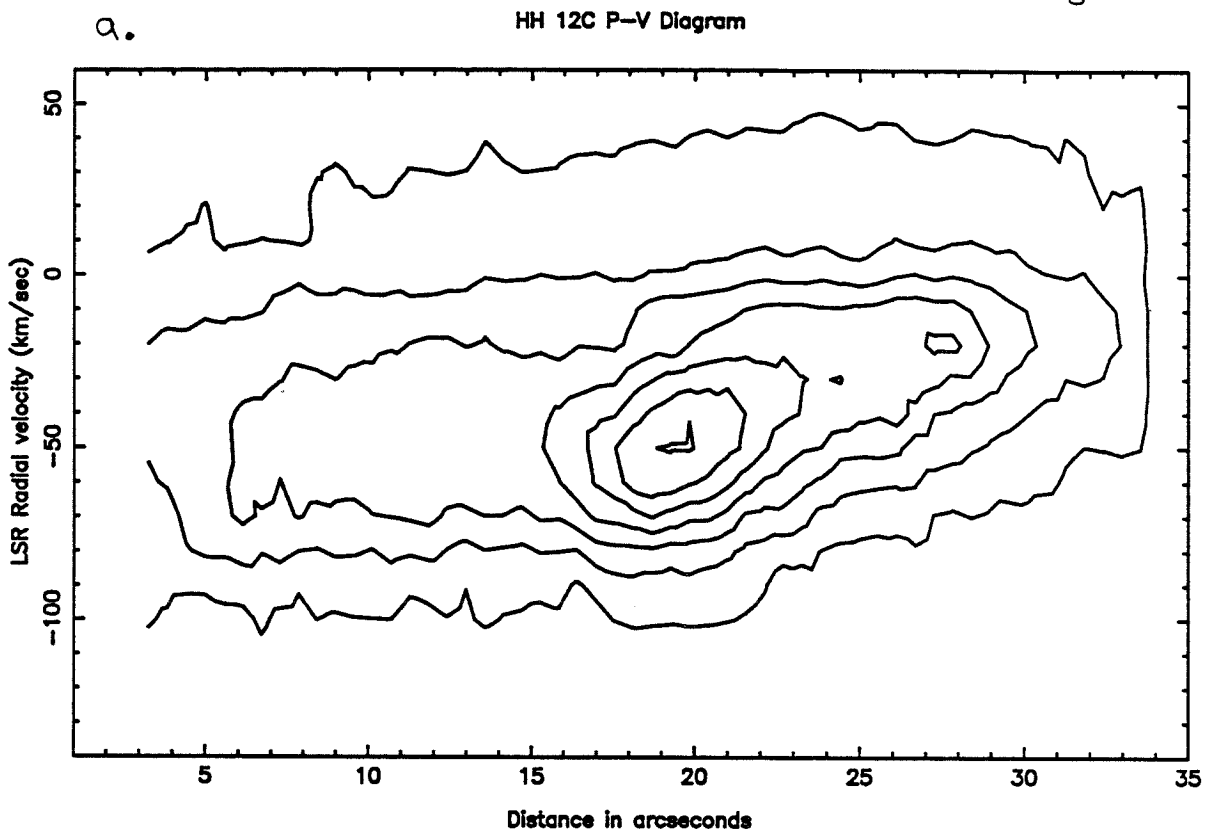
HH 12C P–V Diagram
LSR Radial velocity (km/sec)
50
0
−50
−100
5
10
15
20
25
30
35
Distance in arcseconds

b.

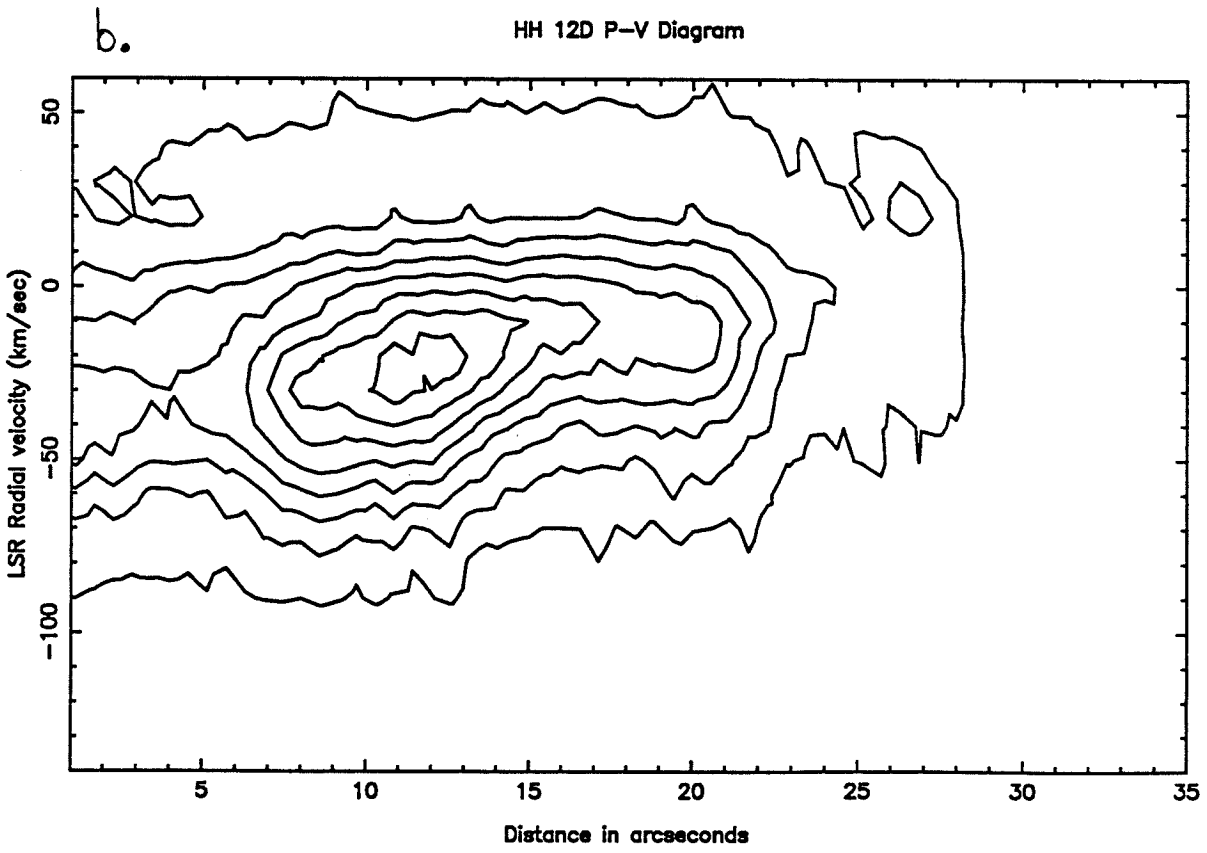
HH 12D P–V Diagram
LSR Radial velocity (km/sec)
50
0
−50
−100
5
10
15
20
25
30
35
Distance in arcseconds

Chapter IV.

Circumstellar Molecular Gas of the HH 34 and HH 111 Exciting Stars

Abstract:

The HH 34 and HH 111 exciting stars, two pre-main sequence objects which are the sources of highly collimated optical jets, have been observed in the J= 1-0 transition of ^{13}CO and in the millimeter continuum using the Owens Valley Radio Observatory Millimeter Interferometer. The high resolution aperture synthesis maps reveal dense molecular gas concentrations at the positions of both stars. The morphology and kinematics of the line emission suggest that the molecular gas is distributed in circumstellar disks, each about 2000 AU in diameter, elongated perpendicular to each system's outflow axis. Independent mass determinations based on the dust continuum and molecular line fluxes indicate for HH 34, a disk mass of 0.2 $M_\odot$; and for HH 111, a disk mass of $0.4M_\odot$. The inferred circumstellar disks of these two jet sources are significantly more massive than those found associated with T Tauri stars. The observed millimeter line and continuum fluxes *alone* imply that these objects may possess the most massive disks currently known in association with low mass pre-main sequence stars. The fact that *both* of these jet sources possess such large amounts of circumstellar material suggests that the collimation, energetics, and evolution of bipolar outflows are strongly influenced by circumstellar disks.

I. Introduction

As understanding of star formation and early stellar evolution has grown over the past two decades, it has become clear that young pre-main sequence stars can possess significant amounts of circumstellar material. The presence of this material is almost certainly a by-product of the star formation process, for main sequence stars generally do not possess significant amounts of circumstellar material. The nature of this material, particularly its distribution, composition, total mass, and time evolution, is of great interest because it is within a young star's circumstellar material that planetary systems are believed to form. The coplanar orbits of our planetary system, combined with with theoretical insights into the gravitational collapse of rotating interstellar clouds, lead to the expectation that the circumstellar material of young stars will be distributed in flattened disks (*cf.* Shu, Adams, and Lizano 1987).

There is abundant indirect evidence for circumstellar disks in association with solar-type pre-main sequence (PMS) stars. Excess far-infrared continuum emission, understood as thermal radiation from warm dust within a disk 10-100 AU in size, has been detected by IRAS (Beichman *et al.* 1986; Myers *et al.* 1987). Optical forbidden emission lines, formed in the outflowing stream of PMS stellar winds, show only blueshifted components; the missing redshifted forbidden emission is thought to be occulted by a circumstellar disk (Edwards *et al.* 1987). Direct detection of circumstellar disks has been accomplished using infrared speckle imaging (Beckwith *et al.* 1984). Millimeter interferometry has identified disk structures associated with HL Tauri (Sargent and Beckwith 1987), DG Tauri (Sargent and Beckwith 1988), T Tauri (Weintraub, Masson, and Zuckerman 1989), and L1551 IRS5 (Sargent *et al.* 1988). The HL Tau result is especially noteworthy, for it demonstrated that

the disk kinematics were in accord with Keplerian rotation. Single-dish continuum observations at wavelengths near 1 millimeter have recently been conducted with goal of determining disk masses for a larger number of objects (Weintraub, Sandell, and Duncan 1989; Beckwith et al. 1990; and Adams, Emerson, and Fuller 1990).

Most investigations of the circumstellar matter of young stellar objects (YSO's) have concentrated on T Tauri stars. However, there is another viable strategy: observing more deeply embedded infrared sources. T Tauri stars (as a class) are by definition optically visible objects. Since molecular gas column density correlates well with the amount of visible extinction produced by dust, it is reasonable to expect that *some* of the more optically obscured sources may possess larger masses of circumstellar gas. The observational challenge is to find embedded sources obscured by *circumstellar* dust, rather than the bulk *interstellar* dust within a molecular cloud.

A class of embedded young stellar objects that fit this criteria is the Herbig-Haro object exciting stars. Herbig-Haro objects (*cf.* Schwartz 1983) are optically visible emission nebulae, now generally agreed to be luminous shock waves formed where a supersonic, often collimated stellar wind impacts ambient cloud material. The 'HH' exciting stars are the sources of these stellar winds. The existence of large extinction gradients near these sources is implied by the fact that the HH objects themselves are optically visible, while their exciting stars are usually optically obscured. Furthermore, bright far-infrared emission is associated with several HH exciting stars (Cohen and Schwartz 1987; Cohen *et al.* 1984,1985). This observational evidence suggests that HH exciting stars may generally possess substantial amounts of circumstellar material. Theoretical work by Konigl (1982) and Boss (1987) has shown that the bipolar outflows responsible for HH objects may be col-

limated by circumstellar disks at the outflow sources.

The most collimated young stellar outflows known are those associated with optical jets and Herbig-Haro objects. The first examples of these flows were recognized by Mundt and Fried (1983) using narrowband CCD imaging in Hα and [S II] 6717,6731 Å emission lines; many examples are now known (Mundt, Brugel, and Buhrke 1987; Reipurth 1989). If disks do play a role in outflow collimation, then these highly collimated flows are a natural place to look for them.

Overview of the regions studied

One of the most striking examples of an optical emission line jet is the case of HH 34, whose discovery was reported independently by Mundt (1986) and Reipurth *et al.* (1986). The observers found a highly collimated jet emerging from an optically faint star and pointing directly toward HH 34, 110″ to the south. It was quickly realized that HH 34 itself is the 'working surface' of this jet, a bow shock formed where the jet flow impacts the ambient medium. To the north of the HH 34 jet source, Buhrke, Mundt, and Ray (1988) discovered a second, redshifted bow shock that mirrors the southern bow shock in location and morphology. However, no northern jet has been found (see Chapter 2).

The most extensive study of the HH 34 exciting star (the source of the jet) has been done by Reipurth *et al.* (1986). They report R = 19.4, K = 12.3, and the presence of strong emission lines (Hα, Ca II, [S II], [O I], [Fe II]) in the spectrum. The stellar spectral type is estimated to fall in the range between F and K and the visual extinction $A_V \approx 5$ mag. A definite near-infrared excess is reported. Scarrott (1988) has found that scattered starlight near the exciting star is strongly

polarized (21% in red light), with polarization vectors are oriented perpendicular to the jet. The HH 34 star is not included in the IRAS Point Source Catalog. However, Cohen and Schwartz (1987) identified a suitably located bright IRAS source in co-added survey data; the estimated luminosity is 45 $L_{\odot}$. Overall, the optical and infrared properties of the HH 34 exciting star resemble those of extremely active T Tauri stars, and suggest the presence of a circumstellar disk. The only published millimeter wavelength observations of this object are those of Reipurth *et al.* (1986), but their single-dish observations lacked the spatial resolution necessary to reveal true circumstellar structure. However, they did find an unresolved CO column density enhancement and CS emission at the position of the HH 34 star.

The HH 111 outflow and optical jet were discovered by Reipurth (1989) during a deep survey for Herbig-Haro objects in the Orion L1617 molecular cloud. In this system a highly collimated jet extends from an optically invisible infrared source toward a small condensed bow shock 140″ to the west. To the east of the source no counter-jet is seen; however, there are two bow shocks 200″ from the source along the flow axis. Reipurth argues that the multiple bow shocks require an unsteady, perhaps episodic outflow. A conical reflection nebula is present at the base of the optical jet, suggesting that obscuring material is anisotropically distributed about the star in a manner consistent with the presence of a circumstellar disk. The HH 111 exciting star very likely corresponds to the IRAS source 05491+0247, for which a counterpart is known only at 2 μm (K magnitude = 12.8; Reipurth 1989). Reipurth estimates that the total visual extinction toward the star $A_V \geq 30$ mag, and that the total source luminosity is about 25 $L_{\odot}$.

II. Observations

The Owens Valley Radio Observatory Millimeter Interferometer was used to observe the HH 34 and HH 111 exciting stars in the 110.2 GHz J= 1-0 line of ^{13}CO. Eight configurations of the three 10.4 m telescopes, with unprojected baselines ranging from 15 to 170 m, were used to observe a field centered on the HH 34 exciting star during April–June 1988 and February–March 1989. The resulting maps cover a field 60″ in diameter with a synthesized beam of 4.0″ x 3.2″ at PA 2°. Five telescope configurations, with unprojected baselines ranging from 15 to 80 m, were used to observe a field centered on the HH 111 exciting star during December 1989 - May 1990, yielding a synthesized beam of 8.5″ x 5.7″ at PA 85°. Both sources were observed in the lower sideband with two 32 channel filterbanks that sampled the spectrum at 50 kHz and 1 MHz (0.14 km s^{-1} and 2.7 km s^{-1}) intervals. In addition, a 375 MHz wide channel allowed measurements of the 2.7 mm continuum emission. The SIS receivers (Woody, Miller, and Wengler 1985) provided a typical system noise temperature of

A source 'track' was collected each time an object was observed in a particular telescope configuration. The tracks were typically 7-9 hours in duration for these low declination sources. Most of the observations carried out during a track were of the program source; however, a phase calibrator was observed at 30 minute intervals. In addition, amplitude calibration and filterbank (passband) calibration sources were observed for 30 minutes of each track. The quasar 0420-014, an unresolved millimeter continuum source, was used as the phase calibrator. Long-period stochastic variations in the observed phase of the program source are assumed to follow those of the nearby quasar. Subtracting the observed variation in calibrator phase from the phase of the program source allows the effects of changing atmo-

spheric/ionospheric propagation to be accounted for. A bright continuum source, usually 3C273, was used to solve for the relative gains and phase offsets of the individual filterbank channels. Uranus and Mars (if available) were used as amplitude calibration sources. The measured peak variation in amplitude of 0420-014 was 15% over each track, implying a similar fractional uncertainty in the derived fluxes for the objects.

After performing the phase calibration, filterbank (passband) calibration, and amplitude calibration, the visibility data was loaded into the NRAO AIPS software package using the OVRO program MMGOD. CLEANed maps using natural uv weighting were made of all 65 available spectral channels for both HH 34 and HH 111. The finals maps showed RMS noise levels of of 200, 60, and 3 mJy per beam in the 50 kHz, 1 MHz, and 375 MHz channels respectively.

III. Results

a) Millimeter Continuum Emission, HH 34 Exciting Star

A map of the 2.7 mm continuum emission associated with the HH 34 exciting star is shown in Figure 1. An unresolved core of emission is present at position $\alpha = 05^h33^m03.7^s$, δ = -06°28′50.8″. The optical position of the star (K. Strom *et al.* 1986) is $\leq 1''$ from this position. Low-intensity spatially resolved continuum emission is also evident surrounding the star, with a weak extension 6″ to the north. The total continuum flux density detected is 60 $\pm$ 10 mJy, with the unresolved core contributing 32 $\pm$ 3 mJy. The nature of the continuum emission can be ascertained

if the spectral index is known. The 1.3 mm continuum flux density of the HH 34 star has been measured using a bolometer at the Caltech Submillimeter Observatory (A. Sargent, personal communication); a value of 479 $\pm$ 28 mJy was obtained with a 30″ beam. The two continuum measurements imply a frequency spectral index of 3.0. Free-free emission cannot produce a spectrum with this spectral index. Thermal dust emission has been identified in the millimeter continuum spectrum of many pre-main sequence stars (Sargent & Beckwith 1987; Beckwith *et al.* 1990), and is consistent with the derived millimeter spectral index of the HH 34 star. This interpretation is also consistent with the large far-infrared excess of the star. We therefore conclude that thermal dust emission is responsible for the millimeter continuum emission from this source.

The measured continuum flux density can be used to estimate the mass of the circumstellar dust and gas. Hildebrand (1983) has derived a relationship between the mass of a parcel of H_2 gas and its flux of long wavelength thermal dust emission. The relationship can be written as

$$M_{H_2} = \frac{F_\nu D^2}{\kappa_\nu B_\nu(\nu, T)} \qquad (1)$$

where F_ν is the observed continuum flux density, D is the distance to the source, $B_\nu(\nu,T)$ is the Planck function at frequency ν and temperature T, and κ_ν is the mass opacity of the circumstellar dust grains. This relationship assumes that the thermal emission is optically thin, and is therefore valid only in the millimeter wavelength region for the objects considered here. Equation (1) can be re-expressed in the form

$$M_{H_2} = \frac{0.120 F_{Jy} (D_{kpc})^2 (\lambda_{mm})^3 (e^{14.4/\lambda_{mm} T_d} - 1)}{\kappa_\nu} \qquad (2)$$

There is some uncertainty regarding the correct value for the mass opacity at these wavelengths. Theoretical estimates of κ_ν have been made using assumptions about the size, shape, and composition of the dust grains; a standard interstellar gas to dust ratio must also be adopted. The results of different authors have varied by more than an order of magnitude (see discussion by Beckwith *et al.* 1990; Adams, Emerson, and Fuller 1990). I shall adopt the mass opacity expression used by Beckwith *et al.* (1990) in order to facilitate a comparison between this work and their millimeter continuum survey of T Tauri stars. Their expression for the mass opacity is

$$\kappa_\nu = \kappa_0 \left(\frac{\nu}{1.2 \text{x} 10^{12} \text{Hz}} \right)^\beta = \kappa_0 \left(\frac{0.25 \text{mm}}{\lambda_{mm}} \right)^\beta \qquad (3)$$

with $\kappa_0 = 0.1$ cm^2 gr^{-1} (Hildebrand 1983). It has been found observationally that the spectral index $\beta \approx 1$ in regions of circumstellar dust (Woody *et al.* 1989; Beckwith and Sargent 1991). With these assumptions, the value of κ_ν at $\lambda = 2.7$ mm is $9 \text{x} 10^{-3}$ cm^2 gr^{-1}.

The dust temperature must be estimated in order to derive gas masses from the observed millimeter continuum flux density. In general equation (2) should be integrated over the mass and temperature distributions of the emitting region to derive a total mass that is consistent with observed flux densities. This approach has been taken by Beckwith *et al.* (1990) and by Adams, Emerson, and Fuller (1990), where mass and temperature distributions predicted by disk models have been used to

derive circumstellar gas masses from millimeter continuum observations of T Tauri stars. A less exact approach is to adopt a single representative dust temperature for the emitting region and use it to estimate the circumstellar mass. This method was used by Sargent and Beckwith (1989, 1987) for the cases of DG Tau and HL Tau, and it yielded circumstellar mass estimates which are very close to those derived from an integration over a disk temperature distribution (Beckwith *et al.* 1990). A representative dust temperature is given by

$$T_d = \left(\frac{L_* T_{eff}^{\beta}}{16\pi\sigma r^2} \right)^{1/(4+\beta)} \tag{4}$$

(Beckwith *et al.* 1986), where r is the distance from the central star. The effective temperature of the radiation field seen by the circumstellar dust, T_{eff}, must lie between 70 K (a value consistent with the IRAS data) and 5000 K (the approximate stellar photospheric temperature determined by Reipurth *et al.* 1986). Using Cohen & Schwartz's (1987) value for the HH 34 star's bolometric luminosity (45 $L_\odot$) and $\beta = 1$, the dust temperature at 1000 AU is calculated to be in the range 28 - 67 K from the two possible values for T_{eff}. A value of 50 K will be adopted for the gas mass calculation.

Substituting $T_d \approx 50$ K, D = 0.46 kpc (Reipurth 1989), $\lambda_{mm} = 2.72$, $\kappa_\nu = 9\text{x}10^{-3}$ cm^2 gr^{-1}, and $S_\nu = 32$ mJy into equation (2), a molecular gas mass of 0.20 $M_\odot$ is derived for the unresolved emission core. If the extended emission is also included, the total S_ν= 60 mJy implies a mass of 0.38 $M_\odot$. Repeating this calculation with the CSO flux density at $\lambda = 1.3$ mm yields a similar result, suggesting that for $\beta = 1$ the size of the 1.3 mm continuum emission region (which

was unresolved by the CSO's 30″ beam) must be comparable to the size seen in the OVRO continuum map.

b) Molecular Line Emission, HH 34 Exciting Star

A map of the total integrated ^{13}CO emission associated with the HH 34 exciting star is shown in Figure 2. A region of molecular emission is seen at the position of the star (marked by a cross), and it is resolved by the 3.2x4.0″ beam. This map was produced by binning data from 16 channels of the 50 kHz filterbank, and covers the velocity range 7.27 to 9.45 km s^{-1}. No significant line emission was seen at velocities outside this range. The central velocity of this ^{13}CO emission (V_{LSR}= 8.3 km s^{-1}) differs from that of the ambient molecular cloud (Reipurth *et al.* 1986) by only 0.3 km s^{-1}. The brightest molecular emission is present in an east-west oriented 'bar' centered on the star, with the peak emission occurring 2″ west of the star. This 'bar' is spatially unresolved in the north-south direction, but is resolved and extends over a distance of 5″ (2300 AU at 460 pc) in the east-west direction. The position angle of the 'bar' is within 15° of being perpendicular to the HH 34 jet. Fainter ^{13}CO emission extends 6″ to the north of the stellar position; this emission overlaps the northern extension seen in the continuum map and fills the region in which Stapelfeldt *et al.* (1991) found near-infrared reflection nebulosity.

Four velocity channel maps of the HH 34 star's associated molecular gas are shown in Figure 3. Each map covers a velocity width of 0.27 km s^{-1}. The position of the HH 34 star is marked by a cross. In the different channel maps, the ^{13}CO emission peak shifts its position relative to the star. At the largest radial velocities (8.90 km s^{-1}, Figure 3*a*) the emission peak lies near the stellar position. Moving through lower radial velocities, the peak can be seen to shift first 2.7″ east of the star

(8.22 km s^{-1}, Figure 3*b*); then 3.6″ west of the star (7.95 km s^{-1}, Figure 3*c*). The lowest radial velocity channel (7.68 km s^{-1}, Figure 3*d*) shows the emission peak 2.0″ northwest of the star, as well as a new peak 9″ to the north. The kinematic pattern seen in these maps suggests that the circumstellar gas in the 'bar' is rotating about the HH 34 exciting star. This interpretation will be discussed further in section IV.

A second independent estimate of the mass of circumstellar material can be obtained using the observed ^{13}CO line flux and appropriate assumptions about physical conditions in the gas. Following A. Sargent (1989), the relationship between gas mass and line flux can be written as

$$M_{H_2} = \frac{2.74\text{x}10^{-9}(T_{ex} + 0.88)\tau_{13}(D_{kpc})^2 \int S_\nu dv}{e^{-5.29/T_{ex}}(1 - e^{-\tau_{13}})X(^{13}CO)} M_\odot \qquad (5)$$

where the integrated flux units are Jy km s^{-1}, T_{ex} is gas excitation temperature, τ_{13} is the line optical depth, and $X(^{13}CO)$ is the fractional ^{13}CO abundance relative to H_2. Assuming the gas to be in thermal equilibrium with the dust grains ($T_{ex} = T_d$), the approximate dust temperature of 50 K determined above may be used.

The total flux for the E-W molecular 'bar' seen in Figure 2 is 4.0 ± 0.4 Jy km s^{-1}. This is very close to the value measured in the two overlapping 1 MHz channels: 4.3 ± 0.7 Jy km s^{-1}. Using $X(^{13}CO) = 1.1\text{x}10^{-6}$ (Frerking, Langer, and Wilson 1982) and assuming the ^{13}CO emission to be optically thin, equation (5) yields a mass of 0.12 $M_\odot$ for the HH 34 circumstellar gas. Note the calculated mass increases if the ^{13}CO emission is optically thick, so the estimate of 0.12 $M_\odot$ should be considered a lower limit. This estimated disk mass is somewhat less than the value of 0.20 $M_\odot$ derived above from the millimeter continuum flux density, but the

agreement is adequate considering the systematic uncertainties in the assumptions used.

An exact agreement between the line and continuum mass estimates should not be expected for this object, for there are important morphological differences between the line and continuum maps. Significant line emission clearly originates at radii exterior to the region of continuum emission; the molecular emission is resolved into an E-W bar, whereas the continuum emission is dominated by an unresolved central core. The line emission peak is located 2″ to the west of the star where there is no corresponding continuum peak. In these circumstances the total mass of circumstellar gas is likely to be *greater* than either the line or continuum mass estimate alone. The additional unknown effects of emission line opacity could further increase the estimated mass. It is therefore quite probable that the total mass of material within 1200 AU of the HH 34 star could exceed 0.2 $M_{\odot}$.

c) Millimeter Continuum Emission, HH 111 Exciting Star

The interferometer map of the 2.7 millimeter continuum emission associated with the HH 111 exciting star is shown in Figure 4. The emission takes the form of a single unresolved peak at $\alpha = 05^h49^m09.2^s$, $\delta = +02°47'48.5''$, about 5″ east of Reipurth's (1989) reported 2 μm position for the HH 111 exciting star. The direction of this offset is almost along the axis of the HH 111 jet, with the millimeter emission peak located 'upstream' of 2 μm position. Interferometer studies to date have not identified a single case where a millimeter continuum emission peak is significantly displaced from the optical position of a pre-main sequence star. This fact, and the fact that the HH 111 exciting star's position has been measured at only one other wavelength, makes the millimeter continuum postion an equally viable candidate for

the actual stellar position. Infrared images (Stapelfeldt 1992) verify Reipurth's K band position, but also show a diffuse morphology suggesting that the K band object may be reflection nebulosity. Images at longer wavelengths (or perhaps deeper K band imaging or polarimetry) are needed to clarify the true position of the HH 111 exciting star. Throughout the following we will assume that the exciting star's position is coincident with the millimeter continuum peak.

The total 2.7 millimeter continuum flux density detected in the OVRO map is 46 $\pm$ 7 mJy. The 1.3 mm continuum flux density was also measured at the Caltech Submillimeter Observatory, with a value of 524 $\pm$ 32 mJy obtained (A. Sargent, personal communication). A frequency spectral index of 3.5 is implied by these two continuum measurements; this value is also consistent with a thermal dust emission mechanism, with $\beta = 1.5$.

The mass of circumstellar gas can be estimated from the observed continuum flux densities using the method described in section III*a*. T_{eff} is bounded at low values by the blackbody temperature that fits the IRAS data; 55 K. An upper limit for T_{eff} is not defined, however, because there is as yet no estimate for the spectral type of the HH 111 exciting star. Available data can therefore only place a lower limit on the dust temperature at 1000 AU, which is 24 K. A reasonable guess for the maximum T_{eff} is 5000 K (the same value as used for HH 34), in which case the maximum T_d is 59 K. A value of 45 K will be used in the mass calculation. Substituting T_d= 45 K, D = 0.46 kpc (Reipurth 1989), $\kappa_\nu = 9\text{x}10^{-3}$ cm^2 gr^{-1}, and S_ν = 46 mJy into equation (2), a molecular gas mass of 0.33 $M_\odot$ is derived.

d) Molecular Line Emission, HH 111 Exciting Star

The integrated ^{13}CO emission associated with the HH 111 exciting star is shown in Figure 5. All 32 narrowband channels were binned together to produce this map of emission in the heliocentric velocity range 23.7 km s^{-1} to 27.3 km s^{-1}. The central velocity, V_{helio} = 25.5 km s^{-1} (equivalent to V_{LSR}= 9.0 km s^{-1}) is only 0.4 km s^{-1} from the ambient molecular cloud CO velocity at this position (S. Tereby, personal communication). A bright peak of molecular emission coincides with the position of the 2.7 millimeter continuum peak (marked by a cross). The high intensity ^{13}CO emission region is resolved by the interferometer beam in the N-S direction – a direction nearly perpendicular to the HH 111 jet. Assuming a gaussian shape for the observed source and beam, the N-S extent of the source can be found from a simple deconvolution. The observed source and beam are well represented by gaussians of FWHM 7.1″ and 5.7″ respectively, implying the true N-S extent of the source is 4.2″; this corresponds to 2000 AU at a distance of 460 pc. The core emission is unresolved in the E-W direction. The broader E-W shape of the beam limits the degree of flattening which can be observed, but does constrain the E-W size of the source to be less than its N-S extent. To the west of the bright emission core, low-intensity molecular emission extends out to a distance of 12″ (.02 pc). This extended ^{13}CO emission corresponds to the region of high obscuration at the base of the cone-shaped reflection nebulosity described by Reipurth (1989).

Six maps depicting ^{13}CO emission in channels 0.54 km s^{-1} wide are shown in Figure 6. A cross marks the position of the millimeter continuum source in each figure. From one channel to the next, the molecular emission peak can be seen to shift its position relative to the star. At the largest heliocentric radial velocities (26.8 km s^{-1}, Figure 6*a*) the emission peak lies 2″ south of the stellar position. In the adjacent lower velocity channel (26.3 km s^{-1}, Figure 6*b*) the peak moves to 3″ south of the star, and a secondary peak appears 15″ to the west. Figure

6*c* shows no circumstellar emission centered at 25.7 km s^{-1}, while the secondary peak has intensified and shifted 2″ closer to the star. The position of the secondary peak suggests it is related to the western lobe of the HH 111 bipolar outflow. An emission peak at the stellar position appears and the secondary peak vanishes in the next velocity channel (25.2 km s^{-1}, Figure 6*d*). The velocity of the surrounding molecular cloud falls in this channel, implying that the line intensity shown in Figure 6*d* could be affected by foreground ^{13}CO absorption. The most intense circumstellar emission is found at 24.7 km s^{-1} (Figure 6*e*), with the peak emision located 1″ west of the star. The final map (velocity 24.1 km s^{-1}, Figure 6*e*) shows the peak emission 1″ north of the star. The overall pattern shown in Figure 6 is the movement of the ^{13}CO peak from south side to the north side of the star as the heliocentric radial velocity decreases. This pattern suggests the presence of a rotating gas structure extended perpendicular to the outflow axis, an interpretation discussed further in section IV. However, this interpretation is less robust than in the case of HH 34 because of the larger beam size.

The mass of circumstellar gas can be estimated again using the observed ^{13}CO line flux and the method employed in section III*b*. For the bright emission core at the stellar position (Figure 5), the total flux measured is 12.4 ± 0.2 Jy km s^{-1} over all channels in the 50 kHz filterbank (total width 4.35 km s^{-1}). This almost identical to the value measured in the two overlapping 1 MHz channels, 12.3 ± 0.6 Jy km s^{-1}. Assuming the gas temperature equals the dust temperature (T_{ex} = T_d = 45 K) and that the line emission is optically thin, equation (5) yields a mass of 0.34 $M_\odot$ for the HH 111 circumstellar gas. Note the calculated mass increases if the line emission is optically thick, so the estimate of 0.34 $M_\odot$ should be considered a lower limit. This mass estimate is only a bit less than the value derived above from the millimeter continuum fluxes. As in the case of HH 34, the total mass of

circumstellar material associated with the HH 111 exciting star could exceed the values estimated separately from the line and continuum fluxes because the line and continuum emitting regions do not fully overlap.

IV. Discussion

Spectral Energy Distributions

Spectral energy distributions for the HH 34 exciting star and HH 111 exciting star are shown in Figures 7*a* and 7*b*. The spectral energy distributions of L1551/IRS5 and HL Tau are shown for comparison in Figures 7*c* and 7*d*; these well-studied sources have bolometric luminosities of 35 $L_\odot$ and 8.7 $L_\odot$ respectively (Cohen and Schwartz 1987; Adams, Emerson and Fuller 1990). L1551/IRS5 is the source of a bipolar molecular outflow which is associated with HH 28 and HH 29, thus qualifying the source as an HH object exciting star. HL Tau is thought to have a circumstellar disk that extends from 0.1 AU to 100 AU radial distance (Beckwith it et al. 1990). The large uncertainties in the IRAS fluxes for the HH 34 star are due to source confusion in the IRAS beam. Cohen and Schwartz's (1987) value for the HH 34 star's total luminosity (45 $L_\odot$) assigns most of the regions' IRAS flux to the HH 34 star; if other sources are significant the true luminosity of the HH 34 star could be lower. Extinction corrections have been made for the short wavelength HH 34 data. Like L1551/IRS5, both HH jet sources have a spectrum that rises over the wavelength region between 12 μm and 100μm. Both stars are therefore 'class I' sources in the young stellar object spectral taxonomy of Adams, Lada, and Shu

(ALS, 1987). Class I sources are thought to represent one of the earliest stages of stellar evolution, when a young star and its circumstellar disk are still accreting mass from residual infalling material.

At IRAS wavelengths the circumstellar material of a YSO is usually optically thick; consequently, the observed fluxes should depend only on the integral of the temperature distribution over the emitting surface area. To produce a continuum spectrum that peaks near 100 microns, the emitting surface area of low temperature regions (50 K) must be much larger than emitting surface area of higher temperature regions. For a 'class I' source, the angular momentum of infalling material prevents direct accretion on to the central star; instead this material must accrete to the developing circumstellar disk at some finite radius. This infalling material will be distributed above and below the plane of the circumstellar disk, in regions of low temperature. Such infalling material is a prime candidate to provide the large surface area at low temperature that is needed to explain the infrared spectum of class I sources such as the HH 34 and HH 111 exciting stars (ALS 1988, 1987). To produce the observed infrared spectrum, the total mass of this surrounding envelope need only be a small fraction of the total circumstellar mass.

There is an interesting aspect of the HH exciting star spectra at short wavelengths. Relative to HL Tau, whose continuum spectrum is relatively flat at a level of 10^{34} erg s^{-1} between 3 μm and 100 μm (fig 7*d*), the HH object exciting stars have smaller luminosities at wavelengths shorter than 20 μm. This is also true relative to DG Tauri (ALS 1988). It is possible that this deficit of short wavelength emission occurs because of a cleared inner zone within the circumstellar material. By Wein's displacement law, the deficit of 12 μm emission implies a sharply decreased emitting surface area for regions where the temperature exceeds 400 K. Assuming that stellar

radiation is the dominant energy input to the circumstellar material (which may not be true), the radius of the "cleared" region could be as large as 10 AU for a 30 $L_\odot$ star. It should be emphasized that this region can be described as 'cleared' only in a relative sense versus the flat-spectrum T-Tauri stars, and it is likely that the region still contains some circumstellar material. Nevertheless, it is quite plausible that the strong bipolar outflows from the HH exciting stars could act to partially or completely carry away circumstellar material from regions proximate to the flow source, thus reducing the objects' mid-infrared emission.

The mass of the stars

It is not possible to definitively locate the two stars in an HR diagram because of a lack of good spectral type information, and in the case of the HH 34 exciting star poor quality IRAS data. Under the circumstances, the best available constraint on the stellar masses is an upper limit derived by comparison of the source luminosities with pre-main sequence evolutionary tracks. In the unlikely limiting case where the observed source luminosity arises *entirely* from stellar energy generation, the tracks of Cohen and Kuhi (1979) imply stellar masses of 3 $M_\odot$ and 2.5 $M_\odot$ for the HH 34 and HH 111 stars, respectively. These values were found by identifying the largest stellar masses whose PMS evolutionary tracks 'bottomed out' at the observed source luminosities, and as such represent mass upper limits. Lower mass stars on the Hayashi track will show the same luminosity, so it is very probable that the stellar masses are below these upper limits. In addition, a large part of the total source luminosity may be generated by processes within the circumstellar disk, thereby reducing the stellar contribution to the total luminosity. A useful comparison is the case of DG Tau, an active T Tauri star similar to the objects studied here because it possesses a jet and quite likely possesses a circumstellar

disk. The equivalent width of the 6300 Å [O I] line, a quantity which Cohen, Emerson, and Beichman (1989) have found to be correlated with intrinsic disk luminosity in T Tauri stars, is about the same for DG Tau and the HH 34 exciting star (Cohen and Kuhi 1979; Reipurth *et al.* 1986). Adams, Emerson, and Fuller (1990) estimate on the basis of infrared spectral modelling that fully 90% of DG Tau's luminosity originates in a circumstellar disk; the disk luminosity source is uncertain but may include the accretion of infalling material and/or the effects of gravitational instabilities within the disk. Class I sources may be accreting material even more rapidly than T Tauri stars (Shu, Adams, and Lizano 1987). Naively using the DG Tau fraction to estimate the disk luminosity for the HH 34 and HH 111 sources, the reduced stellar luminosities drop the the stellar mass upper limits to 1.7 $M_\odot$ and 1.4 $M_\odot$ respectively. Detailed spectral modelling, based on improved determinations of these sources' spectral energy distributions, is needed to yield a more reliable estimate of the stellar luminosities. It is clear that even though the systems' bolometric luminosities are high, the stellar masses are likely to be less than 2 $M_\odot$. The kinematic structure of the circumstellar gas is consistent with this determination, and could allow even lower stellar masses.

Mass Determination Uncertainties

Estimates of the circumstellar material masses made in section III are dependent on the assumed gas temperature. There is reason to believe that the temperatures adopted in the mass estimation process, although relatively unconstrained by the data, are not greatly in error. Because the equations governing the continuum and line derived mass estimates have different temperature dependences, an incorrect choice for the characteristic circumstellar material temperature will yield divergent mass estimates. For the range of temperatures considered here (greater

than 30 K), the the mass estimated from the ^{13}CO line fluxes is roughly proportional to the assumed temperature (see equation 5); however, the continuum-derived mass estimates are very nearly *inversely* proportional to the assumed temperature of the dust (see equation 2). The relatively close agreement in the results of the two mass estimation methods therefore suggests that the characteristic temperatures assumed for these objects are accurate to within a factor of 2.

The greatest uncertainty in the millimeter continuum mass estimates originates in the adopted value for the mass opacity κ_ν. If the standard interstellar mass opacity law ($\kappa_\nu \propto \nu^2$; i.e. $\beta = 2$) is employed in the estimates, then the calculated circumstellar masses become extremely large: 1.2 $M_\odot$ for HH 34 and 3.5 $M_\odot$ for HH 111. These masses are probably too large to be reconciled with the masses estimated from the observed ^{13}CO fluxes. Even if τ_{13} is as large as 3 (which is the case for HL Tau; see Sargent and Beckwith 1987), the estimated masses would only increase to .38 $M_\odot$and 1.1 $M_\odot$ for HH 34 and HH 111 respectively. In addition, the large circumstellar masses which are required by a $\beta = 2$ opacity law appear to be inconsistent with the observed kinematics of the circumstellar gas (see below). Finally, it is clear that the millimeter continuum spectra of these two sources is not fit well by a $\kappa_\nu \propto \nu^2$ opacity law. Although significant uncertainty remains in the values used here for κ_ν (the value of κ_0 in particular), it appears unlikely that the lowest estimates of κ_ν are applicable to these two sources.

Circumstellar Disks

There is evidence to suggest that the bulk of the molecular gas found in association with these two jet sources is gravitationally bound to the central stars. The ^{13}CO emission associated with these two jet sources is centered at velocities

less than 0.5 km s^{-1} from the ambient cloud velocities. Only small radial velocity differences are expected between true circumstellar gas and the ambient cloud, for the central star is presumed to have recently formed from the surrounding molecular cloud material. Furthermore, the velocity width of the line emission is only 2.2 and 2.7 km s^{-1} for HH 34 and HH 111 respectively. From a vantage point near the orbital plane, the expected velocity width for material orbiting at a distance of 1000 AU (the radius of the observed ^{13}CO emission regions) from a 1 $M_{\odot}$ star is 2.6 km s^{-1}, very close to the observed velocity widths. It is therefore plausible that the observed ^{13}CO emission arises in gravitationally bound circumstellar material.

An alternative possibility is that the observed line emission is related to the strong outflows emanating from these sources. However, it is difficult to reconcile an outflow model with the observed kinematics of the molecular gas. The radial velocities of the optical jets are large: -85 km and -60 km s^{-1} for HH 34 and HH 111 respectively (Buhrke, Mundt, and Ray 1988; Reipurth 1989). If the observed ^{13}CO emission was related to the outflows in a dynamically significant way, then its radial velocity should differ from that of the ambient cloud by several km s^{-1}; this is not the case for HH 34 and HH 111. In addition, molecular outflows are in general more easily observed in CO than in ^{13}CO; interferometer maps of the strong HH 7-11 outflow show abundant CO emission but relatively little high-velocity ^{13}CO emission associated with the outflow (Grossman *et al.* 1987). No high-velocity ^{13}CO emission was detected in either the HH 34 or the HH 111 source fields within $\pm$ 40 km s^{-1} of ambient cloud velocities. We therefore conclude that kinematics of the observed ^{13}CO emission is best understood if the emission arises in quiescent circumstellar material, and that the bulk of this material is gravitationally bound to the central stars.

Rotation curve matters in here.

A final point to argue that we are observing circumstellar disks at HH 34 and HH 111 is the presence of the jets. These high-velocity flows are obviously clearing a channel along an axis through the surrounding circumstellar material. A spherical circumstellar mass distribution is clearly ruled out; the simplest mass distribution consistent with the outflowing jets is a circumstellar disk. For identical reasons, accretion disks are believed to accompany the sources of the much larger and more energetic quasar and galactic radio jets.

The Disk Role in Jet Collimation

A major question about the jet collimation process is the role of magnetic fields. If the central star has a sufficiently strong magnetic field, then the inner portion of the disk will co-rotate with the central star. If the central star is rotating fast enough, this co-rotation will accelerate disk material. For a dipole field, co-rotating disk material at high magnetic latitudes can be accelerated to high velocities by "centrifugal" forces as the plasma follows the field lines. By collisions with fast-moving charged particles, neutrals can also be accelerated to high velocities and escape the system along the magnetic poles. This is one of the suggested jet formation mechanisms.

In an alternative scenario, an initially isotropic stellar wind is extrinsically collimated by the surrounding circumstellar disk; magnetic fields play little role. Konigl (1982) has shown that in such circumstances the flow emerges at the rotational poles of the disk, and that the disk can form a deLaval nozzle that collimates and accelerates a jet flow. The available observations of the HH 34 system allow

a schematic test of this hypothesis. If the observed momentum flux in the jet was isotropically distributed over a hemisphere, the dynamic pressure on the inner edge of the disk would be ρ_j v_j^2 $r_j^2/2$ r_i^2, where r_i is the disk inner radius and ρ_j, r_j, and v_j are the jet density, radius, and velocity respectively. Approximating the disk as an annular slab, the disk mass per unit area pressured by the wind is M_d/π r_i^2 t, where M_d is the total disk mass and t is the disk thickness. Over a time τ the isotropic wind would radially accelerate the disk material to a velocity of

$$V_{wind} = \frac{\pi \rho_j v_j^2 \tau t r_j^2}{M_d r_i} \qquad (6)$$

Burhke, Mundt, and Ray (1988) find $n_j = \rho_j/m_H = 10^2$ cm^{-3} and $r_j = 150$ AU; from the jet proper motion, Reipurth (1989) finds $v_j = 220$ km s^{-1}. Choosing r_i= 10 AU (as suggested by the spectral energy distribution), $\tau = 10^4$ yrs (the minimum age of the outflow), $M_d = 0.2$ $M_\odot$, and disk thickness t= 1 AU at the inner radius yields a V_{wind} of only 100 cm s^{-1}. This velocity is much smaller than typical circular orbital velocities (1-13 km s^{-1} between 1000 AU and 10 AU, assuming a 1 $M_\odot$ star). Although this calculation is very approximate (it entirely neglects gravitational effects), it demonstrates that the observed HH 34 disk is stable against disruption by an isotropic, jet-producing wind; therefore, the disk should be capable of extrinsically collimating the jet.

Comparison with Millimeter Wave Studies
of other Pre-Main Sequence Objects

In Table 1 the observed 2.6 mm flux density, distance, and 2.6 mm luminosity $L_{2.6}$ is shown for six pre-main sequence stars. The 2.6 mm luminosity of each object

is expressed relative to HL Tauri, the most luminous source observed by Beckwith *et al.* 1990 in their millimeter continuum survey of T Tauri stars in Taurus-Auriga. It can immediately be seen that the HH 34 and HH 111 exciting stars are intrinsically more luminous in the 2.6 mm continuum than the T Tauri stars by a factor of 3. Provided that the circumstellar temperature structure does not vary greatly among these objects, the circumstellar material mass $M_{cir} \propto L_{2.6}$ because the circumstellar region is optically thin at 2.6 mm.

Table 2 presents the molecular line flux, distance, ^{13}CO luminosity, and source size for six pre-main sequence stars which have been observed with the OVRO interferometer. The ^{13}CO luminosities are expressed relative to HL Tauri. No account has been made for variations in ^{13}CO opacity between sources. Although the source sizes are generally similar (several thousand AU), the ^{13}CO luminosities range over more than an order of magnitude. The ^{13}CO luminosity of the HH 111 exciting star is particularly large : 11 times HL Tauri. We expect the circumstellar mass to be roughly proportional to the ^{13}CO luminosity, provided that the temperature structure, ^{13}CO fractionation, and ^{13}CO opacity do not vary greatly among these sources. The apparent ^{13}CO luminosity of an embedded source (such as the HH 111 exciting star) may be diminished by absorption in foreground molecular cloud material, whereas optically visible T Tauri stars are less likely to suffer ^{13}CO absorption because they are comparatively free of surrounding molecular cloud material.

In Table 3, large beam measurements of the 1.3 mm continuum emission from five YSOs is shown. The same trend is evident in these data, that is the largest luminosities are found for the HH jet sources.

The millimeter line and continuum flux densities *alone* therefore suggest that

Herbig-Haro object exciting stars possess the most massive disks known to be associated with low-mass pre-main sequence stars. This conclusion is *independent* of the value chosen for the mass opacity κ_ν, a parameter upon which different authors disagree and which thus sometimes confuses mass comparisons. It is interesting to note that even though the HH disks are more massive than the T-Tauri disks, their sizes are comparable : 2000-3000 AU. This suggests that the surface densities are also larger in the HH disks. It is interesting to note that nearly all of the objects shown in Table 1-3 show *both* (1) the largest inferred disk masses of low-mass YSO's; and (2) highly collimated optical jets. These two source properties therefore appear to be related.

The Significance of Massive Disks

There are two different ways to interpret the massive HH disks. The first possibility is that the combination of massive disks and energetic outflows is an indication of stellar youth; that HH exciting stars evolve over time to become T Tauri stars; and that as the stars age, their luminosity, mass loss rate, and accompanying disk mass decreases. A very appealing aspect of this scenario is that it naturally accounts for the fact that optically visible HH exciting stars share many characteristics with the most "active" T Tauri stars. Significant reddening, strong polarization, strong forbidden line emission, nearby reflection nebulosity, and infrared excess are properties which are common to HL Tau, DG Tau, and the HH 34 exciting star. It is very significant that HL and DG Tau also have the most prominent optical jets *and* the largest millimeter continuum luminosities of the objects in their class (Mundt *et al.* 1990; Beckwith *et al.* 1990), although each is less remarkable in these respects than the HH 34 star. Based on these many similarities, it seems quite plausible that HH exciting stars, active (or continuous spectrum) T Tauri stars, and less active clas-

sical T Tauri stars represent an evolutionary sequence, and that large disk masses are rapidly processed into some other form during the first stages of that evolution.

An alternative interpretation for the massive HH disks is that the combination of massive disks and energetic outflows is a result of some special properties of the stellar source, for example its mass or binarity. It is significant that HH 34 and HH 111 are both found in Orion, which unlike the Taurus clouds is forming both high and low mass stars. It is possible that these two jet sources are young stars of mass 2 $M_{\odot}$, and that larger disk masses are a by-product of the formation of more massive stars. This possibility can be addressed with improved mass determinations for embedded or reddened YSO's, a prospect that may be realized soon with the advent of cryogenic infrared echelle spectrographs allowing spectral type determinations from 2 micron photospheric features. However, this scenario does not naturally account for the optical obscuration and rising infrared spectra of most HH exciting stars.

The existence of massive disks raises the possibility that low-mass stars may accrete a substantial fraction of their mass from circumstellar disks. To produce the radial mixing needed to sustain high accretion rates, spiral-wave instabilities in a massive circumstellar disk have been proposed (Shu *et al.* 1990). Due to the uncertainties in our knowledge of the disk and stellar masses in these two systems, it cannot yet be determined if the disk/star mass ratio for HH 34 and HH 111 exceeds the threshold at which instability formation is predicted. However, the fact that HH exciting star disks appear to be very massive suggests that they may be the best candidate objects in which the effects of such instabilities could be observed.

The existence of massive circumstellar disks also has implications for the for-

mation of planetary systems, namely that circumstellar masses much greater than the minimum mass solar nebula (by a factor ≈ 100) are observed to be available for condensation into solid objects. The observed sizes of the HH and T Tauri disks are much larger than size of our solar system. If the material in these disks is not dispersed or accreted, it could serve as a reservoir for the formation of massive comet clouds (Oort clouds). The inner regions of massive disks, where orbital timescales are short enough for large objects to form before nebula dissipation, may be an ideal location for the formation of brown dwarfs, planets of several Jupiter masses, or even a low-mass binary stellar companion.

V. Conclusions

(1) OVRO millimeter interferometer maps reveal spatially compact regions of circumstellar material associated with both the HH 34 and HH 111 exciting stars. The brightest ^{13}CO emission is extended 2000 AU in a direction perpendicular to the highly collimated optical jets that emerge from these two sources, and unresolved in the jet direction. This morphology, combined with evidence for rotation found in the observed kinematics, strongly suggests that each source is accompanied by a circumstellar disk.

(2) Circumstellar disk masses have been estimated for each source using the observed ^{13}CO flux and the flux density in the 2.7 mm continuum. For HH 34, the estimated disk mass is 0.2 $M_\odot$; for HH 111, the estimated disk mass is 0.4 $M_\odot$. These masses are significantly larger (by a factor of 2-4) than the largest disk

masses derived for T Tauri stars.

(3) Both sources show a rising spectrum from 25 μm to 100 μm. This argues that these objects are still surrounded by an infalling envelope of material, and thus they are among the youngest stars. The stellar masses are uncertain, but are likely to be less than 2 $M_{\odot}$.

(4) Because such large disk masses are not found among older T Tauri stars, it appears that much disk material is being rapidly processed into some other form during the bipolar outflow phase of early stellar evolution. Dispersal of the disk material, accretion onto the central star, and the formation of substellar condensed objects may all play significant roles in depleting the early reservior of material.

(5) The observed mass of the HH 34 circumstellar disk appears sufficient to collimate an initially isotropic outflow into the observed jet.

Acknowledgements

The author expresses his thanks to the entire staff of the Owens Valley Radio Observatory for their support of the Millimeter Interferometer. I wish also to express my appreciation to Anneila Sargent for her encouragement and assistance, and to her and Steve Beckwith for observing HH 34 and HH 111 at the CSO and making the results available prior to publication. Sue Tereby was helpful in several conversations. KRS acknowledges the suppport of a NASA Graduate Fellowship.

References

Adams, F. C., Emerson, J. P., and Fuller, G. A. 1990 Ap.J. 357 606

Adams, F. C., Lada, C. J., and Shu, F. H. 1988 Ap.J. 326 865

Adams, F. C., Lada, C. J., and Shu, F. H. 1987 Ap.J. 312 788

Beckwith, S., and Sargent, A. I. 1991 in preparation.

Beckwith, S., Sargent, A. I., Chini, R. S., and Gusten, R. 1990 A.J. 99 924

Beckwith, S., Sargent, A. I., Scoville, N. Z., Masson, C. R., Zuckerman, B., and Phillips, T. G. 1986 Ap.J. 309 755

Beckwith, S., Zuckerman, B., Skrutskie, M. F., and Dyck, H. M. 1984 Ap.J. 287 793

Beichman, C. A., Neugebauer, G., Habing, H. J., Clegg, P. E., and Chester, T. J. (eds.) 1988 *The IRAS Point Source Catalog*, NASA Research Publication 1190 U.S. Government Printing Office

Beichman, C. A., Myers, P. C., Emerson, J. P., Harris, S., Mathieu, R., Benson, P. J., and Jennings, R. E. 1986 Ap.J. 307 337

Boss, A. P. 1987 Ap.J. 316 721

Burhke, T., Mundt, R. and Ray, T. P. 1988 Astr.Astrophys. 200 99

Cohen, M. and Schwartz, R. D. 1987 Ap.J. 316 311

Cohen, M., Emerson, J. P., and Beichman, C. A. 1989 Ap.J. 339 455

Cohen, M., Harvey, P. M., and Schwartz, R. D. 1985 Ap.J. 296 633

Cohen, M., Harvery, P. M., Schwartz, R. D., and Wilking, B. A. 1984 Ap.J. 278 671

Cohen, M. and Kuhi, L. V. 1979 Ap.J.Suppl. 41 743

Edwards, S., Cabrit, S., Strom, S. E., Heyer, I., Strom, K. M, and Anderson, E. 1987 Ap.J. 321 473

Frerking, M., Langer, W. K., and Wilson, R. 1982 Ap.J. 262 590

Grossman, E. N., Masson, C. R., Sargent, A. I., Scoville, N. Z., Scott, S. L., and Woody, D. P. 1987 Ap.J. 320 356

Hildebrand, R. H. 1983 Quart.Journ.R.A.S. 24 267

Keene, J. and Masson, C. R. 1990 Ap.J. 355 635

Konigl, A. 1982 Ap.J. 261 115

Myers, P. C., Fuller, G. A., Mathieu, R. D., Beichman, C. A., Benson, P. J., Schild, R. E., and Emerson, J. P. 1987 Ap.J. 319 340

Mundt, R., Ray, T. P., Buhrke, T., Raga, A., and Solf, J. 1990 Astr.Ap. 232 37

Mundt, R., Brugel, E. W., and Buhrke, T. 1987 Ap.J. 319 275

Mundt, R. 1986 CanadianJ.Phys, 64 407

Mundt, R. and Fried, J. W. 1983 Ap.J. 274 L83

Reipurth, B. 1989 Nature 340 42

Reipurth, B. in *Low Mass Star Formation and Pre-Main Sequence Objects*, ESO Conference Proceedings No. 33 (1989), ed. Bo Reipurth, pp. 247-279.

Reipurth, B., Bally, J., Graham, J. A., Lane, A. P., and Zealey, W. J. 1986: Astron.Astrophys. 164 51

Sargent, A. I. in *The Formation and Evolution of Planetary Systems*, STSci Symposium Series 3 (1989), H. A. Weaver and L. Danly eds., Cambridge University Press, pp. 111-129.

Sargent, A. I., and Beckwith, S. in *Structure and Dynamics of the Interstellar Medium*, IAU Colloquim No. 120 (1989) G. Tenorio-Tagle, M. Moles, and J. Melnick eds., Springer-Verlag, pp. 111-129.

Sargent, A. I., and Beckwith, S. 1987 Ap.J. 323 294

Sargent, A. I., Beckwith, S., Keene, J. and Masson, C. 1988 ApJ. 333 936

Scarrott, S. M. 1988 MNRAS 231 1055

Schwartz, R. D. 1983 Ann.Rev.Astron.Astrophys. 21 209

Shu, F. H., Tremaine, S., Adams, F. C., and Ruden, S. P. 1990 Ap.J. 358 495

Shu, F. H., Adams, F. C., and Lizano, S. 1987 Ann.Rev.Astron.Astrophys. 25 23

Stapelfeldt, K. R., Beichman, C. A., Hester, J. J., Scoville, N. Z., and Gautier, T. N. 1991 ApJ. 371 226 (Chapter II).

Strom, K. M, Strom, S. E., Edwards, S., Cabrit, S., and Skrutskie, M. F. 1989a AJ 97 1451

Strom, K. M. Newton, G., Strom, S. E., and Seaman, R. L. 1989b ApJSuppl 71 183

Strom, K. M., Strom, S. E., Wolff, S. C., Morgan, J., and Wenz, M. 1986 Ap.J.Suppl. 62 39

Weintraub, D. A., Masson, C. R., and Zuckerman, B. 1989 Ap.J. 344 915

Weintraub, D. A., Sandell, G., and Duncan, W. D. 1989 Ap.J. 340 L69

Woody, D. P., Miller, R. E, and Wengler, M. J. 1985: IEEE Transactions, M.T.T. 33 90

Woody, D. P., Scott, S. L., Scoville, N. Z., Mundy, L. G., Sargent, A. I., Padin, S., Tinney, C. G., and Wilson, C. D. 1989 Ap.J. 337 L41

TABLE 1

Millimeter Interferometer Continuum Observations of Circumstellar Material associated with Low Mass Pre-Main Sequence Stars

Object	Reference	Distance (pc)	2.6 mm flux milliJanskys	Luminosity (HL Tau = 1)
HH 34 star	1	460	60	5.4
HH 111 star	1	460	46	4.1
SVS 13	2	350	80	4.2
L1551 IRS5	3	140	150	1.3
HL Tau	4	140	120	1.0
DG Tau	5	140	70	0.6

TABLE 2

Millimeter Interferometer Molecular Line Observations of Circumstellar Material associated with Low Mass Pre-Main Sequence Stars

Object	Reference	Distance (pc)	Line Observed	Line Flux Jy km s^{-1}	Luminosity (HL Tau = 1)	Source Size (AU)
HH 111 star	1	460	^{13}CO	12.4	14.4	2000
HH 34 star	1	460	^{13}CO	4.0	4.6	3000
SVS 12	6	350	^{13}CO	18.5	12.4	10000
L1551 IRS5	3	140	$C^{18}O$	3.0	*2.0	1400
HL Tau	4	140	^{13}CO	9.3	1.0	4000
DG Tau	5	140	^{13}CO	6.2	0.7	4000

* The optically thin ^{13}CO / $C^{18}O$ ratio of 6.1 was used to derive this value.

(1) This work

(2) Grossman *et al.* 1987

(3) Sargent, Beckwith, Keene, and Masson 1988

(4) Sargent and Beckwith 1987

(5) Sargent and Beckwith 1989

(6) Stapelfeldt 1991 in preparation

TABLE 3

Single-Dish Millimeter Continuum Observations of Circumstellar Material associated with Low Mass Pre-Main Sequence Stars

Object	Reference	1.3 mm flux milliJanskys	Distance (pc)	Luminosity (HL Tau = 1)
HH 111 star	1	524	460	6.4
HH 34 star	1	479	460	5.9
L1551 IRS5	2	2300	140	2.6
HL Tau	3	879	140	1.0
DG Tau	3	443	140	0.5

(1) A. Sargent, personal communication

(2) Keene and Masson 1990

(3) Beckwith, Sargent, Chini, and Gusten 1990

FIGURE CAPTIONS

Figure 1. A map of the 2.7 mm continuum emission associated with the HH 34 exciting star. The stellar position is marked by a cross. The contour interval is 4 mJy/beam and the peak intensity is 32 mJy/beam.

Figure 2. A map of the total integrated ^{13}CO emission associated with the HH 34 exciting star. The star's optical position is marked by a cross. The contour interval is 90 mJy/beam and the peak intensity is 630 mJy/beam. The velocity width of the channel is 2.18 km $^{-1}$.

Figure 3. Four channel maps showing the velocity structure of the ^{13}CO emission associated with the HH 34 exciting star. Each channel is 0.27 km s^{-1} wide; the stellar position is marked bay a cross. Panels *a* through *d* show the emission at V_{LSR} = 8.90, 8.22, 7.95, and 7.68 km s^{-1} respectively. The contour interval is 250 mJy/beam.

Figure 4. A map of the 2.7 mm continuum emission associated with the HH 111 exciting star. The contour interval is 4 mJy/beam and the peak intensity is 53 mJy/beam.

Figure 5. A map of the total integrated ^{13}CO emission associated with the HH 111 exciting star. The position of the millimeter continuum peak is marked by a cross. The contour interval is 120 mJy/beam and the peak intensity is 1.4 Jy/beam. The velocity width of the channel is 4.35 km $^{-1}$.

Figure 6. Six channel maps showing the velocity structure of the ^{13}CO emission

associated with the HH 111 exciting star. Each channel is 0.54 km s^{-1} wide; the position of the millimeter continuum peak is marked by a cross. Panels *a* through *f* show the emission at V_{helio} = 26.8, 26.3, 25.7, 25.2, 24.7, and 24.1 km s^{-1} respectively. The contour interval is 200 mJy/beam.

Figure 7. Four spectral energy distributions are shown. Panel *a* shows the SED for the HH 34 exciting star, with data taken from Reipurth (1986), Cohen and Schwartz (1987), and this work. Panel *b* shows the SED for the HH 111 exciting star, with data from Reipurth (1989), the IRAS Point Source Catalog (Beichman *et al.* 1988), and this work. For comparison the spectral energy distributions of HL Tau and L1551/IRS5 are shown in panels *c* and *d*. HL Tau data is taken from K. Strom *et al.* (1989a) and Beckwith *et al.* (1990); data for L1551/IRS5 is from Cohen and Schwartz (1983), the IRAS PSC, and Keene and Masson (1990).

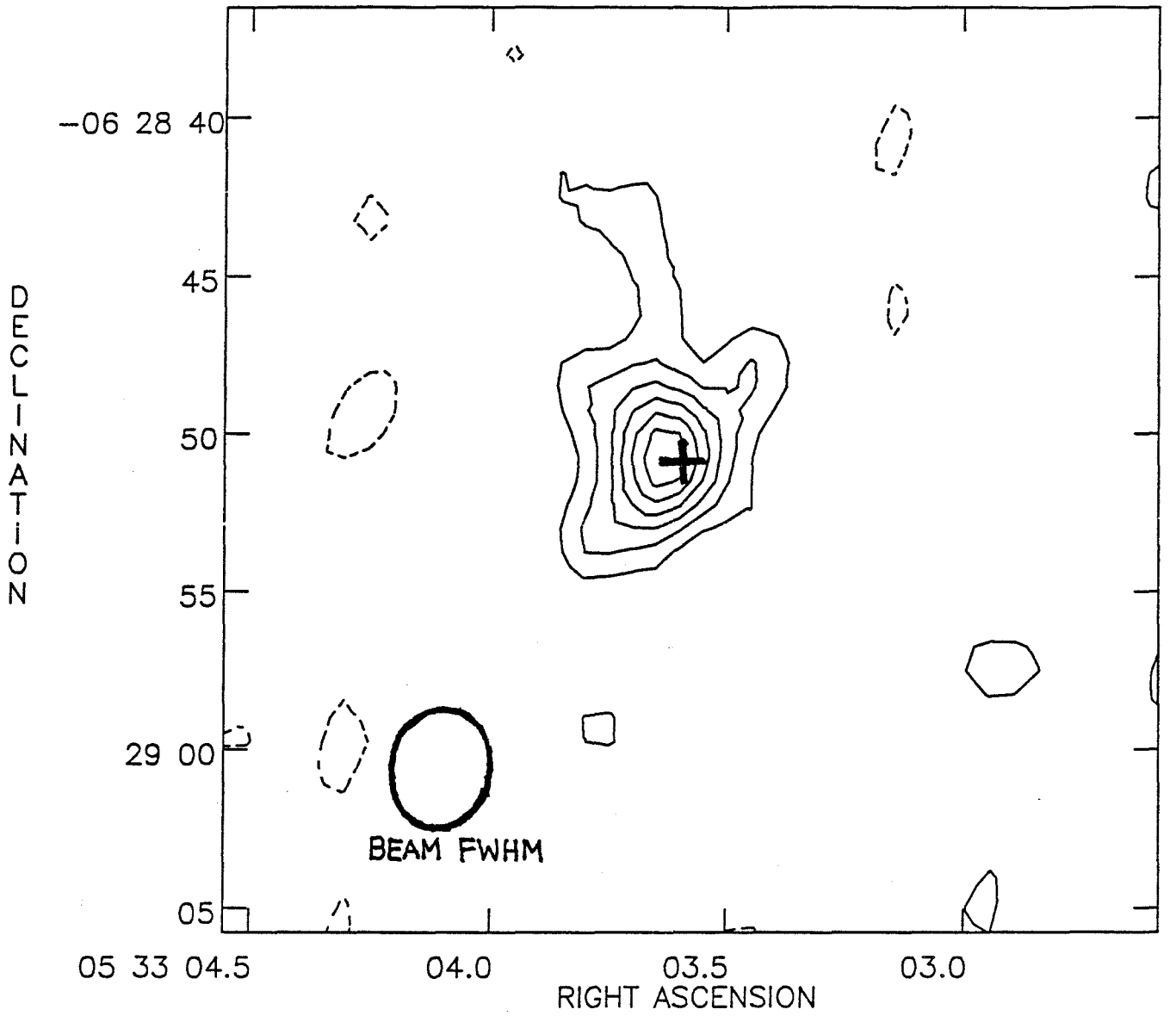

HH 34 Continuum Map

Figure 2

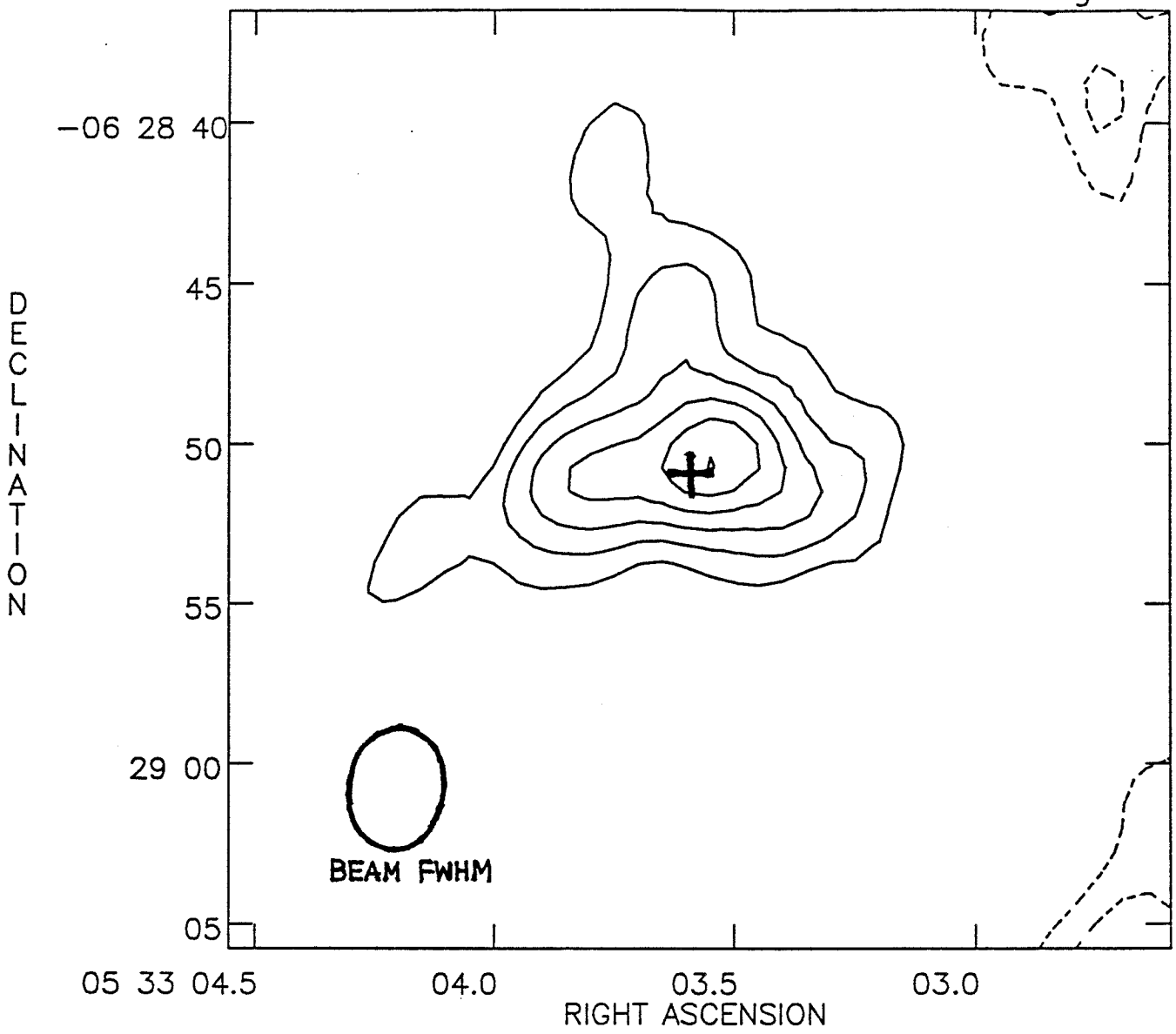

HH 34 ^{13}CO Map

Figure 3

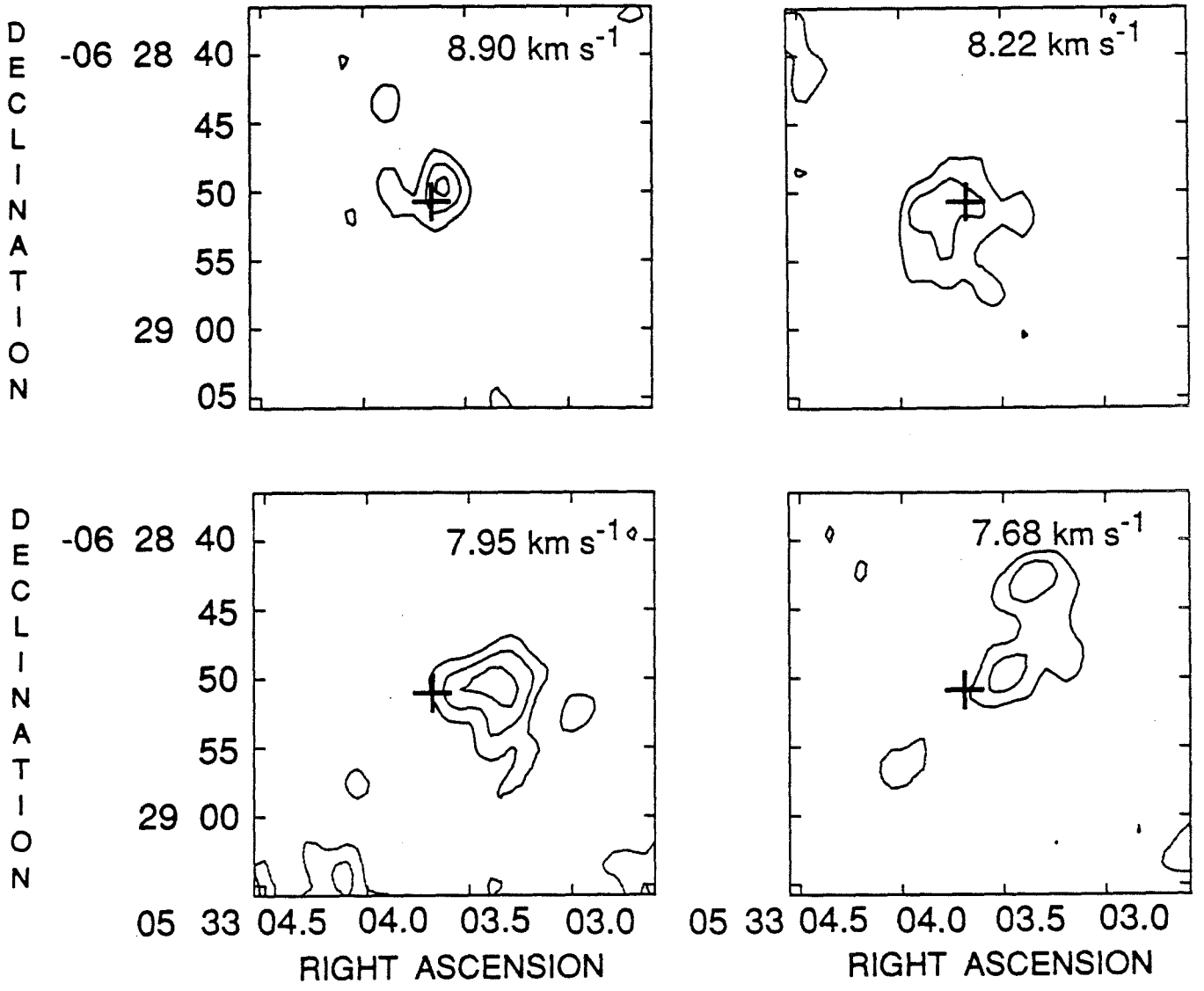

HH 34 ^{13}CO Channel Maps

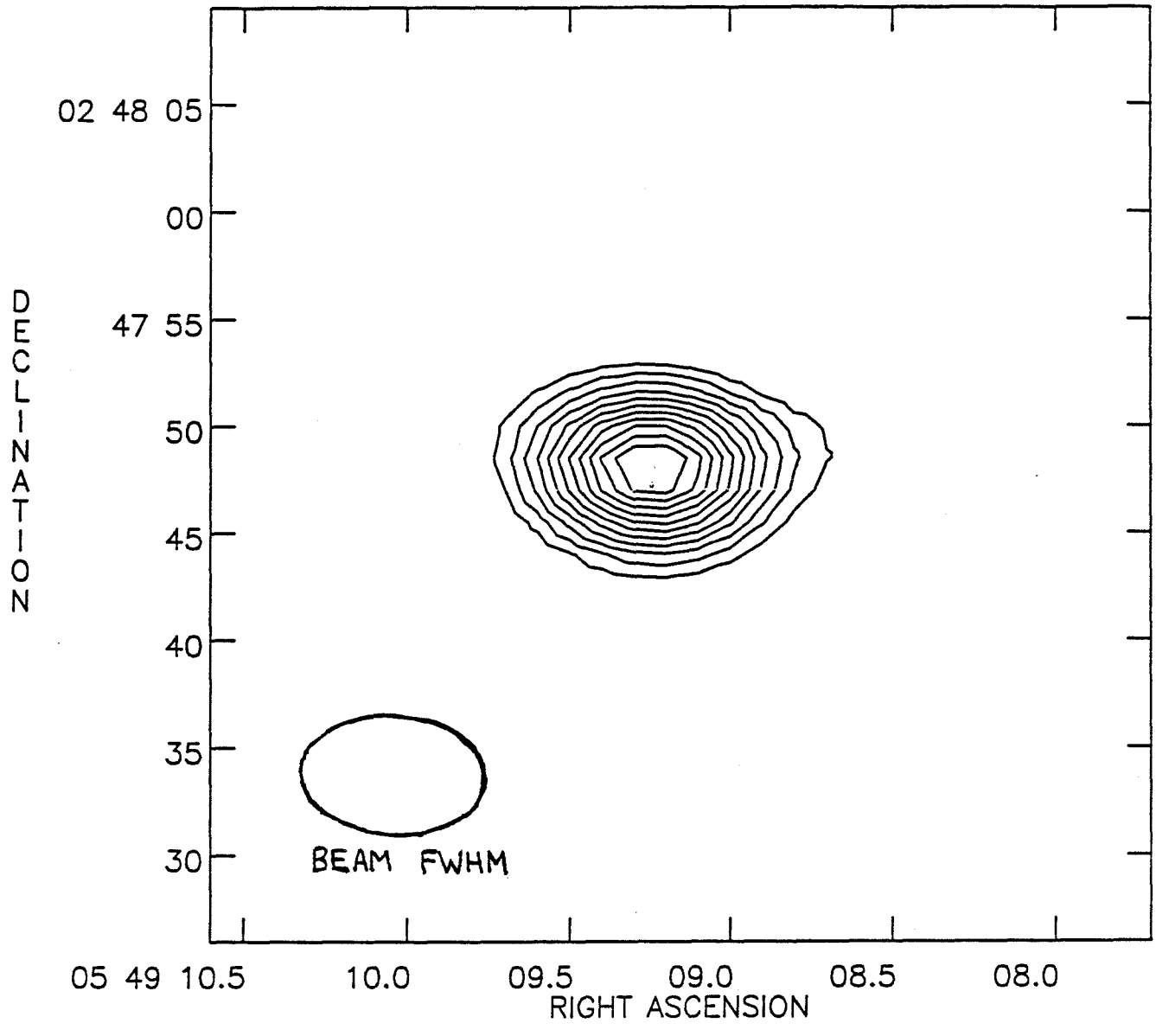

HH 111 Continuum Map

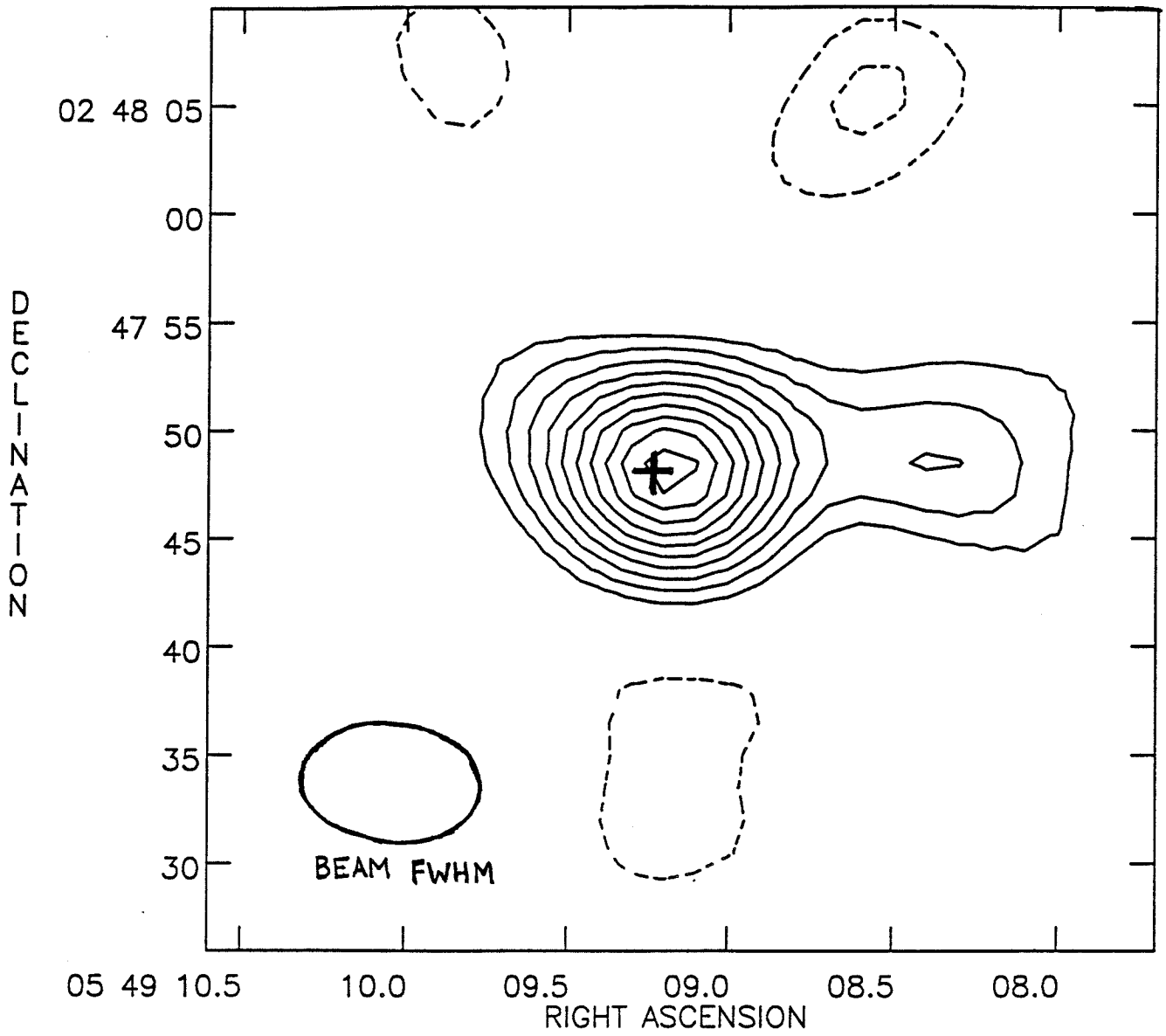

HH 111 ^{13}CO Map

Figure 6

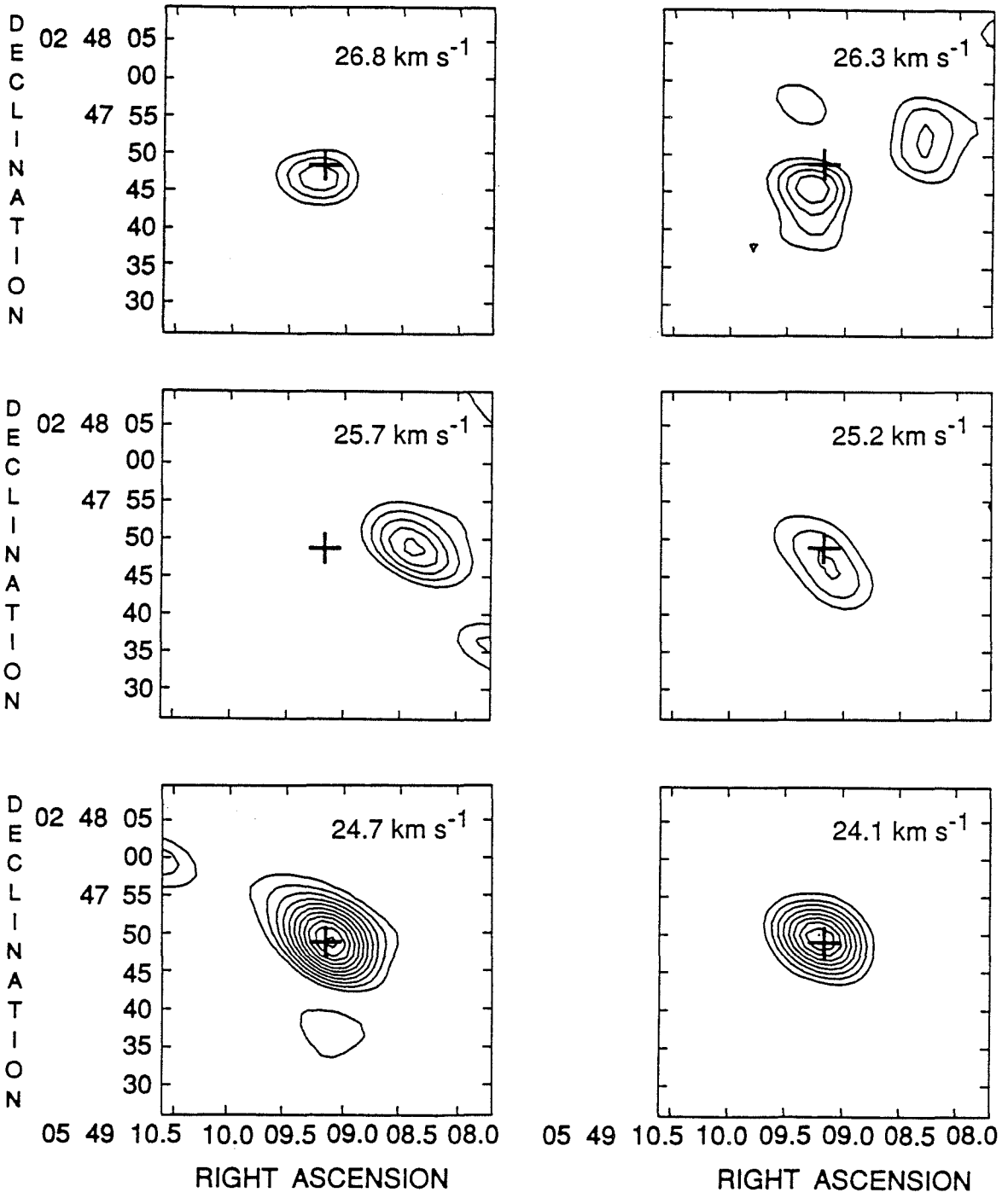

HH 111 ^{13}CO Channel Maps

Figure 7

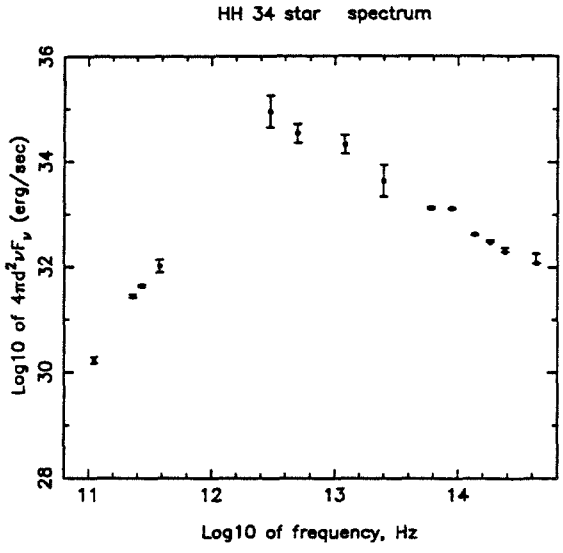
HH 34 star spectrum
Log10 of $4\pi d^2\nu F_\nu$ (erg/sec)
Log10 of frequency, Hz
28
30
32
34
36
11
12
13
14

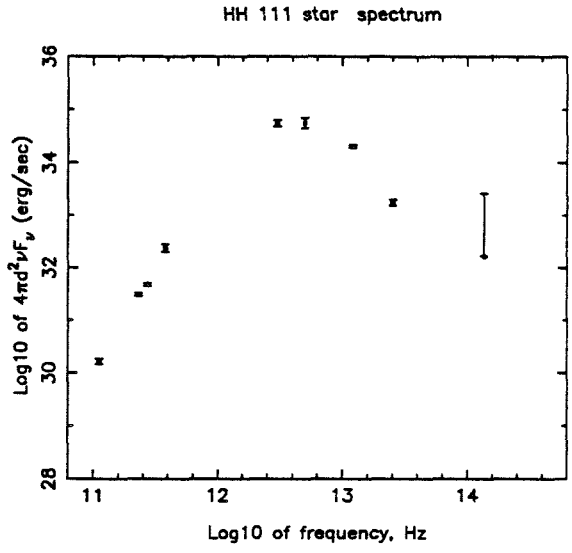
HH 111 star spectrum
Log10 of $4\pi d^2\nu F_\nu$ (erg/sec)
Log10 of frequency, Hz
28
30
32
34
36
11
12
13
14

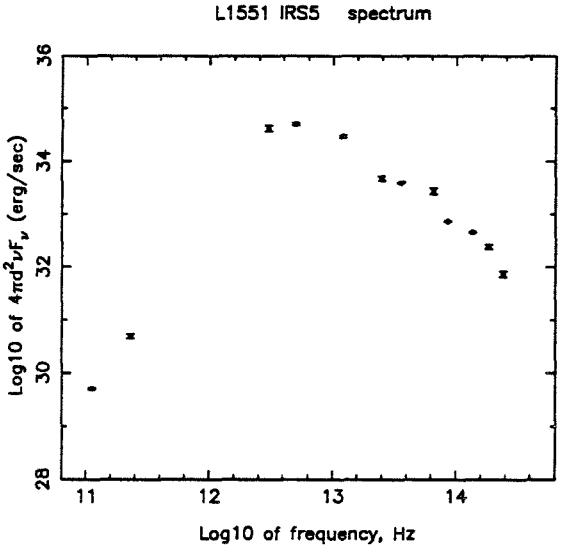
L1551 IRS5 spectrum
Log10 of $4\pi d^2\nu F_\nu$ (erg/sec)
Log10 of frequency, Hz
28
30
32
34
36
11
12
13
14

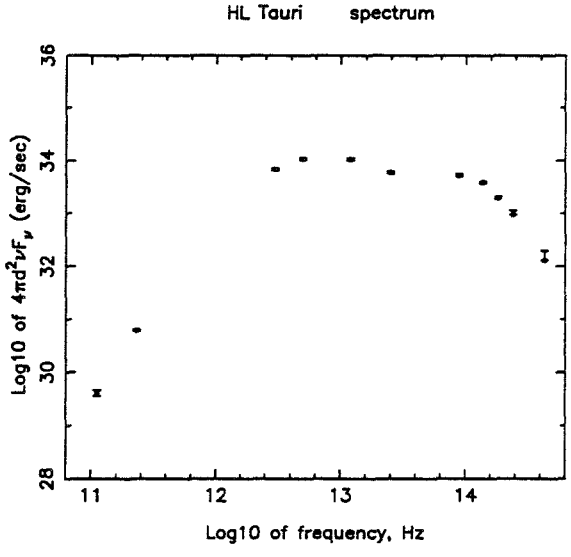
HL Tauri spectrum
Log10 of $4\pi d^2\nu F_\nu$ (erg/sec)
Log10 of frequency, Hz
28
30
32
34
36
11
12
13
14

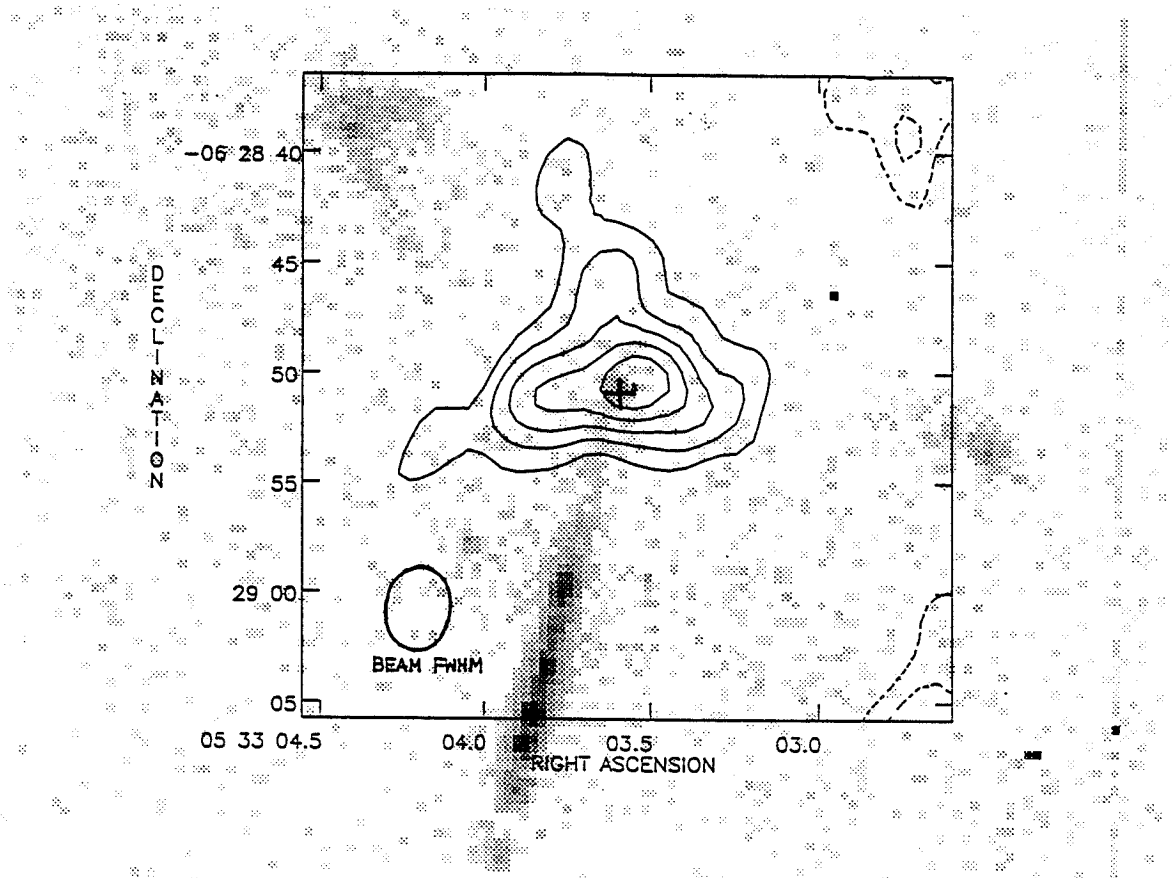

HH 34 Jet and Disk

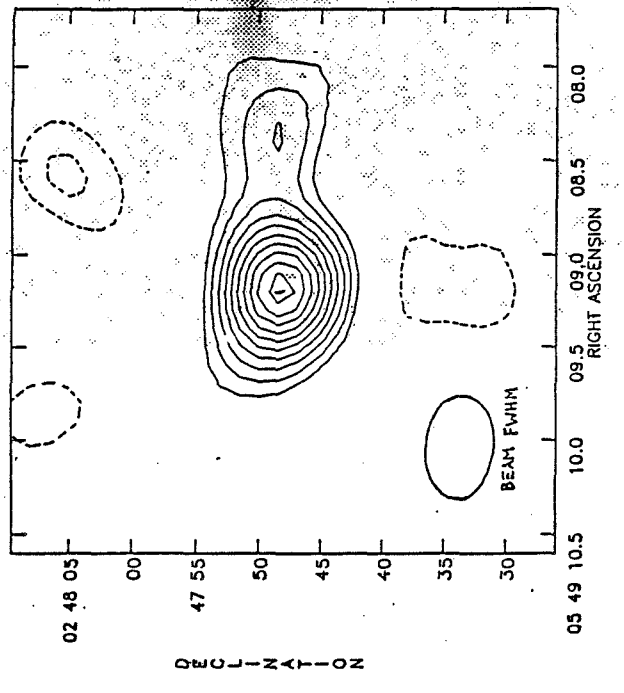

HH 111 jet + disk (?)